# Table of contents

# 1 Outline

Metabolism is the ensemble of biochemical processes allowing a cell to live and build all of its constituents, exert its functions and cooperate to determine, in multicellular organisms, the functions of tissues and organs. Different tissues are characterized by metabolic processes that can differ both qualitatively (for example the type of substrates degraded to obtain chemical energy) and quantitatively (depending on the state of activity). Thus, metabolism is modulated during development and, in adult life, as a function of the level of activity of the whole animal and of each organ. Alterations of the regulation of metabolism can lead to pathologies and a remarkable change in the metabolic asset is characteristic also of cancer cells. At the whole animal level, the measurement of metabolism is largely based on the consumption of oxygen and the production of carbon dioxide; these measurements provide a course indication on the rate of metabolism and allow correlation with physiological or pathological conditions. A more detailed measurement of metabolism, at the cellular level, would provide key insights in the processes of differentiation during embryo development, and possibly clarify the mechanisms of several pathologies. Thus, methods enabling a real time *in vivo* measurement of metabolism in the whole animal are highly desirable.

A fundamental organelle involved in the metabolic activities of the cell is the mitochondrion. Here, ATP is produced with consumption of oxygen and the involvement of coenzymes which are among the most important components contributing to a cell's autofluorescence. The signal of these molecules (NADH and FAD), as it will be shown in this thesis, represents a great tool to measure metabolism *in vivo* with cellular resolution.

Most of inhaled oxygen is used by mitochondria. Through oxidative phosphorylation, mitochondria oxidize the substrates of the Krebs cycle and produce adenosine triphosphate (ATP) which is the molecule that powers most of the cell's activities that require a source of energy. An increasing number of studies demonstrated that a wide number of human diseases are due to mitochondrial dysfunctions. Mitochondrial diseases are a large group of pathologies associated with defects in mitochondrial energy metabolism, mainly due to anomalies in the mitochondrial respiratory chain and/or in oxidative phosphorylation (OXPHOS)[1]. Oxidative phosphorylation

deficiency can cause dysfunctions in the respiratory chain, a heteromultimeric structure embedded in the inner mitochondrial membrane, or it can be associated to a single or multiple defects of the five complexes forming the respiratory chain itself [2].

During my PhD work I tested if it was possible to perform *in vivo* morpho-functional imaging of zebrafish larvae tissues and organs through nonlinear optical (NLO) microscopy that offers the advantage to obtain images from tissue and organs *in vivo* without requiring exogenous stains or tissue excision. Moreover, a goal of the thesis has been to setup methods to employ NLO microscopy for characterizing not only the morphology of a tissue but also its metabolism and functionality. NLO microscopy is a high resolution laser scanning imaging technique that allows obtaining images with a good penetration depth into tissues. Cells and extracellular matrix of biological tissues contain a variety of intrinsically fluorescent molecules (NADH, FAD, tryptophan, keratin, melanin, elastin, cholecalciferol and others). These molecules, and their interactions with the surrounding environment, can provide a tool for measuring variations of metabolism and of the cellular and extracellular environmental conditions. One of the parameters commonly utilized to study the mitochondrial health and functions is the redox ratio [1], i.e. the NADH/FAD ratio, which allows obtaining information of the cell's metabolic activity. In fact, Nicotinamide Adenine Dinucleotide (NADH) transfers electrons to the electron transport chain (ETC) while Flavin Adenine Dinucleotide (FAD) acts as an intermediary acceptor of electrons in the ETC. For this reason, it was decided to take advantage of the endogenous signal produced by these molecules to obtain information on metabolic state using nonlinear microscopy without having to add exogenous probes. The redox ratio can be obtained through the measurement of NADH fluorescence intensity, divided by the FAD fluorescence intensity. As stated above, this ratio is sensitive to changes in the cellular metabolic rate and vascular oxygen supply [1, 3]. An increase in the NADH/FAD redox ratio usually indicates increased cellular metabolic activity [4] and an increase of glycolytic state. The NADH and FAD fluorescence are reliable biomarkers reflecting the mitochondria functions. A complementary method to optically assess cellular metabolism based on NADH fluorescence relies fluorescence lifetime measurements. Combining TPEF and fluorescence-lifetime imaging microscopy (FLIM), it is possible to obtain more information about the molecular microenvironment of a fluorescent

molecule. In the case of NADH, this method provides a tool to discriminate free and protein-bound components of NADH. In fact, NADH not bound to proteins has a short lifetime (around 0.3ns), whereas when it is bound to proteins it has long lifetime (2ns – 4.5ns). Therefore, in this work I also developed methods for the *in vivo* measurement of NADH fluorescence lifetime in zebrafish larvae and compared these measurements with those bases on intensity NADH/FAD ratios for different experimental conditions.

To characterize the spectroscopic techniques developed, the zebrafish larvae were treated with compounds known for their effects on metabolism (Rotenone) and metabolic signaling pathways (DMOG). Another test of the method was performed with a transient know-down of the mitochondrial DNA Polymerase by use of morpholinos antisense oligos; in this study it has been used two kinds of morpholinos: splicing morpholinos that is zygotic-specific interfering with the maturation of a primary transcript of the mitochondrial DNA Polymerase; ATG morpholinos that not only interfering with the maturation of a primary transcript but also with mature maternal mRNAs of the mitochondrial DNA Polymerase; (thus inducing a decrease if the density of mitochondria in the developing embryo)

In the following sections, the thesis will provide:

- a discussion on mitochondrial diseases and different methods that reduce the activity of oxidative phosphorylation or activating the HIF signaling, that mimics the lack of oxygen, and the interference of MOpolG (morpholino against the transcription of mitochondrial DNA polymerase) on mitochondria replication in zebrabrafish larvae; moreover, the physical theories of nonlinear optics, in particular Two-Photon Excited Fluorescence (TPEF) and Fluorescence Lifetime Imaging Microscopy (FLIM) (chapter 1);
- a description of the housing and care of zebrafish, the procedures adopted to characterize and calibrate both experimental setups, and the methods applied for data analysis (chapter 2);
- a report on the results obtained from each study (chapter 3)
- Conclusions (chapter 4).

## 1.1 Mitochondrial Disease

Mitochondrial diseases are a large group of pathologies associated with defects in mitochondrial energy metabolism mainly due to anomalies in the mitochondrial respiratory chain and/or in oxidative phosphorylation (OXPHOS) [5]. The effects of mutations affecting the electron transport chain tend to be multisystemic, involving the visual and auditory pathways, heart, central nervous system, endocrine glands, skeletal muscle, liver, and kidneys. Since the most affected organs are the brain and skeletal muscles, pathologies are often known as mitochondrial encephalomyopathies [6]. Mitochondrial encephalomyopathies involve both mendelian and mitochondrial genetics, as the respiratory chain is under the control of two genetic systems: the nuclear genome and the mitochondrial genome. These human diseases, in fact, depend on mutations that may intervene in the nuclear and / or mitochondrial genome. It is estimated that the risk of developing mitochondrial disease is 1 out of 5,000 [7].

Numerous nuclear genes have been identified in recent years, encoding several subunits of the electron transport chain, mitochondrial proteins involved in the assembly of the peptides of each respiratory complex, and the proteins involved in the transcription and replication of mitochondrial DNA (mtDNA). Mutations in these genes cause mitochondrial diseases that follow the rules of Mendelian genetics, and which translate clinically into more or less multisystemic pathologies as described above.

The genetic classification of mitochondrial diseases distinguishes disorders due to defects in mtDNA from those due to primitive alterations of native DNA (nDNA).

MtDNA mutations are inherited according to the rules of mitochondrial genetics (maternal inheritance, mitotic segregation, heteroplasmy and threshold effect). When all copies of mtDNA in a cell are identical, they are referred to as "omoplasmia", otherwise "heteroplasmia" [8]. Heteroplasmy is a common condition in mtDNA alteration diseases. The number of mutated genomes in a certain tissue must reach a critical minimum before oxidative metabolism is sufficiently compromised to determine clinical manifestations ("threshold effect"). This threshold may vary over time and be different depending on the different tissues and is often higher in postmitothic tissues such as neurons, striated muscle, heart, endocrine glands, where there is a need for high ATP production.

The alterations in nDNA that may cause mitochondrial disease are of various kinds: structural components or ancillary proteins of the electron transport chain, intergenomic communication defects (associated with multiple deletions or single depletion of the mtDNA), membrane lipid milieu defects and mutations in the biosynthetic pathway of the Ubiquinone (also called coenzyme Q10 or CoQ10).

We can also divide mitochondrial diseases into three major nosological groups:

1) Pathologies characterized by sporadic or maternal transmission of mtDNA mutations;

2) Pathologies caused by mutations of nuclear genes linked to oxidative phosphorylation. Most of the mitochondrial diseases fall into this group.

3) Diseases due to mutations in nuclear genes used to control structural integrity and the propagation of mtDNA, resulting in a new class of pathologies due to defective nuclear-mitochondrial communication.

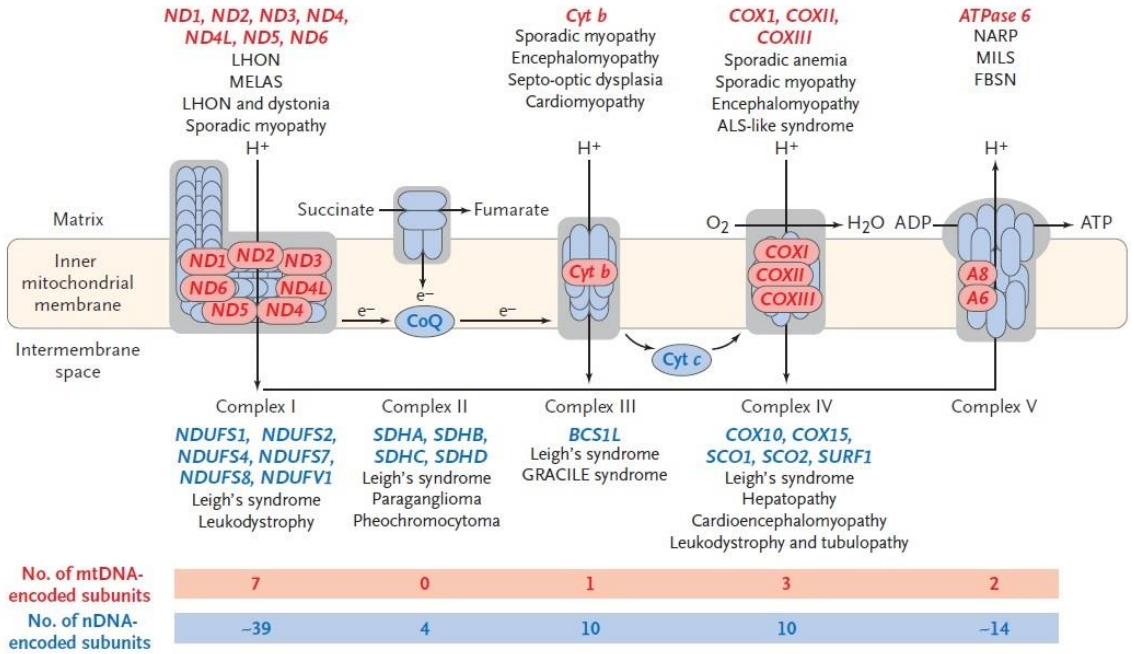


**Figure 1 shows the subunits of the respiratory chain encoded by nuclear DNA (nDNA) in blue and the subunits encoded by mtDNA in red. The figure shows also the genes responsible for the respiratory-chain disorders and the resulting diseases. ATPase 6 denotes ATP synthase 6; BCS1L cytochrome b–c complex assembly protein(complex III); NDUF NADH dehydrogenase–ubiquinone oxidoreductase; SCO synthesis of cytochrome oxidase; SDHA, SDHB, SDHC, and SDHD succinate dehydrogenase subunits; SURF1surfeit gene 1; FBSN familial bilateral striatal necrosis; LHON Leber's hereditary optic neuropathy; MELAS mitochondrial encephalomyopathy, lactic acidosis, and strokelike episodes; MILS maternally inherited Leigh's syndrome; NARP neuropathy, ataxia, and retinitis pigmentosa; GRACILE growth retardation, aminoaciduria, lactic acidosis, and early death; and ALS amyotrophic lateral sclerosis. [images taken from: Pinho, B.R., et al., How mitochondrial dysfunction affects zebrafish development and cardiovascular function: an *in vivo* model for testing mitochondria-targeted drugs. British journal of pharmacology, 2013. 169(5): p. 1072-1090. - Fink, B.D., et al., Impaired utilization of membrane potential by complex II-energized mitochondria of obese, diabetic mice assessed using ADP recycling methodology. American Journal of Physiology-Regulatory, Integrative and Comparative Physiology, 2016. 311(4): p. R756-R763.]**

The occurrence of each disease is predominantly in a certain age group, so it is common for neonatal diseases, infantile and juvenile illnesses and adult diseases.
Mitochondrial diseases may cause various interdependent processes among which low oxygen levels (hypoxia) are certainly significant. In fact the mitochondria have a central role in energy production, reactive oxygen species homeostasis, and cell death [9].

In this study we have decided to use Zebrafish as model organism because it has demonstrated to be excellent vertebrate model organism for the ease of *in vivo* manipulation and it is also advantageous for *in vivo* drug screening. Zebrafish is an ideal vertebrate model of human mitochondrial diseases because of its high conservation of physiological processes and genomic structure. The most important advantage to use Zebrafish as model organism is that its embryos are translucent and this enables the study of tissue development under a microscope.

## 1.2 Zebrafish

Zebrafish, *Danio rerio*, is a small tropical fish belonging to the Cyprinidae family, original from the Gange River, in the north-eastern region of India, Southeast Asia, e.g. Thailand, Burma, Pakistan and Bangladesh, where it lives in stagnant or flowing water like paddy fields or rivers [10]. Zebrafish is named for the five uniforms, pigmented, horizontal, blue stripes along both sides of the compressed body, which extend to the end of the caudal fin, reminding of a zebra's stripes. It is easy differentiate the sex of adults through the swollen bellies of the females in addition to their lack of yellow tint along the longitudinal stripes.

**Figure 2 Zebrafish , *Danio rerio***

This organism is extremely suitable as a model in numerous genetic and molecular biology studies of vertebrate development [11].

The small size and the food needs of this small Teleost make it is much more versatile than the mouse, allowing the retention of many individuals in confined spaces. Additionally, being an oviparous species, the ease of mating in the lab and the large amount of eggs a female can lay (about 100-200 for each reproductive event) facilitate the conduction of large-scale genetic analysis, and drug screening types of experiments requiring large statistics. In fact, the external fertilization [12] and the complete transparency of the egg [13] wrapped in the chorion allows to observe all the stages of embryonic development and to follow, through appropriate markers, the different cell destinies or to monitor the expression of specific genes at each stage. The external fertilization provides many benefits since there aren't limitations like those that it exists for in utero development. In addition, embryonic development is rapid and after 24 hours from the fertilization event, all major characteristics of the vertebrate body plane can be observed

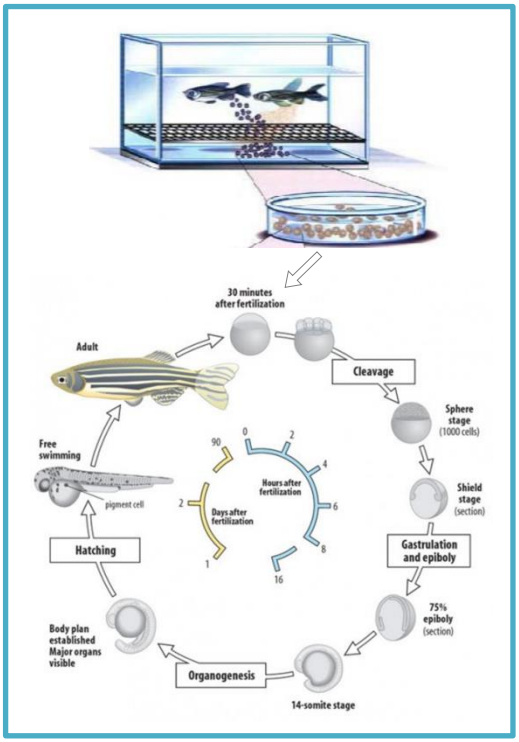


Figure 3 - Generation time of Zebrafish

On the other hand zebrafish lack specific organ structures such as the lungs, prostate, and bladder since they are characterized by structures unique to the aquatic environment.

The advantages that zebrafish offers include the ability to easily manipulate eggs and embryos [14], by allowing transplantation, cellular ablation and nucleic acid injection, by means of which, for example, gene silencing can be obtained by microinjection of antisense oligo. Zebrafish analysis and study are facilitated by the embryo's transparency, which can also be maintained artificially by the addition of phenylthiourea (PTU), melanin synthesis inhibitor, in embryo culture water. Many genes discovered in this species are evolved and conserved and homologues are present in mammals, including humans. The deep molecular similarity of the developmental mechanisms is accompanied by the fact that the comparison to the

human reference genome shows that approximately 70% of human genes have at least one obvious zebrafish orthologue [15].

## 1.3 Mitochondria

Mitochondria are the only organelles to have their own genome that is mitochondrial DNA (mtDNA), and also their own machinery for the synthesis of RNA and proteins [8]. It is believed that mitochondria were originated from a symbiotic relationship between a primitive eukaryotic cell and a eubacterium. Margulis in 1971 developped the endosymbiotic theory, that assumed that this relationship occurred after the formation of the nucleus, while in 1998 Martin e Muller suggested the hydrogen hypothesis, a different theory supposing that the mitochondrion and nucleus were formed simultaneously from a relationship between a hydrogen dependent archaebacterium and a hydrogen producing eubacterium. Both the theories presume that nucleus contains most of the genetic material inside the mitochondria [16].

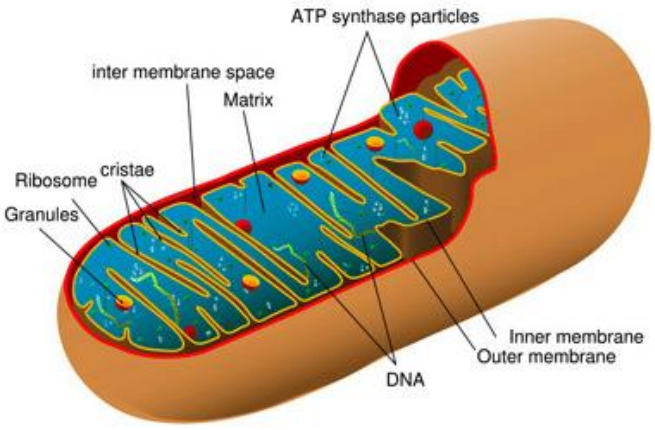


Figure 4 Diagram of a mitochondrion

Richard Altmann, in 1890, was the first to describe mitochondria calling them bioblasts. Seven years later Benda coined the term *mitochondrion*, from the Greek words meaning "thread" and "granule". In the ‘19 - '20s, Warburg discovered that in most tissue oxidative reactions take place in small parts of the cell. The mitochondria oxidize the substrates of the Krebs cycle providing the energy that the cell needs. Through β-oxidation and the Krebs cycle mitochondria transform carbohydrates, fats, and proteins into smaller molecules such as pyruvate, fatty acids, amino acids NADH (reduced nicotinamide adenine dinucleotide) and/or $FADH_2$ (reduced flavin adenine dinucleotide). These reduced equivalents are degraded and the electrons liberated by their oxidation are passed along the electron transport chain (ETC), and ultimately

transferred to molecular oxygen. The enzymatic oxidation of these chemical compounds provides the energy for the cell, providing the mechanism of conversion of oxygen and nutrients into adenosine triphosphate (ATP). ATP is the molecule that powers most of the cell's activities that require a source of energy.

The mitochondria are composed of a double (outer and inner) membrane constituted by phospholipid bilayer with embedded proteins. Here different metabolic processes take place. In the mitochondrion structure four different compartments can be identified: mitochondrial outer membrane (MOM), intermembrane space, the mitochondrial inner membrane (MIM) and matrix (the space enclosed by the inner membrane).

The inner mitochondrial membrane is extended into numerous cristae; these contain the ETC, consisting of four enzyme complexes (complexes I to IV), and two mobile electron carriers, coenzyme Q (CoQ) and cytochrome C (CytC), and the complex V (ATP synthetase). The muscle cells that have greater demand for ATP, contain more cristae than liver mitochondria.

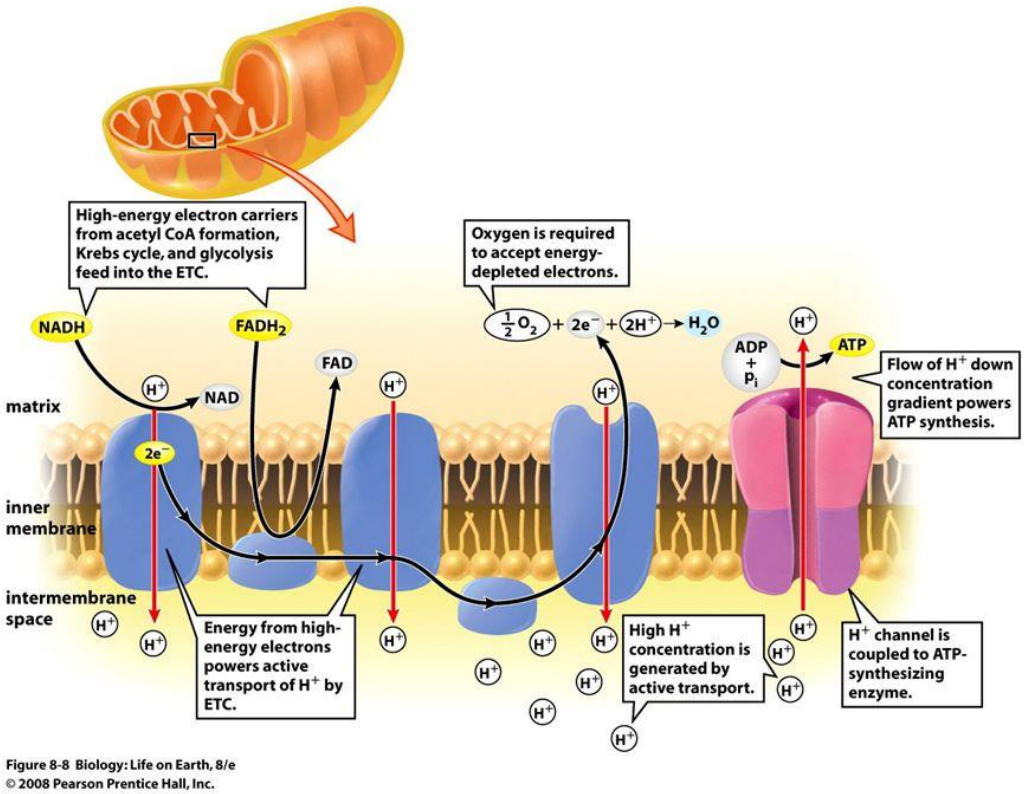


**Figure 5 Electron Transport Chain - NADH and $FADH_2$ deposit electrons into electron transport chains in the inner mitochondrial membrane; Electrons join with oxygen gas and hydrogen ions to made H2O at the end of the ETCs.**

Complex I - NADH-Coenzyme Q reductase: contains a FMN prosthetic group and seven or more iron-sulfur complexes. The FMN prosthetic group is required for activity of complex I; for this reason this complex is a flavoprotein. Through Complex I, that has iron-sulfur complexes that include both 2Fe-2S and 4Fe-4S clusters, an electron transfer occurs that carries one electron at a time from one end of the complex to the other transferring 2 electrons from NADH to coenzyme Q producing NAD+ and FMNH2 [17].

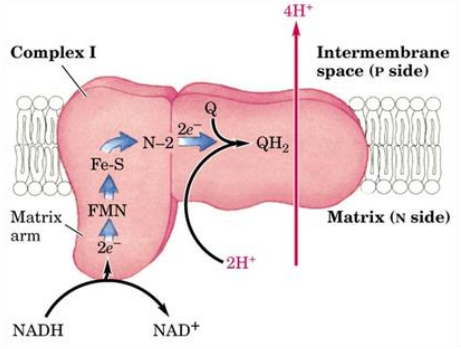


**Figure 6 Schematic picture of Complex I in the inner mitochondrial membrane.**

Complex II - Succinate-Q oxidoreductase: catalyzes an oxidation reaction that converts succinate into fumarate thorough a redox reaction involving FAD and reducing ubiquinone. Complex II is the only enzyme of the respiratory chain that does not transport protons across the membrane and does not contribute to the protonic gradient.

Complex III - ubiquinol-cytochrome c oxidoreductase is known also as CoQ-cytochrome reductase. Like complex I, complex III includes an iron-sulfur (Fe-S) protein, but it also contains two cytochromes. The electrons pass from one cytochrome to an iron-sulfur protein and then to a second cytochrome; then they are transferred to cytochrome C that is a mobile electron carrier located on the outer periphery of the membrane. In this way ubiquinol is oxidized by Complex III which reduces cytochrome c. Like complex I, complex III pumps protons from the matrix into the intermembrane space, contributing to the $H^+$ concentration gradient.

Complex IV - Cytochrome C oxidase accepts electrons one at a time from Cyt C and donates them to oxygen to form water. In the process, $2H^+$ are pumped across the membrane.

Complex V - ATP synthase converts the energy stored through a proton gradient in high-energy phosphate bonds readily available for cell demand. In fact the flow of protons (down their electrochemical gradient) across the ATP synthase drives the synthesis of ATP from ADP and inorganic phosphate (Pi).

Mitochondria are present in almost all eukaryotic cells, though some cells like red blood cells lose these organelles in their later stages of development.

As mentioned above mitochondria contains mtDNA, in zebrafish it is a circular double-stranded composed by 16596 bp, within 100 bp of the length of other teleost fishes [18]. It encodes seven subunits of Complex I - NADH dehydrogenase, one subunit of Complex III - cytochrome c reductase, three subunits of Complex IV - cytochrome c oxidase and two subunits of Complex V - ATP synthase. It also contains large (16S) and small (12S) subunits ribosomal RNA genes and 22 tRNA genes. The complex of five tRNA genes contains the origin of heavy and light strand replication noncoding control region [18]. The mtDNA transcription and replication begins from mitochondrial transcription factor A (TFAM) that wraps bends and unwinds mtDNA. TFAM determines mtDNA copy number also. Instead DNA polymerase gamma (POLγ) has key role in replication, recombination and repair of mtDNA, for this reason is essential in mtDNA. This polymerase has two subunits POLγ A and POLγ B. The POLγ A is the proofreading subunit thanks its exonuclease activity (3'→5'), while POLγ B is absolutely required for replisome function.

During the early stages of zebrafish development the mtDNA replication doesn't take place because in the process of partition of the oocyte organelles, the maternal organelles are disposed among the blastomeres, since the total content of mtDNA is constant at least 24 hour post-fertilization (hpf) [19].

## 1.4 Hypoxia

Hypoxia is a condition where the tissues are not adequately oxygenated. When the levels of oxygen are low the down regulation of metabolic demand occurs with decrease in ATP utilization and production to avoid a bioenergetics collapse. Several biological processes are regulated by the genes that are responsive of hypoxia. Among hypoxia-upregulated genes there are genes involved:

- in angiogenesis (vascular endothelial growth general introduction 13 factor - VEGF),
- in glycolysis (a glucose transporter - GLUT1)
- in regulation of cellular pH (carbonic anhydrase IX - CA IX)
- in proliferation
- in migration [20].

Hypoxia, besides, induces a decrease in the electron flux through the electron transport chain and in the electron transport this decrease limits the overproduction of Reactive Oxygen Species (ROS) during hypoxia and it slows down the rate of oxygen depletion to prevent anoxia [21].

Zebrafish adult extracts oxygen from their environment through the gills. From here the oxygen is carried by hemoglobin to tissues. Oxygen, inside the mitochondria, is used for ATP production. During the absence of oxygen, the electron transport chain does not run, and leads to a buildup of cytosolic and mitochondrial ADP, Ca2+ and NADH; thus, hypoxia leads to an increase in the [NADH] / [NAD+] ratio. To survive to low oxygen conditions, the fish keep the metabolic energy balance, and this requires a coordinated response to counterbalance the metabolic consequences of decreased ATP production in the mitochondria [22]. Depending on the time of exposure to hypoxia, the cells display changes in carbon flux into the the tricarboxylic acid (TCA) cycle:

- in acute exposure to hypoxia (from seconds to minutes), cells do not display changes
- in prolonged hypoxia (hours), there is the activation of the transcription factor hypoxia-inducible factor-1 (HIF-1), that diminishes the carbon flux into the TCA cycle, and consequently this reduces ATP production.

### 1.4.1 Hypoxia Inducible Factors - HIF

The Hypoxia Inducible Factors (HIFs) are principal transcription regulators of various hypoxia-responsive genes which help animals to survive under hypoxia.

Sundry studies displayed that there is a relationship between mitochondrial alterations and hypoxia signaling pathway [23-25].

Oxygen is essential for aerobic respiration. Zebrafish, being an aquatic organism, uses the oxygen dissolved in water. When the dissolved oxygen (DO) concentration falls below 2.8 mg /L there is hypoxia [21, 26]. To survive in hypoxic environments, fishes have evolved a diversity of mechanisms to obtain more oxygen from their low DO surroundings. During hypoxia the metabolism of fish undergoes a physiological adaptation altering the pathways of metabolic energy production, and increases tolerance to ionic and pH disturbances [27]. Under hypoxia the metabolism of fish shifts from aerobic to anaerobic pathways.

The hypoxia leads a cellular response characterized by coordinated regulation of the expression of a large number of genes that have several roles like hypoxia-inducible factor (HIF), which exists as a heterodimer of an alpha and a beta subunit [28].

While HIF-1 β is readily found in cells under all oxygen conditions, HIF-1α is virtually undetectable in normal oxygen conditions [29].

In normoxic conditions alpha subunits of HIF are hydroxylated by HIF prolyl-hydroxylases at conserved proline residues located within the oxygen-dependent degradation domain ODDD, these modifications allow the binding of the E3 ubiquitin ligase to von Hippel Lindau protein (pVHL) and subsequently rapid degradation by the proteasome. The VHL protein binds HIF-1α and HIF-2α recognizing two specific hydroxyproline residues [30-32].

Three homologous 2-oxoglutarate-dependent dioxygenases PHD1, PHD2, and PHD3 catalyze this prolyl hydroxylation [33, 34]

The 2-oxoglutarate-dependent dioxygenase (FIH-1) yields the formation of a specific hydroxyasparagine in the C terminus of HIF-α providing another oxygen-dependent modification of HIF-α.

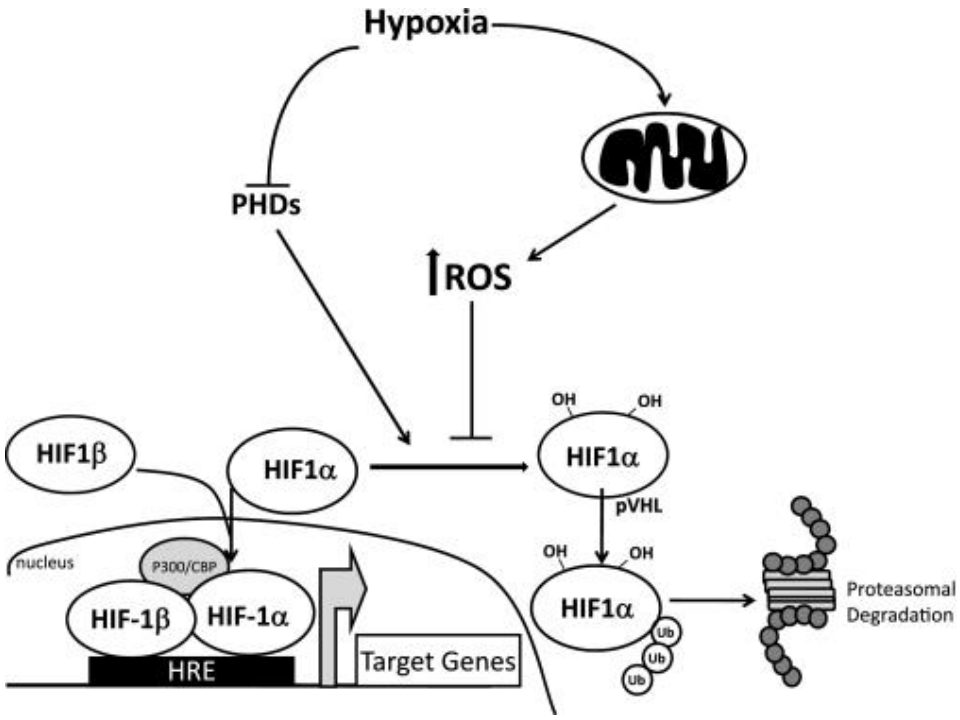


**Figura 7 Hypoxia inducible factor-1 (HIF-1) is activated by hypoxia: pyruvate dehydrogenase 2 (PHD2) labels the HIF1α subunit hydroxylating it at distinct proline residues, in this way HIF1α is recognized by the protein for von Hippel-Lindau protein (pVHL) mediating the proteasomal degradation. Concomitantly hypoxia induces the production of mitochondrial reactive oxygen species (ROS) at complex III, and decreases PHD2 activity, so there is an inhibition of hydroxylation of HIF1α subunit. In the promoters and enhancers of target genes that modulate metabolism, HIF1α subunit is stabilized and it can bind HIF-β and p300 coactivators to hypoxic response elements (HREs). [Wheaton, W.W. and N.S. Chandel; *Hypoxia regulates cellular metabolism.* American Journal of Physiology-Cell Physiology, 2011. 300(3): p. C385-C393]**

.

In hypoxic conditions, PHDs and FIH-1 enzymes are inhibited owing to the absence of oxygen that PHDs utilize as a co-substrate. The HIF-α protein is therefore not targeted for proteasomal degradation and it is translocated to the nucleus where the dimerization between HIF-α and HIF-β (to form the active complex HIF-1) occurs. HIF-1 interacts with the transcriptional coactivators p300/CBP [29, 35]. In the nucleus, the complex HIF-1 upregulates several genes to promote survival in low-oxygen conditions, binding to the hypoxic response elements (HREs) in the regulatory regions of target genes, that include glycolysis enzymes and vascular endothelial growth factors (VEGF). When HIF-1 is activated, there is an increase of concentration of glucose and then an acceleration of glycolysis processes. In 1992, at first, it was discovered that the HIF-1 was responsible, in hypoxic conditions, for the expression of erythropoietin. Since this discovery, more than 60 genes have been found to be induced by HIF-1; the products

of these genes are implicated in many different cellular functions such as cell survival, cell proliferation, apoptosis, glucose metabolism and angiogenesis [36].
To simulate HIF in Zebrafish it was used Dimethyloxalylglycine (DMOG).

### 1.4.2 The role of hypoxia in stem cell niche in physiological and pathological condition

From literature it is known that the hypoxic microenvironment preserves the niche cell pool and its function in the Bone Marrow (BM); in fact the key cell types, involved in regulating hematopoietic stem cell (HSC) maintenance, are affected by hypoxia. Multiple niche factors are secreting from various niche cells to induce quiescence or activation operating on gene expression of HSCs. The Wnt pathway is inhibited by HIF-1α to activate EPO production in osteoblasts. While in mesenchymal stem/progenitor cells (MSCs), HIF-1α represses transcription of a key regulator of osteogenesis (RUNX2) that inhibits MSC differentiation and also it suppresses the STAT1/IFN signaling; moreover hypoxia regulates negatively the maturation of megakaryocytes [37].

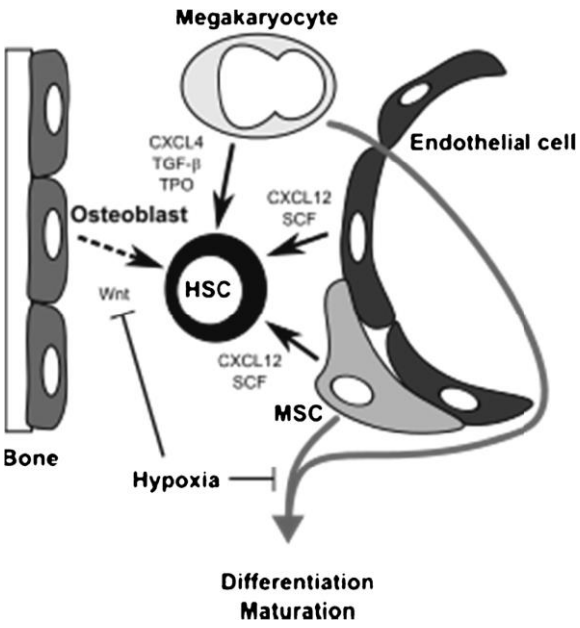


**Figure 8 Niche signals in hypoxic BM.** ***[Hypoxia regulates the hematopoietic stem cell niche - Takayuki Morikawa]***

It is also known in the literature [37-39] that the hypoxia signaling is activated and it is functioning in hematological malignancy. To survive, leukemic cells acquire the ability to activate HIF signaling even under normoxia and they deviate hypoxia-regulated mechanisms for stem cell-specific events such as self-renewal and drug resistance. The molecular mechanisms through which leukemias activate HIFs are still elusive, and a possibility may be that HIF signaling is already activated in HSCs in normoxia, and this property is transformed to leukemic cells and this could be the case in CML, an HSC-

level disorder. However, the origins of other types of leukemia that derive from non-HSCs have not been fully investigated.

### 1.4.3 Dimethyloxalylglycine - DMOG

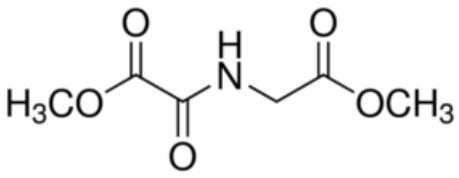


**Figura 9 DMOG is a cell permeable prolyl-4-hydroxylase inhibitor which upregulates HIF activity. HIF activation stimulates angiogenesis in several different models (1nM). DMOG also inhibits FIH (factor inhibiting HIF), an asparaginyl hydroxylase, which enhances the HIF response. [40]**

Dimethyloxalylglycine is a synthetic analogue of α-ketoglutarate; it is a competitive inhibitor of the PHDs [34] and it is commonly used to induce HIF signaling. DMOG was used to activate HIF signaling in zebrafish. DMOG stabilizes and activates HIF-1α by inhibiting hydroxylases via two mechanisms:

- acting as competitive antagonism of α-ketoglutarate
- acting as iron chelators

these mechanisms produce the activation of the HIF system with enhanced transcription of target genes.

DMOG inhibits the HIF prolyl and asparaginyl hydroxylases.

Through DMOG, like in hypoxic conditions, PH prolyl-hydroxylase is inhibited, because it utilizes oxygen as a

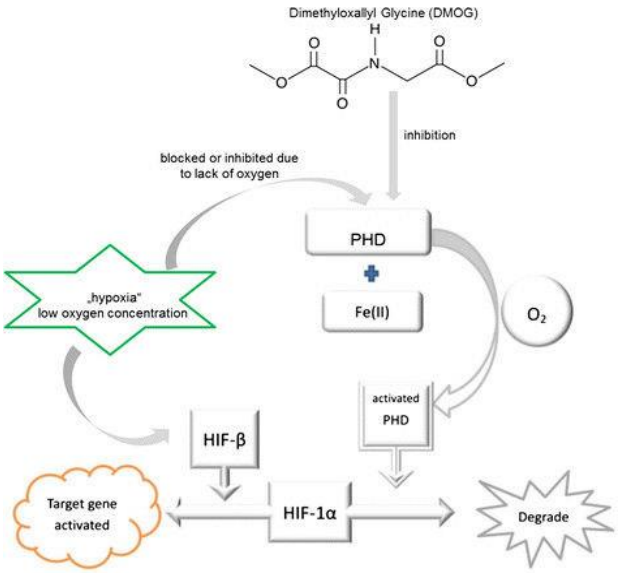


**Figure 10 DMOG inhibits the Prolyl hydroxylase (PHD) that is catalyzed with the presence of oxygen and Fe (II), and then subsequently involved in the HIF protein degradation. Otherwise, HIF-1α is stabilized and dimerized with the HIF-β, and activates the target genes. *[Yuan, Q., et al., PHDs inhibitor DMOG promotes the vascularization process in the AV loop by HIF-1α up-regulation and the preliminary discussion on its kinetics in rat. BMC biotechnology, 2014. 14(1): p. 112.]***

co-substrate. This inhibition induces the dimerization between HIF-1 α and HIF-1β that is phosphorylated and translocated to the nucleus. Here HIF-1 upregulates several genes to promote survival in low-oxygen conditions. These include glycolysis enzymes and vascular endothelial growth factor (VEGF). Then, when HIF-1 is activated, we have an increase of concentration of glucose and then an acceleration of glycolysis processes. Through DMOG we induce HIF signaling then an increase of glycolysis. Therefore the use of DMOG causes a shift to glycolytic metabolism and then an increase in NADH and a decrease in FAD. To study whether it is possible to observe the metabolic changes through TPEF microscopy and FLIM microscopy it has been used also Rotenone.

### 1.4.4 Rotenone

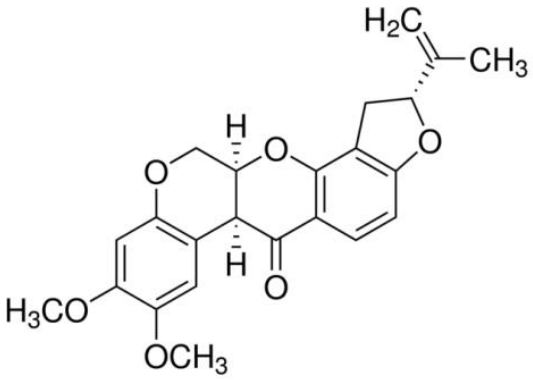


**Figure 11 Rotenone is a broad spectrum insecticide that occurs naturally in seeds and stems of several plants. Biological Activity: Mitochondrial electron transport chain inhibitor. Commonly used pesticide and induces Parkinsonism in animal models [41]**

Rotenone is a natural compound that can be extracted from the roots of Derris sp. Rotenone is utilized as an insecticide owing to its ability to inhibit the mitochondrial respiratory chain, specifically in complex I. The inhibition of mitochondrial electron transport induces cell death in a variety of cells, enhancing the amount of mitochondrial reactive oxygen species production (ROS) [42].

Complex I inhibition with Rotenone induces a strong increase in ROS generation [43]. ROS play an important role in apoptosis as they can influence mitochondrial function without having the longtime of diffusion from the cytosol [44].

Rotenone blocks electron transfer from iron–sulphur clusters to the ubiquinone pool.

Fumarate generated from oxidation of succinate, in complex II, is converted in malate. Malate is, in turn, converted to oxaloacetate (OAA) or it leaves mitochondria through the dicarboxylate carrier. The conversion to OAA requires $NAD^+$/NADH cycling at complex I. When Rotenone is present, the formation of OAA is inhibited like the formation of succinate dehydrogenase (SDH). This involves the increased respiration and also increased exit of malate from the mitochondria [45].

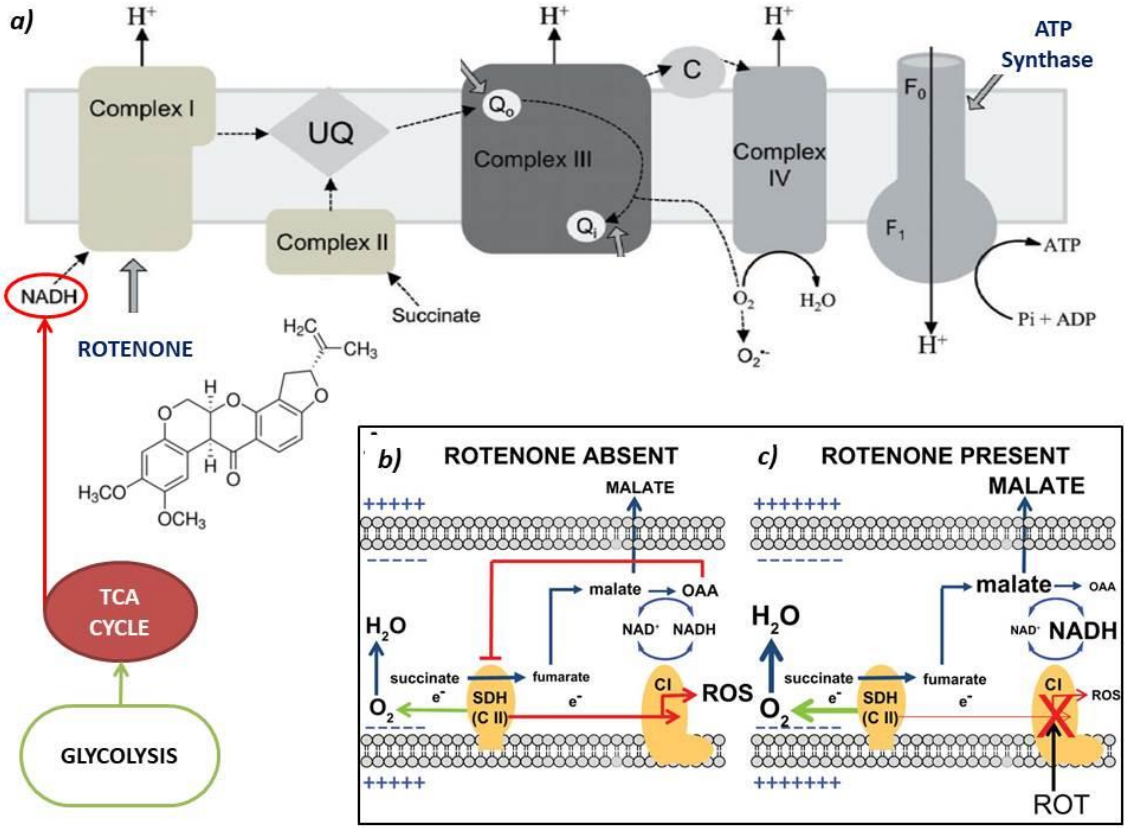


**Figure 12 Show the molecule of Rotenone that acts on complex I of the mitochondrial respiratory chain. A) It is possible to observe the electron flow (dashed-line arrows) from substrates to oxygen, and the protons (H +) pumping across the inner mitochondrial membrane (IMM); b) & c) Rotenone inhibits complex I, preventing the NADH oxidation and the OAA formation. Green arrows depict forward electron transport (proportional to O2 flux), the red arrows show reverse electron transport. The membrane charge differential (blue +) is utilized for ATP production. The metabolite flow depicted above assumes the availability of moderate amounts of ADP. *[images taken from: Pinho, B.R., et al., How mitochondrial dysfunction affects zebrafish development and cardiovascular function: an in vivo model for testing mitochondria-targeted drugs. British journal of pharmacology, 2013. 169(5): p. 1072-1090. - Fink, B.D., et al., Impaired utilization of membrane potential by complex II-energized mitochondria of obese, diabetic mice assessed using ADP recycling methodology. American Journal of Physiology-Regulatory, Integrative and Comparative Physiology, 2016. 311(4): p. R756-R763.]***

The complex I inhibitors can be distinguished in two classes depending on their effect on ROS production [46]:

1) Class A inhibitors: inducing strong increase in ROS production - include Rotenone;

2) Class B inhibitors: preventing ROS production.

Rotenone inhibiting ETC at complex I causes the increment of glycolytic metabolism. The shift to glycolytic metabolism is followed by an increment of NADH/FAD ratio because NADH is not oxidized to $NAD^+$.

After acting on mitochondrial metabolism using DMOG that activates the HIF signaling, and Rotenone that inhibits the ECT irreversibly, it was used a transient knock-down of DNA polymerase Gamma (Morpholino polG) that is essential for replication of mitochondrial DNA.

### 1.4.5 Morpholino

Morpholino is a synthetic molecule that is the product of a natural nucleic acid structure and it is used in molecular biology to modify gene expression. The name Morpholino comes from a six-membered morpholine ring in the backbone where the DNA bases are attached due to the phosphorodiamidate groups.

Morpholinos usually are used for knocking down gene function owing to their capability to block access of other molecules to small specific sequences (~25 base) of the base-pairing surfaces of ribonucleic acid (RNA). Morpholino inhibits the interaction between the target sequence of RNA and the molecules that may interact with this, acting by "steric blocking".

Premature stops and nonsense-mediated decay of the transcript can occur when there is the inclusion of the intron. The scanning of the 40S ribosome is interfered by translational blocking MOs bind the AUG or 5’ UTR, and also occurs the translational inhibition and elongation by the full ribosomal complex.In this study the morpholino oligos were injected into embryos of zebrafish.

#### 1.4.5.1 DNA polymerase gamma (POLG)

DNA polymerase gamma (POLG) is essential for replication and repair of mitochondrial DNA (mtDNA). Mutations in POLG cause mtDNA instability and a diverse range of poorly understood human diseases. The pathogenic POLG mutations are associated to

various types of disorder that are different from each other in severity, affected tissues and age of onset. Most of them occur through POLG-mediated mtDNA replication errors, like Childhood myocerebrohepatopathy spectrum (MCHS), Alpers' syndrome, Autosomal recessive progressive external ophthalmoplegia (arPEO).

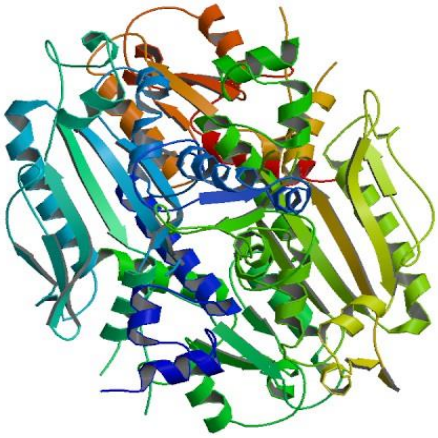

Figure 13 Crystal Structure of DNA polymerase gamma accessory subunit

MCHS causes developmental delay or dementia, lactic acidosis, and a myopathy. This disease appears between the first few months of life up to about age three years. MCHS can include also liver failure, renal tubular acidosis, pancreatitis, cyclic vomiting, and hearing loss [47].

Alpers' syndrome is an autosomal recessive and developmental mitochondrial DNA depletion disorder of fatal neurogenetic type. It is Characterized to deficiency in mitochondrial DNA polymerase γ (POLG) catalytic activity [48].

Autosomal recessive progressive external ophthalmoplegia (arPEO) caused by the ptosis and ophthalmoparesis (or paresis of the extraocular muscles) without associated systemic involvement [47].

Unfortunately, to date, effective treatments for patients suffering from these diseases are not yet available[49].

### 1.4.5.2 Morpholino polymerase Gamma - MOpolG

For this analysis we used a morpholino-based transient knock-down. As already explained, Zebrafish is an excellent model organism for this kind of analysis, for its ease *in vivo* manipulation and in coupling. We used 2 kinds of morpholino:

- Morpholino against a splicing site of PolG;
- Morpholino against ATG PolG;

Both morpholino were provided from Genetools and kindly furnished by Zebrafish Group of University of Padova.

Morpholino splicing inhibits the splicing of the primary transcript to the mature mRNA, while Morpholino ATG blocks protein translation of the mRNA at the translation start site, and they will also knock down maternally loaded mRNAs; on the contrary the splice-blocking MOs are ineffective on already mature transcripts. In detail, the ATG morpholino functions by binding to a sequence on or close to the ATG start site of the mRNA transcript, sterically blocking the translation machinery and thus preventing protein synthesis, while morpholinos splicing act upon pre-mRNA by binding to intron/exon junctions and preventing proper splicing. Depending on the sequence, this can result in either retention of an intron as illustrated in pathway B in figure 13a, loss of an exon, or the use of a cryptic splice site causing either truncation of an exon or retention of a partial intron. Upon export to the cytoplasm, these altered transcripts would either be degraded by nonsense-mediated decay, or in some cases could result in synthesis of a truncated protein. Both types of MOs will inhibit protein synthesis from zygotic transcripts. These MOpolG shows the phenotype that is characterized by homogeneous developmental delay without obvious malformations, except for the

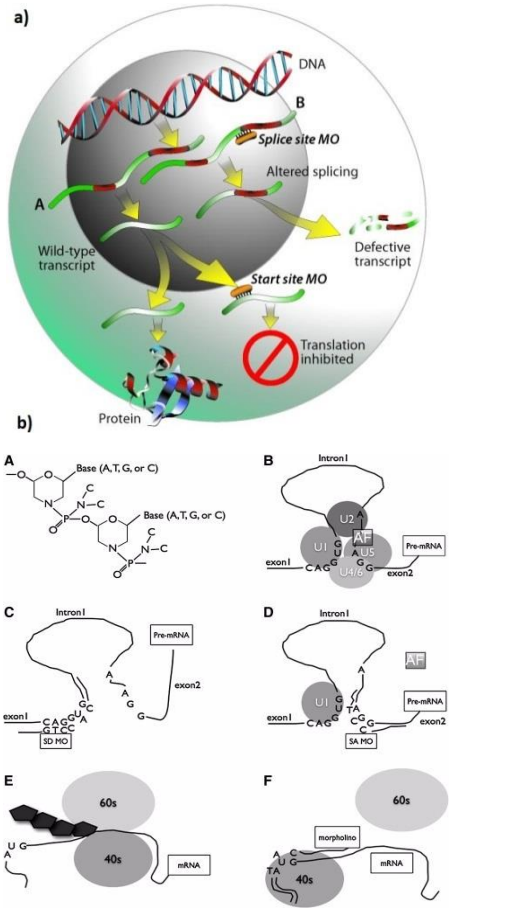


**Figure 14 a) Illustration of how start site (A) and splice site (B) morpholinos work; b) Mechanism of action of Morpholino splicing**

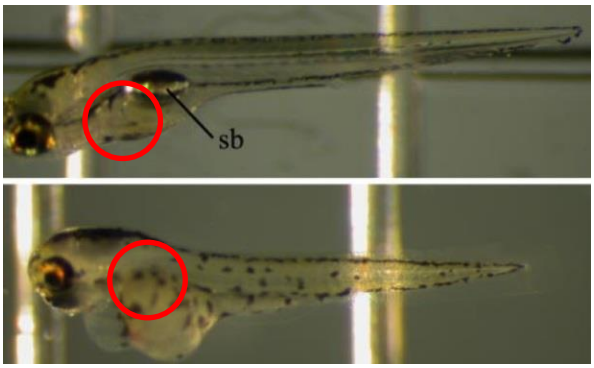


**Figure 15 a) Control zebrafish that has not been microinjected; b) Zebrafish microinjected shows enlargedcardiac chambers and developmental delay**

observation of enlarged cardiac chambers, associated with increased heart rate (shows in figure 14) **[50]**.

## 1.5 NADH and FAD

TCA cycle provides the reduced form of nicotinamide adenine dinucleotide (NADH) and the flavin adenine dinucleotide (FAD) that are two important coenzymes presents in the electron transport chain ETC, that is, as mentioned in paragraph 1.3, the primary means of energy production in the cell [1]. The role of NADH is to yield electrons to molecular oxygen, while the role of FAD is to accept electrons. These coenzymes are also two endogenous autofluorescent molecules, and they allow obtaining noninvasive imaging without staining, processing or tissue excision. The fluorescence of NADH is due to its nicotinamide ring; in fact the form $NAD^+$ is not fluorescent as it lacks of this ring. The fluorescence intensity of NADH can be observed at 350 nm excitation and the emission at 460 nm[3]; on the contrary the oxidized state of FAD ($FAD^+$) is fluorescent, and the reduced state (FADH2) is non-fluorescent [51]. The levels of reduced NADH and FAD are very important to study the cellular metabolism, because they have an important role in a wide range of cellular oxidation–reduction reactions. To investigate simultaneously the fluorophores NADH and FAD, we chose to use the excitation wavelength at 740 nm for TPEF and FLIM microscopy, because through this excitation wavelength it is possible to excite both the fluorescent molecules how we can see from the graph a in Figure 18.

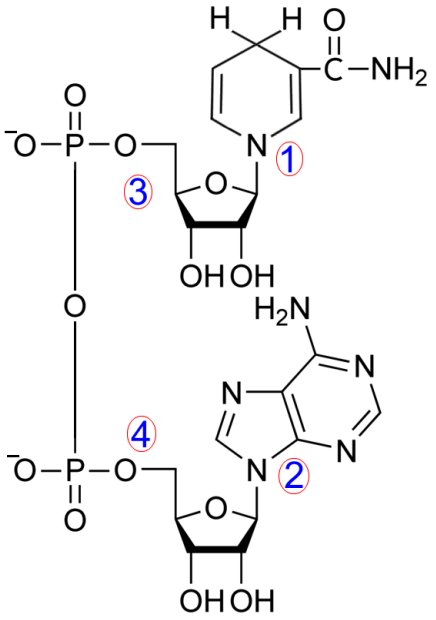


**Figure 16 Molecule of NADH ①Niacin, also known as nicotinic acid; ② Adenine is a nucleobase (purine derivate); ③and④ Dinucleotide: phosphate group and pentose sugar (ribose)**

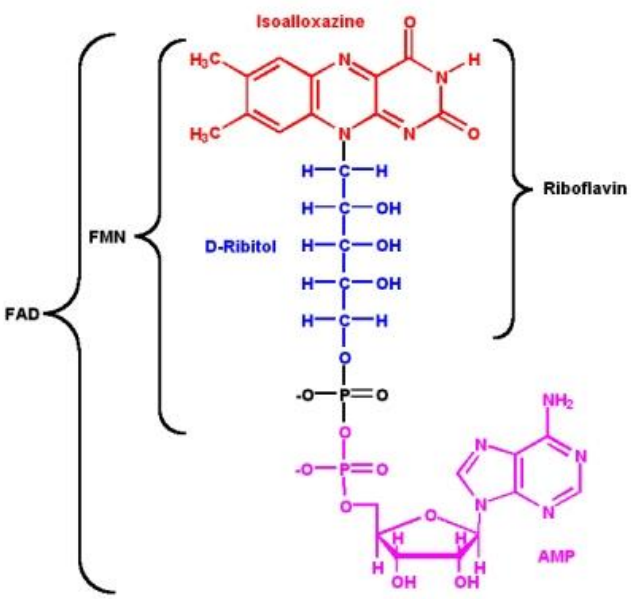


**Figure 17 Molecule of FAD**
**①Isoalloxazine ring**
**②Riboflavin 5' phosphate**
**③Adenine is a nucleobase (a purine derivative)**

Various bioenergetics parameters are used to study the mitochondrial health status and functions; these parameters give information about mitochondrial functionality or individual mitochondrial complexes.

The redox ratio is the most conventional method, which allows obtaining metabolic information from Nicotinamide Adenine Dinucleotide (NADH) and the Oxidized Flavin Adenine Dinucleotide (FAD). This method allows evaluating *in vivo* the metabolic state of cells through a non-invasive and fast analysis.

The redox ratio is also sensitive to vascular oxygen supply [3, 52-55]. Hypoxia (as described in paragraph 1.4) causes an increase of NADH concentration and a decrease of FAD concentration, hence a change in their concentration ratio (NADH/FAD). An increase in the redox ratio usually indicates an increased cellular metabolic activity [56]. These coenzymes are then utilized to study the metabolic state of mitochondria, permitting to evaluate if the mitochondrial functions are compromised, due to the fluorescence of NADH and FAD that are two reliable.

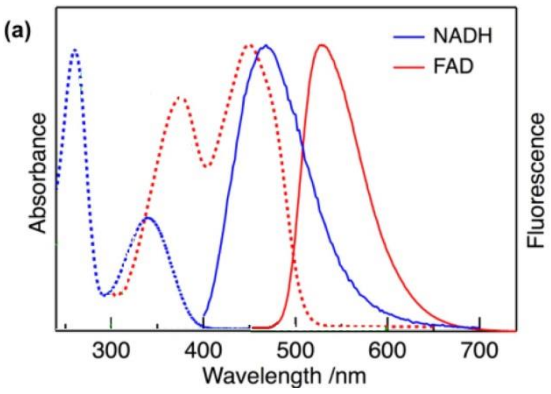


**Figure 18 a) spectral absorptions and emissions of NADH and FAD**

Mitochondria are essential for energy metabolism, oxidative stress, and for programmed cell death. The mitochondrial function can be compromised by mutated mtDNA when its enzymes complex structures are modified, because this leads to a huge number of severe diseases, like neurodegenerative diseases, cancer and diabetes, that are very important to be detected [57].

## 1.6 Nonlinear microscopy

Nonlinear optical microscopy (NLO) techniques are utilized to study autofluorescence signals in living tissues, structural protein arrays, and they are successfully employed in several other biomedical research fields.

NLO is based on nonlinear optic effects related to the non-linear interaction between light and media, in which the induced electric polarization is a non-linear function of the incident electric field [58]. The nature of non-linear optics effects could be coherent or incoherent. Two-photon excited fluorescence (TPEF) microscopy is the most widely known versions of non-linear microscopies. It is based on the possibility to excite an electronic transition through simultaneous absorption of two photons, each of them having an energy equal to half the transition energy, as theorized in 1931 by Maria Goeppert-Mayer [59].

Only 30 years later, it was possible to observe this phenomenon: Kaiser and Garrett measured a two-photon transition in a CaF2: Eu2 + crystal. Since two-photon absorption requires high spatial and temporal density of photons, old light sources were unable to obtain such density without damaging biological samples. Therefore, it was necessary to wait the development of femtosecond pulsed lasers for having the realization of the first two-photon laser scanning microscope in 1990 [60].

## 1.7 TPEF – Two-Photon Excited Fluorescence

Two-photon excitation process involves the transition of molecules from the ground state to the excited state through an intermediate virtual state owing to the simultaneous absorption of two photons in a single quantum event. Each photon has half of the transition energy. For having a reasonable probability of exciting such a process, it is necessary to irradiate the sample with a high density of photons (0.1 - 10MW / $cm^2$) from a laser source that produces pulses of duration in the ps/fs range. This condition arises from the fact that a virtual state has a very short lifetime ($10^{-16}$s). It is only within this temporal window that a second photon can be absorbed to allow the irradiated electron reaching the excited state. Since TPEF depends on the simultaneous absorption of two photons, the transition probability, and hence the

resulting fluorescence emission intensity, depend on the square of the excitation intensity. TPEF is very useful for imaging living cells, providing a mean for optically monitoring physiologic and biochemical events within the cells or other biological tissues [61], including intact tissues such as embryos and whole organs. Furthermore, TPEF provides images with good signal/noise ratio of molecular autofluorescence signals, demonstrating the capability of this technique to provide label-free morphological imaging of biological samples. The use of endogenous molecules for creating naturally present in cells and tissues there is no need to use dye and this reduces the risk of introducing artifacts associated with the preparation of the sample [62].

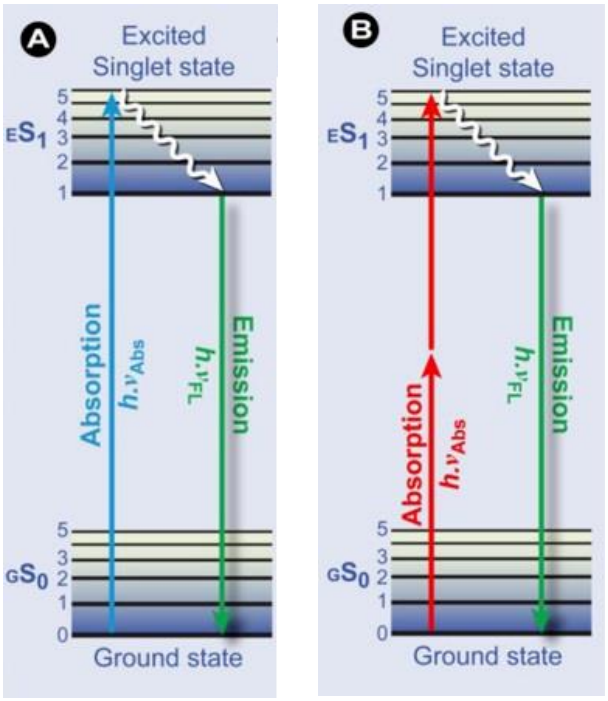


**Figure 19 - Jablonski diagram - A) One-photon excitation scheme, occurring through the absorption of a single resonant photon. B) TPE excitation scheme, occurring through the absorption of two lower-energy photons via a short-lived intermediate state. In both cases, the absorption of photons produces an excited state from which the molecule can relax by emitting a fluorescent photon. [*Ishikawa-Ankerhold, H.C., R. Ankerhold, and G.P. Drummen, Advanced fluorescence microscopy techniques—Frap, Flip, Flap, Fret and flim. Molecules, 2012. 17(4): p. 4047-4132.*]**

Biological tissues contain many endogenous fluorescent molecules that the researchers use to obtain information about cellular activity. Among the endogenous fluorescent molecules there are the mitochondrial matrix proteins NADH, FAD, lipoamide dehydrogenase, also the structural proteins elastin, keratin, and collagen, and the pigments lipofuscin, melanin, and porphyrins. The intracellular fluorescence occurs above all from NADH, flavins, retinol, tryptophan, and indoleamine derivatives of tryptophan; while a majority of extracellular fluorescence comes from the structural proteins elastin and collagen [61]. These molecules have absorption spectra located in the UV-VIS range of the spectrum and are immersed in a highly scattering medium. On the other hand, biological tissues have particularly low absorption in the region from

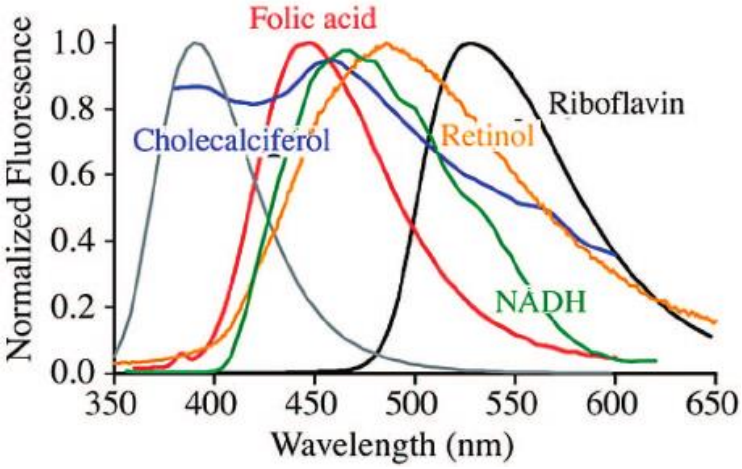


Figure 20 - Emission spectra of some biological components

700 to 1000 nm. This range in the near infrared (NIR) window is included within the optical therapeutic window for tissues (600 – 1600 nm), where both scattering and absorption are reduced with respect to shorter wavelengths, allowing a deeper penetration of light within a highly scattering medium. Non-linear interaction allows exciting a transition located in the UV-VIS range, targeting endogenous fluorophores by means of NIR photons that ensure deeper imaging capability

### 1.7.1 Spatial resolution and localization of excitation

The minimum distance $\Delta$ at which two points can be distinguished depends on the on the width of the point-spread function (PSF), which is the optical response of the system to a point source. In optical microscopy, the expressions of Abbe for lateral and axial resolution are:

$$\Delta_{x,y} = \lambda / 2[n \bullet \sin(\alpha)]$$

$$\Delta_z = 2\lambda / [n \bullet \sin(\alpha)]^2$$

where λ is the wavelength of light, n represents the refractive index of the imaging medium, and the combined term n • sin(α) is known as numerical aperture (NA). In laser scanning fluorescence microscopy, the spatial resolution is determined by the size of the excitation volume. The fluorescence emitted from a molecule has an intensity that is proportional to the transition probability.


**Figure 21 Comparison of excitation volumes. a) One photon excitation of a fluorescein sample, using 488 nm with NA = 0.16. b) Excitation by two-photon of the same sample, using light at 960 nm with NA = 0.16.**

The transition probability of one-photon transition is proportional to the intensity of light; this means that the excitation volume is determined by the distribution of light intensity within the sample. In confocal microscopy, the excitation volume is a large cone Figure 22 and a confocal pinhole is used to exclude out-of-focus background. The transition probability is proportional to the number of the photons involved in the excitation process, hence to $I^2$ for TPEF [63]. This feature, due to a non-linear optical interaction, allows confining the excitation to a smaller volume with respect to an equivalent single-photon interaction, eliminating out-of-focus background. Smaller excitation volume provides better spatial resolution and reduces phototoxicity as potential photodamage is confined to the focal volume [64].

The confocal microscope yields three-dimensional sectioning capability, but it produces photobleaching and phototoxicity throughout the specimen, because of out-of-focus excitation. In TPEF, the excitation is inherently confined to a small volume in the focal volume because the non-linearity of the interaction prevents the unwanted out-of-focus background. Hence, a resolution comparable to that of confocal microscopy can be obtained without a confocal spatial filter [65]. TPE allows three-dimensional optical sectioning without out-of-focus absorption and then can be less phototoxic. TPEF offers increased penetration depth within tissues when compared to confocal microscopy. In fact, it uses NIR light that is less absorbed and scattered by biological tissues than visible light. In addition, the scattering of excitation light when imaging deep into a biological tissue have a minimal impact on spatial resolution in TPEF, since diffused photons are not able to excite molecules out of the focal volume. The amount of diffused photons increase with the imaging depth but it does not reduce spatial resolution, since scattered photons do not contribute to the excitation process.

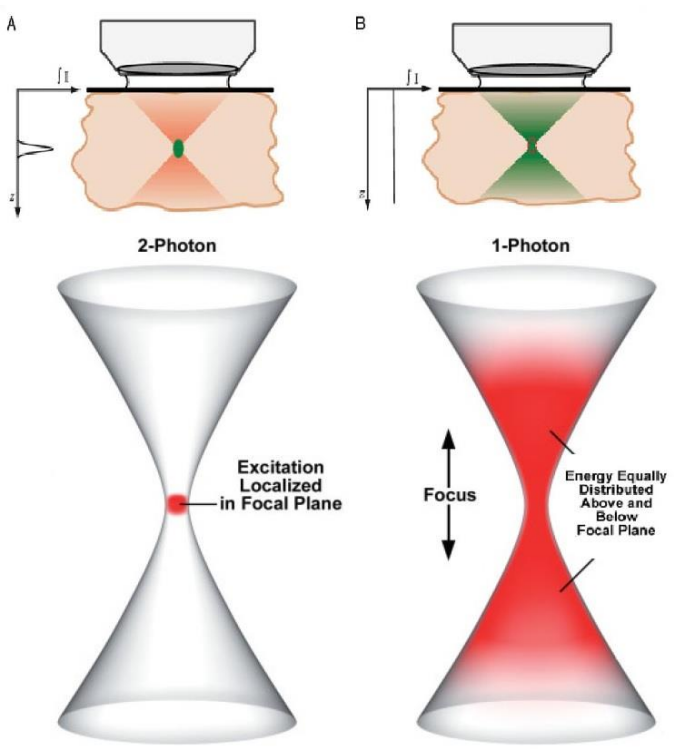


**Figure 22 Localization of excitation - a) In two-photon microscopy the fluorescence excitation is localized in the focal point; b) In single-photon microscopy, fluorescence is excited also in the planes above and below the focal plane. [*Benninger, R.K. and D.W. Piston, Two-photon excitation microscopy for the study of living cells and tissues. Current protocols in cell biology, 2013: p. 4.11. 1-4.11. 24*]**

TPEF microscopy utilizes mode-locked (pulsed) laser. Femtosecond-pulsed source allows readily extending TPEF to fluorescence lifetime imaging.

## 1.8 Fluorescence Lifetime Imaging Microscopy - FLIM

In the excitation process, the energy is supplied to the fluorophore by a light source, promoting the molecule to a higher energy state, the excited state (Figure 21). In the process of emission, the fluorophore returns to the ground state emitting a photon of energy that is inversely related to the wavelength, or directly related to the frequency of the light. The wavelength of the fluorescence photon will be longer, because the emitted energy is lower than the absorbed energy. This is due to dissipation of energy that occurred in the excited band. The separation between excitation and emission wavelength is known as Stokes shift (Figure 21).

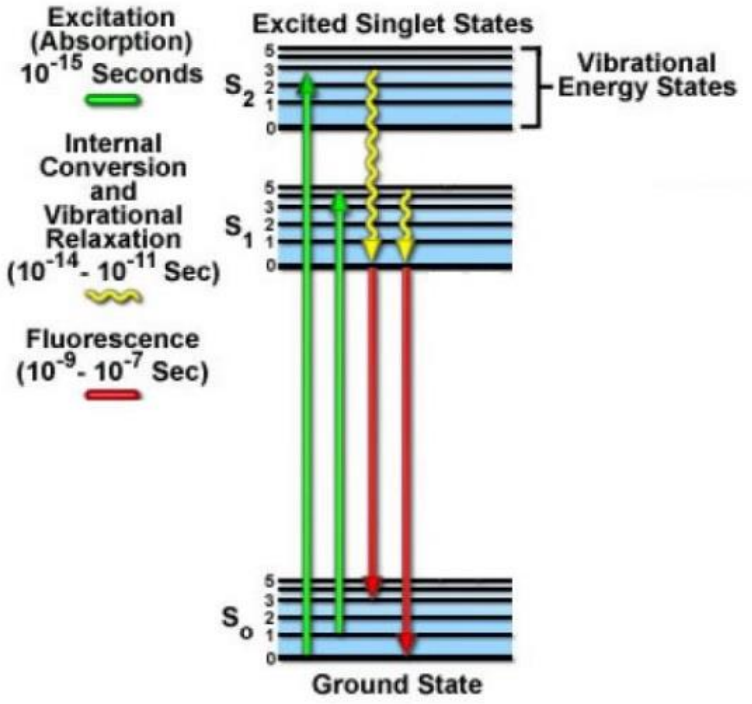


Figure 23 Stages of fluorescence

The fluorescence of molecular emitters is not only characterized by their excitation and emission spectrum, but also by their lifetime, which is the mean time in which a fluorophore stays in an excited state before returning to the ground state by emitting a photon. The emission of a fluorescence photon is a stochastic event, but it is possible to obtain information about the emission probability relatively to a molecular population, by measuring the lifetime of fluorescence. Fluorescence lifetime

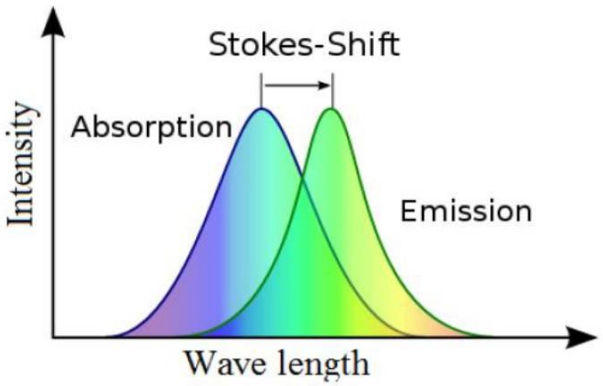


**Figure 24 Stokes Shift is the separation between excitation and emission spectra.**

measurements provide information about the micro-environment in which the fluorescence molecules are immersed, in fact the fluorescence lifetime is sensitive to ionic bond, oxygen concentration, collisions and energy exchanges with other molecules. There is a direct relationship between the concentrations of these quenchers and the measured fluorescence lifetime of a fluorophore.

Considering a set of molecules and exciting them with an infinitely short pulse of light (femtosecond), obtaining an initial population $N_0$ in the excited state, its decay rate is:

$$\frac{d}{dt}N(t) = -(\Gamma + k)\,N(t)$$

Where N (t) is the number of molecules in the excited state at time t, Γ is the radiative decay constants and *k* is the non-radiative decay constant. Through the integration of this equation with initial condition N (t = 0) = $N_0$, we obtain:

$$N(t) = N_0 e^{-t/\tau}$$

Where τ is the lifetime of the excited state:

$$\tau = \frac{1}{\Gamma + k}$$

The fluorescence intensity I(t), that is proportional to the population in the excited state, it is expected to decay exponentially. Usually, the lifetime of a population of

molecules can be calculated from the average time the population spends in the excited state [66]. In particular, considering anexponential decay curve, the lifetime of the decay is defined as the time period that has to pass before the number of excited molecules decay to a value 1/e, compared to the number of initial molecules.

$$N^*(\tau_m) = \frac{1}{e} N^*(0)$$

where $N^*$are the excited molecules, $N^*(\tau_m)$ are the excited molecules at t≠0 and $N^*(0)$ are the excited molecules are at t=0.

Fluorescence Lifetime Imaging Microscopy (FLIM) is a technique that allows to map in an image the measured fluorescence lifetime instead of fluorescence intensity, as it occurs in traditional imaging techniques [67]. In the early 1990s, the development of FLIM [68] allowed mapping the fluorescence lifetime of a sample with microscopic resolution. Imaging based on fluorescence lifetime has been used in wide field [69], confocal [70] and multiphoton [71] microscopy. FLIM uses the advantages of fluorescence lifetime to reveal the spatial distribution of a fluorescent molecule and information about its microenvironment. Through FLIM images is possible to observe the spatial localization of fluorophores and their respective fluorescence decay parameters.

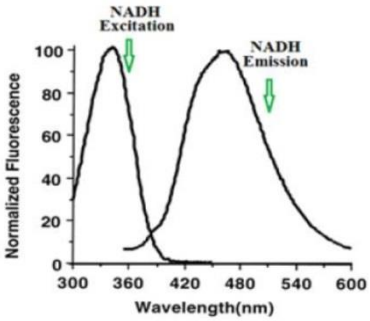


**Figure 25 Spectra of NADH excitation and emission**

FLIM can be used not only to discriminate the different fluorophores on the basis of their characteristic lifetime, but also to distinguish between different environments based on changes in lifetime of the same fluorophore. As fluorophores return to the ground state through radiative and non-radiative processes, the quenching of the excited state by external factors decreases the fluorescence lifetime. These changes in lifetime yields information about the micro-environment of the fluorophore [72]. In this study it has been used FLIM as through this technique it is possible to obtain sensitive measurements of the free and protein-bound NADH ratio, and to obtain information about the metabolic states distinguishing whether it is shifted on glycolytic or oxidative phosphorylation state [71].

There are two methods to derive the lifetime fluorescence from fluorescence measurements: one is related to measurements in the time domain and the other is related to frequency domain. In the first case, the sample is excited with a pulse; this method is based on the measurement of the arrival times of individual fluorescence of photons with respect to the arrival time of the excitation pulse. In the frequency domain, the phase shift of the fluorescence signal is measured with respect to a modulated excitation signal [66]. FLIM with two-photon excitation is almost always associated with time domain measurements.

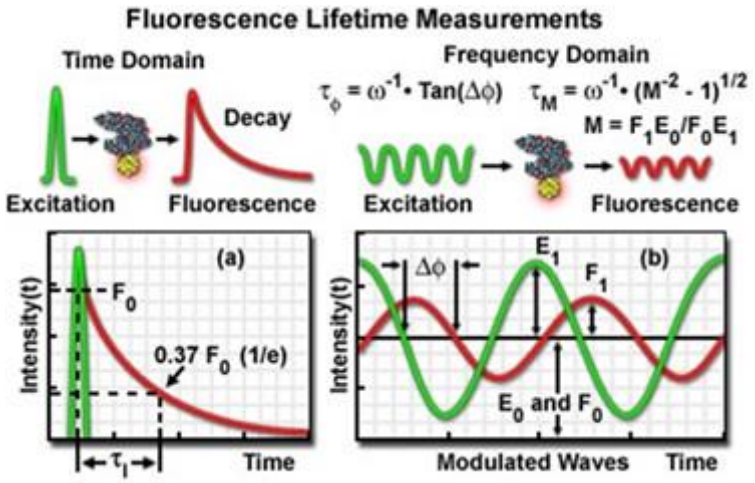


Figure 26 FLIM in the time domain and in the frequency domain

### 1.8.1 Time domain FLIM

The most used measurement technique in time domain is the Time Correlated Single-Photon Counting (TCSPC). TCSPC records a histogram of photon arrival times at each spatial location by using Photo Multiplier Tubes (PMTs) or comparable single photon counting detectors. Fluorescence emitted by a set of molecules excited by the laser pulse has an exponential decay over time. The TCSPC can reconstruct this distribution by measuring the time lags between the arrival time of the individual fluorescence photons and the excitation pulse. A measurement requires short excitation pulses of high intensity and fast detection.

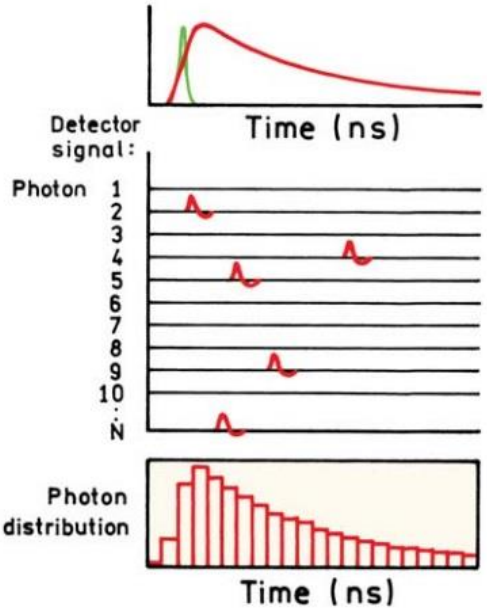


**Figure 27 Principle of TCSPC. The pulses in the middle panel represent the output from a constant fraction discriminator.**

Assuming that Rs is the repetition rate of the laser source and that Rd is the mean rate of fluorescence photons detection, the following condition

$$\frac{Rd}{Rs} = \alpha \ll 1$$

ensures that the probability of revealing two fluorescent photons for each excitation pulse is negligible. For the TCSPC, a value α <0.01 is generally required.

# 2 MATERIAL AND METHODS

## 2.1 Zebrafish utilized

It has been used the albino ($alb^{b4/b4}$) mutant that is characterized by a general deficiency in the production of melanin due to a mutation in the slc45a2 gene. Albino slc45a2 (solute carrier family 45, member 2) mutants completely lack melanocytes.

## 2.2 Zebrafish Facility

In the lab, zebrafish are kept in 1.5, 3, and 10 L tanks. They have a day-night cycle of 14 hour light and 10 hour dark. The water is continuously exchanged by the closed flow and the pumping and filtration system. In fact all the tanks are equipped with openings to allow a continuous replacement of water. The 10% of water are replacement daily, the water is supplemented by a saline solution suitable for the fish's needs (23.55g $CaSO_4$, 3g $NaHCO_3$, 15g Instant Ocean), and constantly maintained at a temperature of 28.5 °C and at a neutral pH. The feeding of Zebrafish consists of three daily meals: at morning and evening they receive a ration of live Artemia nauplii, which are small crustaceans. From the cyst stage the Artemia nauplii are hatched inside a special apparatus containing about 500ml of deionized water enriched with 30g of sea salt, here the cyst are constantly oxygenated and kept at constant temperature and ligthing. After two days Artemias can be distributed to zebrafish after being harvested, filtered to remove excess salt, the remains of empty shells and unopened cysts (which are indigestible) [73].

**Figure 29 the breeding tank; one male and one female are transferred to opposite sides of the breeding tank overnight.**

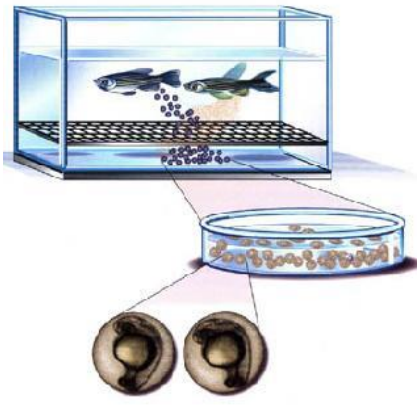

**Figure 28 Mating of zebrafish**

Usually the pairwise breeding is prepared in the afternoon after feeding, the breeding tank is filled with system water and then one male and one female are transferred to opposite sides of the breeding tank. This tank breeding is left overnight in the fish tank. The divider is removed the morning after at 9:00 am to allow mating. The eggs are collected, 1h following spawning, using a strainer and they are transferred to a Petri dish containing fishwater with 0.0002 % methylene blue and incubated at 28°C. The larvae are fed, starting from the sixth day of life, when all the reserve yolk has been fully absorbed. For the first three weeks of life, a ration of dry fish feed based on dehydrated artemies is given.

## 2.3 Microinjection

As stated above, zebrafish have the advantages that their genetics can be manipulated; indeed the early stage embryos can be easily microinjected. Through microinjection it is possible to convey genetic material or transient knock-down of genes into the blastomeres: the embryonic cells sitting atop the yolk of the newly fertilized egg. The solution is injected into the yolk, the deliver into the cytoplasm is reached by cytoplasmic movements that take place after the injection.

For the microinjection we used the glass-needles microinjection capillary tubes without filaments (TW-100F, World Precision Instruments, FL). These glass needles were pulled and separated into two similar sized microinjection needles with a microelectrode puller (Sutter Instrument). The tips were held longitudinally and heated in the middle until it gets broken in two parts. The part where it has broken is cut off to create an opening of about 5µm.

On the micropipette puller the following settings have been entered:

- heat 645
- pull 80
- velocity 80

If the pipette is too thin there is the risk that there isn't the tensile strength to penetrate the chorion and break when forced onto the chorion surface; while the thicker pipettes do not easily slip out of the chorion hazarding to breach it. For this reason needles must be of a consistent size to allow a precise injection of materials.

The zebrafish embryos were microinjected before four-cell stage, ideally at the one-cell stage, using a microinjector (Eppendorf).

## 2.4 The method used to do the microinjection

The embryos during the microinjection are deposed on a Petri dish containing a microscope slide. The embryos are aligned along one side of slide. As the needle penetrates the chorion, the embryo is forced against the rear of the slide moving only a little.

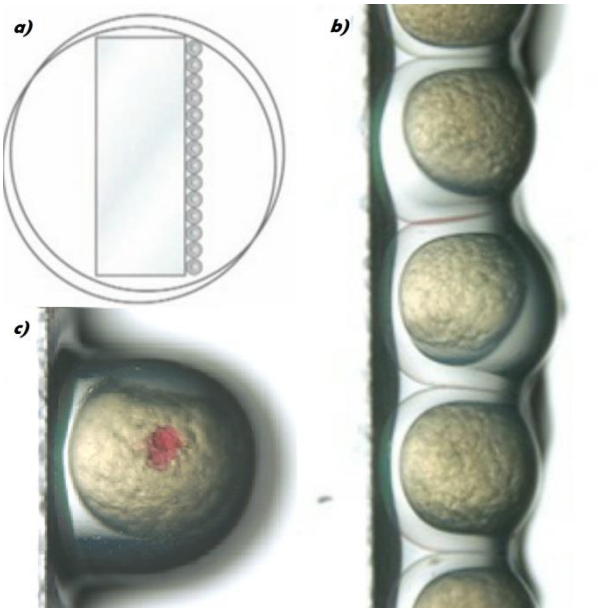


**Figure 30 a) Embryos to be injected are lined up against a microscope slide in a Petri dish; b) Embryos are aligned long the sides of slides; c) Immediately after injection, the morpholino or mRNA is visible as a punctuate spot in the yolk.**

The volume of microinjections can be regulated by setting the pressure and duration of pulses of air. The glass needles are in fact held and connected to the airline of the injector. The micromanipulator allows moving the needle through accurate adjustments so to position it close to the egg.

In this study the injection is due into the yolk.

## 2.5 Mounting

For more precise orientation of zebrafish embryos and to keep them from floating during long term observations, Zebrafish are mounted using low melting point agarose at 0.1% between a microscope slide and a cover slide The agarose is prepared dissolving the low melting point agarose powder in a defined volume, the mixture is heated up in a microwave and mixed until the agarose is completely dissolved. The aliquots can be stored at 4 °C. This solution remains liquid at 37-40°C, but quickly jellifies when cooled.

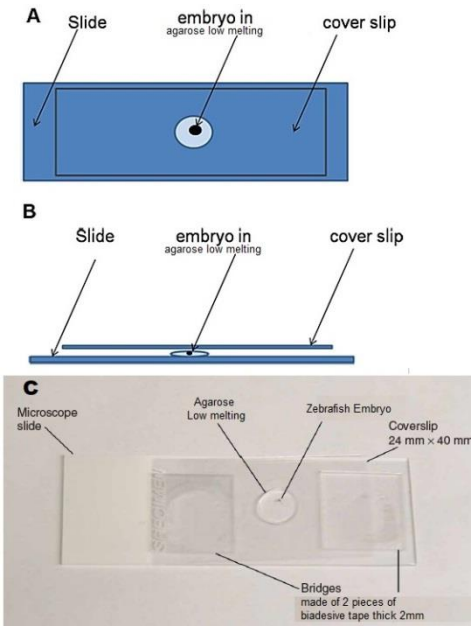


**Figure 31 A) mounting of zebrafish embryo on a slide from above; B) from lateral side; C) photo of embryo embedded in agarose low melting between two a microscope slide and a cover slides**

## 2.6 Sample heater

A sample heater for slides has been designed and realized in order to allow maintaining the temperature constant in time around 28.5°C. The heater is composed by a metal plate on which are mounted 4 heating resistors connected to a thermostat and a sensor. To maintain the temperature constant is very important as zebrafish is a poikilothermic animal, then its body temperature varies with the ambient temperature and this involves some physiological responses [74] like the increasing of food intake, metabolic rate and sympathetic activity that could mask the metabolic phenotype under analysis. This support permits to choose the temperature and maintain it constant during the measurement.

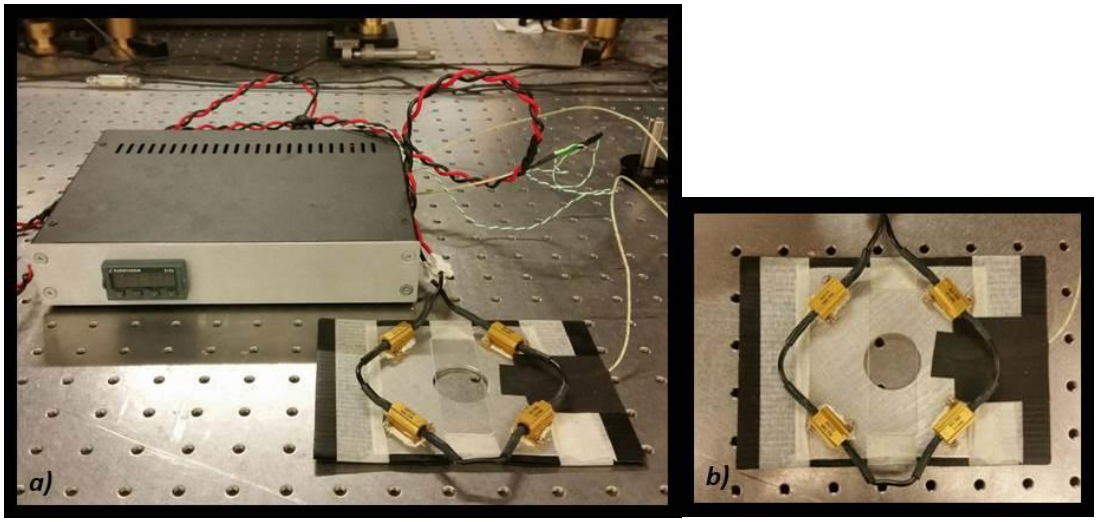


**Figure 32 Custom-made sample heater, used to mantain the zebrafish embryo at a constant temperature.**

## 2.7 Experimental set up

The experimental setup consists of a custom-made multiphoton microscope. The optical system is mounted on two stainless steel optical breadboards, one horizontal (1800 mm x 1200 mm) and one vertical (1200 mm x 750 mm), each ones with a grid of M6 threaded holes with a pitch of 25 mm. The vertical breadboard is fixed to the horizontal one, which in turn is placed as a top on a granite optical table. The optical table is held by four reinforced concrete legs. A neoprene layer about 1 cm thick was inserted between the optical table and the horizontal base in order to damp mechanical vibrations.

In the experimental setup, the excitation source is a pulsed Ti:Sapphire laser (Mira900F, Coherent, Santa Clara, US) emitting 140 fs pulses at 76 MHz repetition rate. The emission wavelength can be tuned between 700 nm and 920 nm. The Ti: Sapphire laser is pumped by a Nd:YAG laser, duplicated in frequency, emitting at 532 nm (Verdi V10, Coherent, Santa Clara, USA). The output beam is collimated by a telescope, composed by L1 and L2. An electronic shutter S (SH05, Thorlabs, Newton, NJ, USA) minimizes the permanence time of the laser on the sample. The beam power is regulated by a λ / 2 waveplate and a polarizing beam splitter cube (PBS). The waveplate can be rotated by a motor (NSR1, Newport, Irvine, CA, USA). The polarization of the electric field incident is rotated and therefore only a part of this is transmitted by the PBS. The scanning head consists of two orthogonal galvanometric mirrors VM500 (GSI Lumonics, Karlsruhe, Germany). Before the sample, there is a beam expander for beam sizing to a size of about 1 cm, a dichroic mirror FF685-Di02 (Semrock Inc, Rochester, NY, US), and a water immersion objective Plan-Apochromat 20× XLUM (Olympus - Shinjuku, Tokyo, Japan), NA 0.95, WD 2 mm.

Fluorescence light is collected by the same objective lens used for the excitation and reflected by the dichroic to the detection path. The detection system is composed by two photomultiplier tubes H7422 (Hamamatsu, Hamamatsu City, Japan) and a fast detector PMH-100 (Becker-Hickl GmbH, Berlin, Germany). To acquire NADH fluorescence, light is reflected by a dichroic mirror FF495-Di01 (Semrock Inc, Rochester, NY, US), it passes through a band-pass filter FF01-460/30 (Semrock Inc, Rochester, NY, US) and it is detected by one photomultiplier tube (PMT). Instead, FAD fluorescence is transmitted by the same dichroic FF495-Di01 (Semrock Inc, Rochester, NY, US) and it passes through a band-pass filter FF01-520/20 (Semrock Inc, Rochester, NY, US) before being detected by the other PMT.

Fluorescence signal can be coupled to a multimode optical fiber by means of a 10× objective lens Plan (Nikon, Tokyo, Japan) and detected using the detector PMH-100 (Becker-Hickl GmbH, Berlin, Germany). Then the detected signal is processed by a single photon counting FLIM board SPC-730 (Becker-Hickl GmbH, Berlin, Germany) for time--resolved analysis of fluorescence.

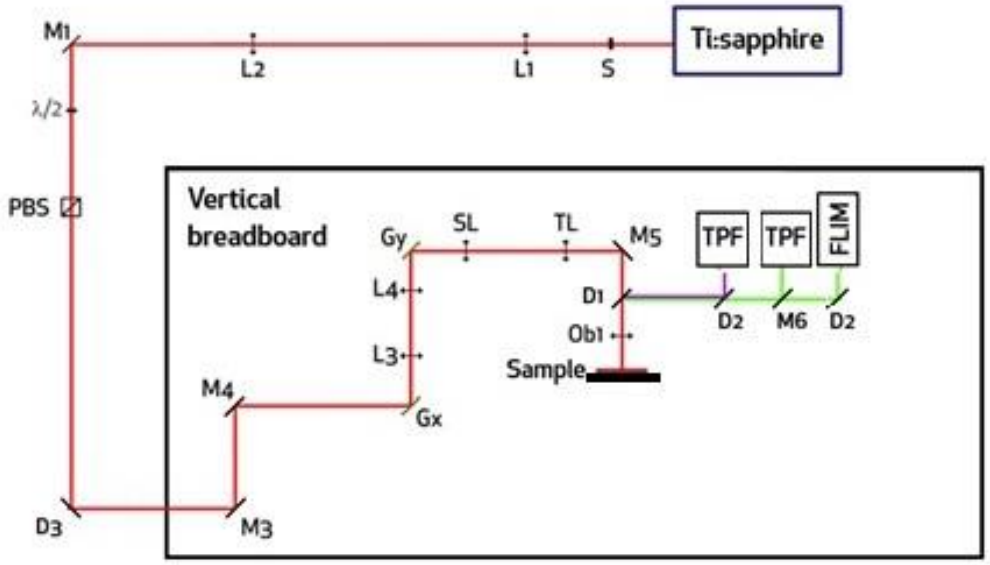


Figura 33 Sketch representing the optical scheme of the experimental setup for TPEF and FLIM.

## 2.8 Calibration

The setup needs to be calibrated because the PMTs are positioned at different distances from the sample, and this means that the efficiency of the detection is different. Besides, each PMT has its own amplifier through which the gain is adjusted and this can be adjusted according to the needs. Furthermore, the PMTs efficiency can change after being exposed a

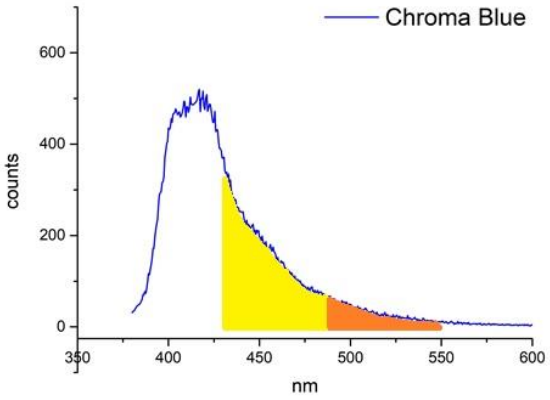


Figure 34 – Fluorescence spectrum of the blue autofluorescent plastic slide through a spectrophotometer. In yellow and orange the spectral bands corresponding to NADH filter and FAD filter, respectively.

high intensity of the signal. In general, the calibration was performed to ensure reproducibility of the measurements. In order to obtain the same experimental conditions for each acquisition, before starting each measurement session, the setup was calibrated using a blue fluorescent plastic slide (Chroma Technology Corp). This blue fluorescent plastic slide was chosen as calibrating sample after having acquired several spectra of different Chroma Slides and different Coumarin solutions (6, 102, 153) through a spectrophotometer (PerkinElmer LS55). The idea was to search for the best spectrum to be used for calibrating the intensity ratio between the two spectral ranges corresponding to the filters used (FF01-460 /30 for NADH and FF01-520 / 20 for FAD).

We calculated that the ratio of the areas under the emission curves, in the two

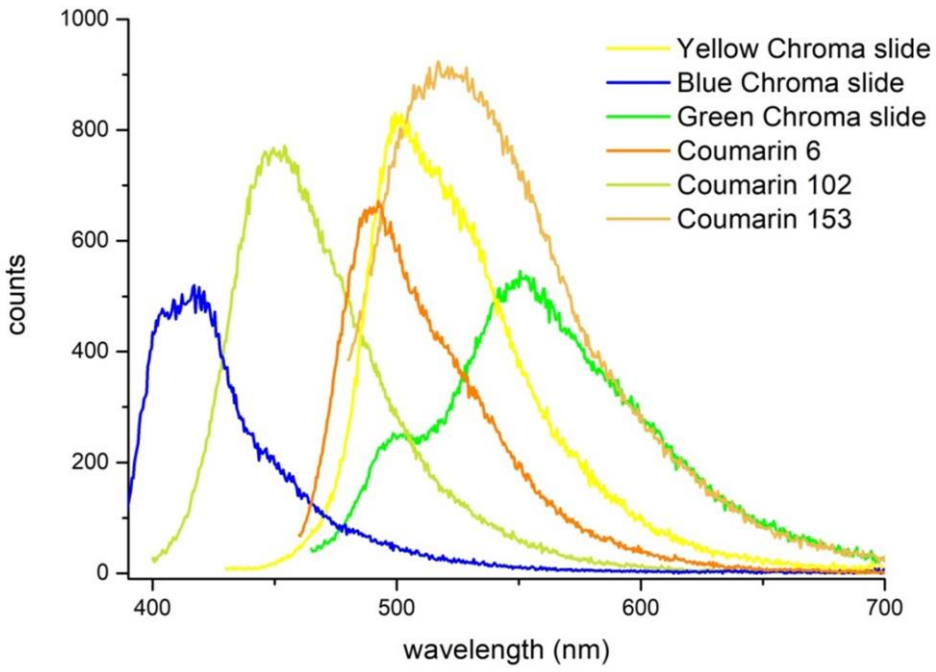


**Figure 35 Emission curve of Coumarin 6, Coumarin 102, Coumarin 153, blue Chroma autofluorescent plastic slide, green Chroma autofluorescent plastic slide, and yellow Chroma autofluorescent plastic slide acquired by spectrophotometer (PerkinElmer LS55)**

spectral ranges corresponding to the filters used give the following intensity ratio.

$$I_{ratio} = \frac{\int_{430}^{490} f(x)dx}{\int_{490}^{550} f(x)dx} = 5.6$$

The calculated intensity ratio allows adjusting the gains of the two PMTs in order to have always the same value for the blue autofluorescent slide.

## 2.9 Image acquisition, processing and analysis

### 2.9.1 TPEF - Image Acquisition

As previously stated in paragraph 1.5, the biochemical estimation of NADH and FAD relative abundances has been extensively used to monitor cellular energy metabolism *in vivo* [75]. The fluorescence intensity ratio between NADH and FAD depends on the changes in the cellular metabolic rate and on the vascular oxygen supply.

Considering that an approximation of the oxidation-reduction ratio of the mitochondrial matrix space can be determined from the "redox ratio", the ratio between the fluorescence intensity of NADH divided by the fluorescence intensity of FAD was calculated for each acquired image.

TPEF images were recorded with a pixel dwell time of 20 µs, a field of view of 200 × 200 µm$^2$ and a resolution of 512 × 512 pixel$^2$:

- 512x512 pixel
- Field of view: 200 µm /400 µm /600 µm
- $\lambda_{exc}$ = 740 nm

As the laser we are working with does not permit to change continuously the wavelength setting it was decided to use the $\lambda_{exc}$ 740 nm to excite in the same time both the fluorophores NADH and FAD. This decision was due not only for the simultaneously excitation of NADH and FAD, but also because zebrafish were not in their natural environment but were embedded in agarose so it was preferable to reduce their exposure to laser beam as more as possible acquiring the images at the

same time for both fluorophores. In this way the data acquired were not altered previous analysis.

Before starting the measurement, we acquired the images from a blue Chroma fluorescent plastic slide to calibrate the set up. The gains of the PMTs were regulated in order to have the average ratio between the 2 channels equal to 5.6 (from the channel where is the filter FF01-460/30 and from the channel with FF01-520/20), and this procedure was repeated at the end of the measurements to verify whether any changes had occurred.

### 2.9.2 TPEF - Data Analysis

The ImageJ software (National Institutes of Health) was used for TPEF analysis to obtain the NADH/FAD ratio about muscle, spinalcord and intestine of the zebrafish larvae. The choice of measuring the redox ratio by NADH/FAD instead of a normalized redox ratio NADH/(FAD+NADH) was due to the fact that utilizing the ratio NADH/FAD the dynamic range is improved. In fact when the FAD intensity is much less compared to NADH intensity the ratio tends to 1 and so the measure loses sensitivity. So we can obtain images intensity ratio with better contrast respect to the images obtained from the normalized redox ratio. For this kind of studies in literature we usually find the use of the normalized redox ratio but in our study using only the wavelength at 740 nm to excite simultaneously both the fluorophores when the contribution of FAD is low, the images obtained using the normalized redox ratio had a weak contrast.

The images obtained from the acquisition have been elaborated through ImageJ. For each analysis, as mentioned in paragraph 1.7, two images are saved in .txt format: one for the intensity information of NADH and one for FAD. In the two images is selected the same region of interest (ROI) is selected in each image and is cropped. The two cropped images containing the same region are threshold in order to cut off the signal coming from the nuclei. Then, a ratiometric image is calculated through the control “Process” -> “Image calculator”, from which we obtain the histogram and the mean. This process is repeated for all the images acquired. The entire mean values obtained are then elaborated in graphs through Microcal Origin software. The graphs obtained

provide data in which is possible to compare the values of intensity ratio in tissue and organs of treated and untreated zebrafish larvae.

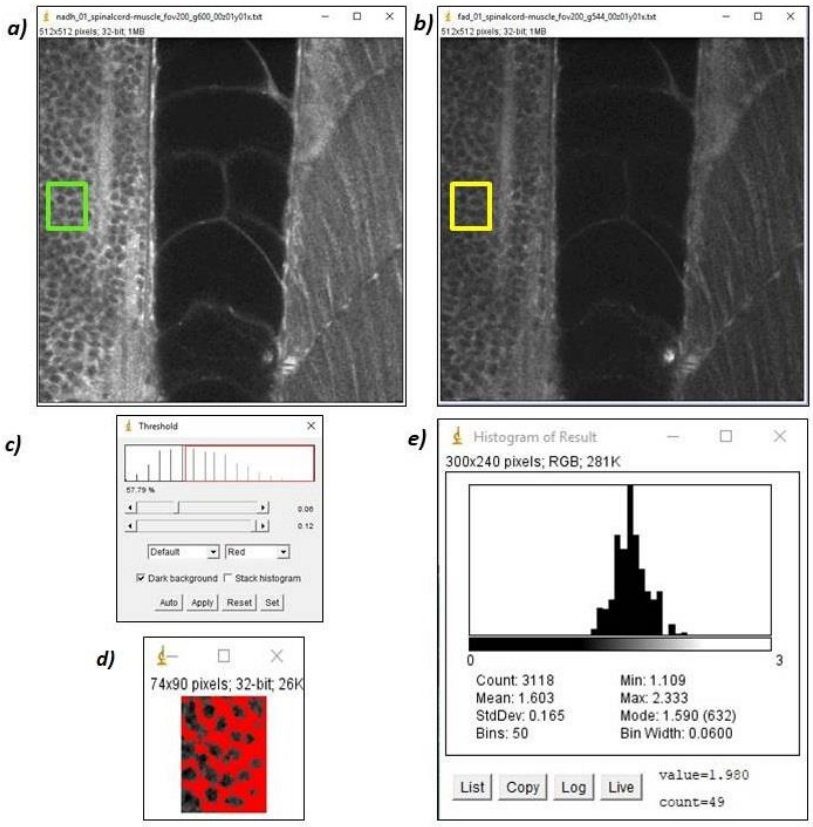


**Figure 36 a) NADH fluorescence image, in green the selected ROI for the analysis; b) FAD fluorescence image, in yellow the selected ROI; c) the threshold chosen to cut off the contributes coming from the nuclei; d) the ROI where in red is selected the area without the nucleus; e) histogram and mean obtained from ROIs ratio**

The spectral emission of NADH and FAD in figure 37 shows that there is a crosstalk of NADH spectra on FAD, where NADH emission curve bleeds in FAD curve.

As possible to see in Appendix the measurements were corrected considering the NADH bleeding in FAD channel.

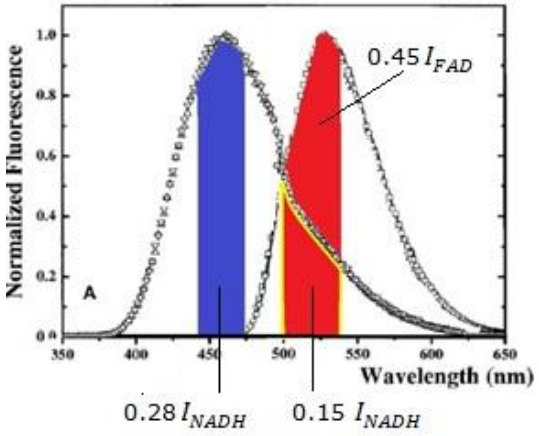


**Figure 37 spectral absorptions and emissions of NADH and FAD**

### 2.9.3 FLIM – Image acquisition

The fluorescence lifetime of NADH depends whether it is in a free or protein-bound state. The short lifetime of NADH in its free state is due to dynamic quenching by the adenine moiety [76], while the long lifetime of protein-bound NADH changes depending on the enzyme it is bound to [77]. The acquisitions of NADH lifetimes were performed using a band-pass filter FF01-460/30 (Semrock Inc, Rochester, NY, US) and a PMH-100 (Becker-Hickl GmbH, Berlin, Germany) detector. For each acquisition we used:

- field of view = 200 × 200 $\mu m^2$;
- spatial resolution = 128 × 128 pixels;
- acquisition time = 120 s
- $\lambda_{exc}$ = 740 nm

### 2.9.4 FLIM - Data Analysis

The SPCImage software shows the fluorescence signal collected at each point of the image and allows deconvolving the acquired data from the instrumental response function (IRF) and fitting with an exponential decay function. In these analyzes a bi-exponential fit was used to separate two contributions of decay: a fast and a slow lifetime components. The measured fluorescence decay in a biological sample results from the combination of several contributions as the sum of several exponential decays. The function F(t) of the fluorescence intensity as a function of time I (t) was approximated at every point of the image:

$$\mathbf{F(t) = \frac{I(t)}{I_0} = a_1 \exp(-t/\tau_1) + a_2 \exp(-t/\tau_2)}$$

where $I_0$ is the integral of the fluorescence intensity in the fitting range, $\tau_1$ is the shortest lifetime component, $\tau_2$ is the longest component, and $a_1$, $a_2$ are the relative contributions of the lifetime components. Thus, the mean fluorescence lifetime $\tau_m$ of the observed point is given by:

$$\boldsymbol{\tau_m = \frac{a_1\tau_1 + a_2\tau_2}{a_1 + a_2}}$$

With SPCimage it's possible to select one of the decay parameters resulting from the fit procedure to create a parameter map.

The ranges for lifetime parameters selected for our lifetime analyses were:

$1000 < \tau_m < 5000$

$0 < \tau_1 < 3000$

$2000 < \tau_2 < 8000$

$0 < a_1/a_2 < 5$

In the Figure 38 it is displayed the interface of SPCImage program.

The *Threshold*-parameter defines the minimum number of photons in the peak of a fluorescence curve which are necessary in order to take the fluorescence decay into account. The feature can be used to suppress "dark" pixels which are skipped during calculation process. This will not only accelerate the calculation process but also improve the quality of the parameter histogram since outliers due to a bad signal-to-noise ratio will be suppressed.

The *Selected fit parameter* shows the weighted average of the different lifetime component in each pixel ($t_m = \tau_m$), this parameter can be changed with another one obtainable from fit ($a_1$, $a_2$, and so on).

The *Binning* factor denotes the number of surrounding pixels which are summed into each decay trace. The number of photon in each decay trace will increase effectively if the binning value is incremented. The spatial resolution will decrease since the binning strategy is used for all the pixels within the region of interest during the fit process.

Deviations between photon data and fit-trace are represented graphically by the weighted residuals at the bottom of Figure 38. To check if the chosen model for the fit is appropriate the reduced $\chi^2$ should be displayed.

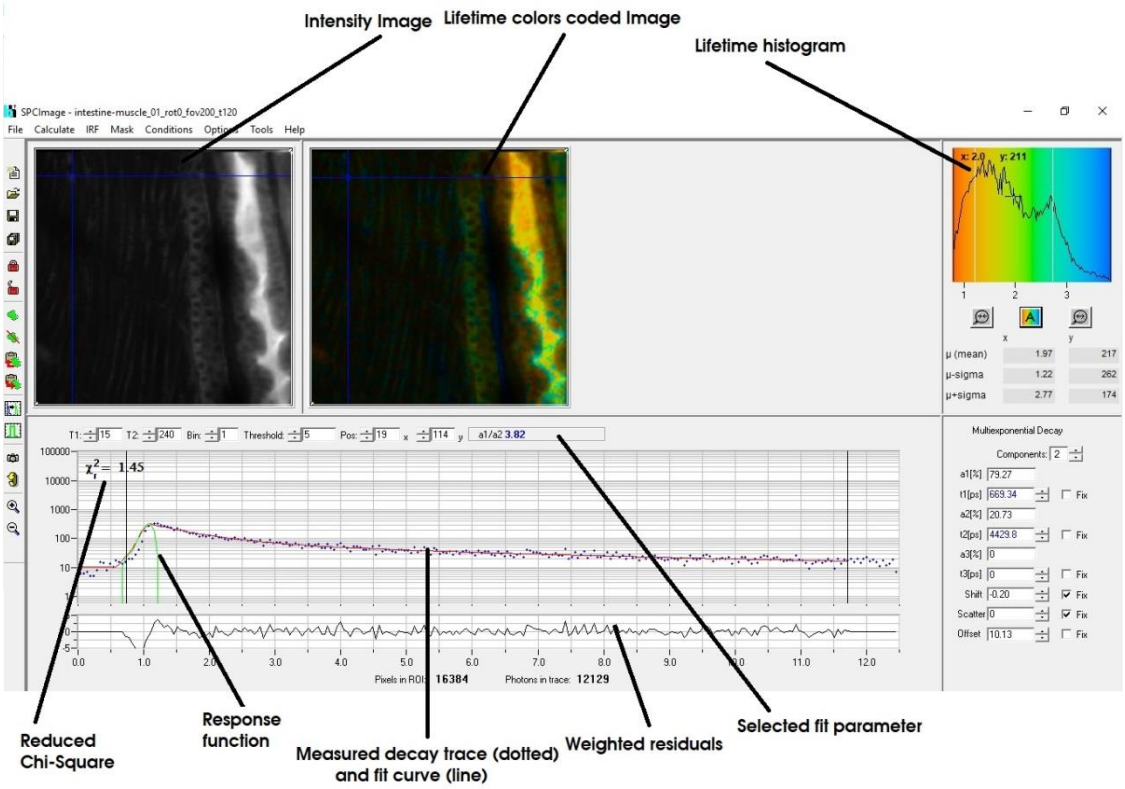


**Figure 38 Graphical interface of SPCImage data analysis. In gray scale there is the intensity of two-photon fluorescence and in false colors there is the lifetime of fluorescence $\tau_m$ (where red corresponds to 0 ps and blue to 6000ps). The histogram of $\tau_m$ is at the top right. Under the images there is a scatter plot (in blue) showing the number of fluorescence photons detected versus the arrival time, with superimposed (in red) the bi-exponential fit function, while in green it is showand the instrument response function (in green). These data were acquired through FLIM measure of muscle and spinal cord in zebrafish larva at 5 dpf.**

# 3 RESULTS AND DISCUSSION

Mitochondrial diseases are a large group of pathologies associated with defects in mitochondrial energy metabolism, due in particular to anomalies in oxidative phosphorylation (OXPHOS). The aim of this study is to characterize by nonlinear microscopy the metabolic state in Zebrafish larvae subjected to different methods that reduce the activity of oxidative phosphorylation inducing hypoxia or activating the HIF signaling, that mimics the lack of oxygen, and the interference of MOpolG on mitochondria replication.

## 3.1 Morpho-functional imaging of zebrafish larvae tissues by Two-Photon Excited Fluorescence

First, to understand if the use of TPEF and FLIM microscopy, in the same optical system and with label-free imaging (i.e. relying only on the intrinsic fluorophores responsible for autofluorescence), could provide full anatomical mapping in Zebrafish larva *in vivo* we acquired full 3D images of the larvae.

The acquisition parameters used for TPEF are:

512x512 pixels

Field of view: 200x200 $\mu m^2$ /500x500 $\mu m^2$

$\lambda_{exc}$ = 740 nm

$\lambda_{collected\ to\ NADH}$= 460/30 nm

$\lambda_{collected\ to\ FAD}$= 520/42 nm

We imaged zebrafish larvae at 2, 3, 4, 5 and 6 days post fertilization (dpf).

To identify exactly the different organs it was used the Zebrafish Atlas where it is possible to view anatomical parts within the context of a virtual slide with the possibilities to zoom and scroll the illustrated parts. The Zebrafish Atlas contains 2- and 3- dimensional anatomical references slides of zebrafish. The zebrafish images are scanned from hematoxylin and eosin histological slides.

In the following images, the acquisitions of a zebrafish larva at 5dpf are shown. The larva is shown in 3 sections: head, thorax and caudal zone.

In Figure 39 the images taken from two z-stacks are shown. The images in panel b) are acquired in coronal section; here it is possible to observe the eyes and the inner ears. In the eyes we can see the photoreceptors, the inner plexiform layer and the lens, while in the inner ears we observe the rostral otolith.

The images in panel c) show the acquisitions in sagittal section. In these images we can distinguish more parts of layers of the neuroretina: starting from the acquisition of outer layer we can observe retinal pigmented epithelium, photoreceptor, inner plexiform, bipolar and amacrine cells and lens. Then there are: the midbrain⑤, pharyngeal arches⑥, operculum⑦ and, in the inner ear③, the caudal otolith④.

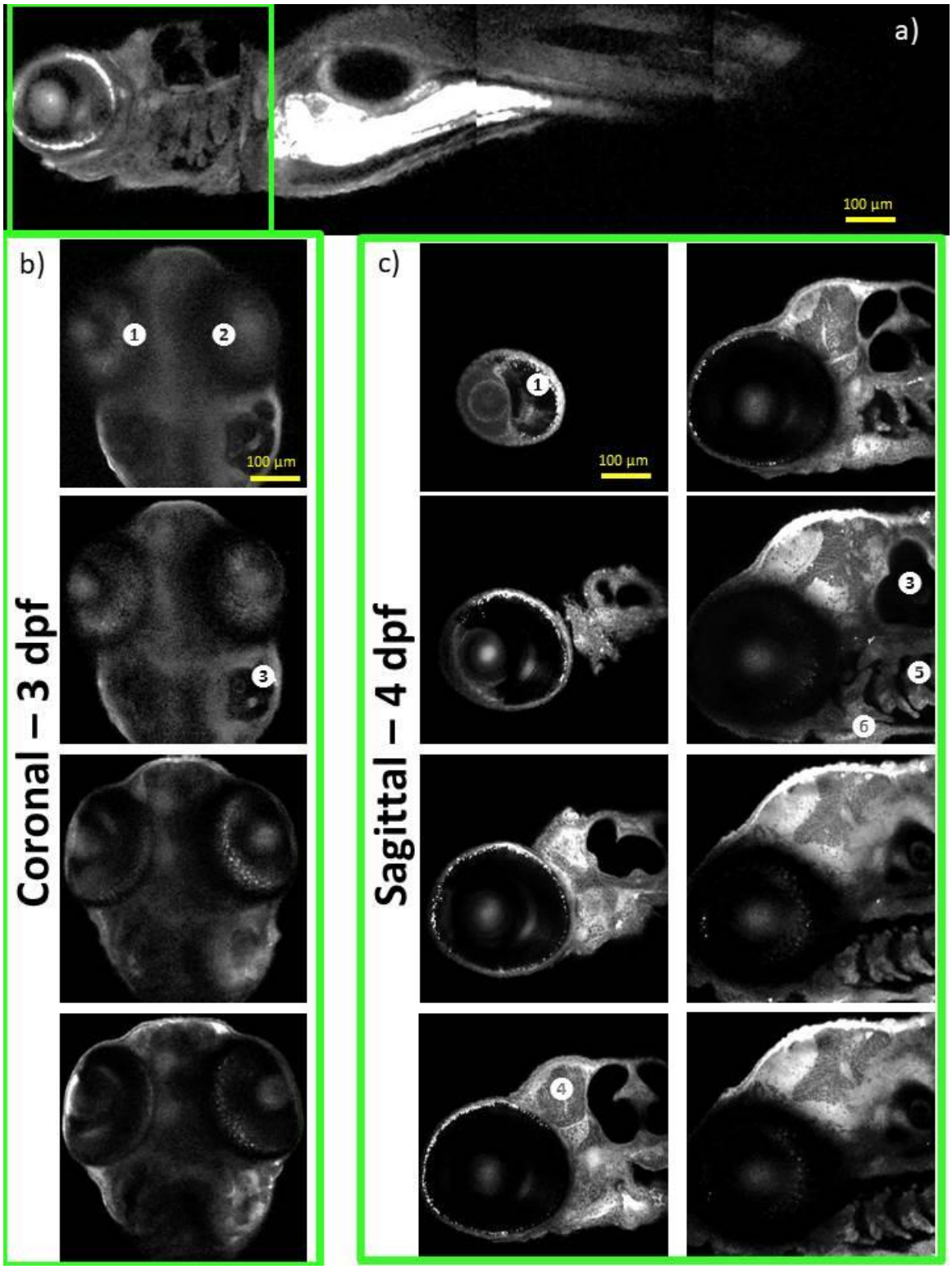


**Figure 39 Label-free TPEF acquisitions of zebrafish larva at 5 dpf – a) stitching of 4 images to create the image of the whole larva; b) representative images of a coronal z-stack of the head with z-step of 5 µm; c) representative images of a sagittal z-stack of head larva, with z-step of 5 µm; ① and ②eyes, ③the inner ear, ④the caudal otolith, ⑤the midbrain, ⑥pharyngeal arches, ⑦operculum; $\lambda_{exc}$ of 740nm and $\lambda_{collected\ to\ NADH}$= 460/30 nm**

Figure 40 shows a sagittal z-stack of the thorax. Owing to this z-stack it is possible to observe in detail ①the intestine, ②the yolk, ③the swim bladder and ④the caudal vein.

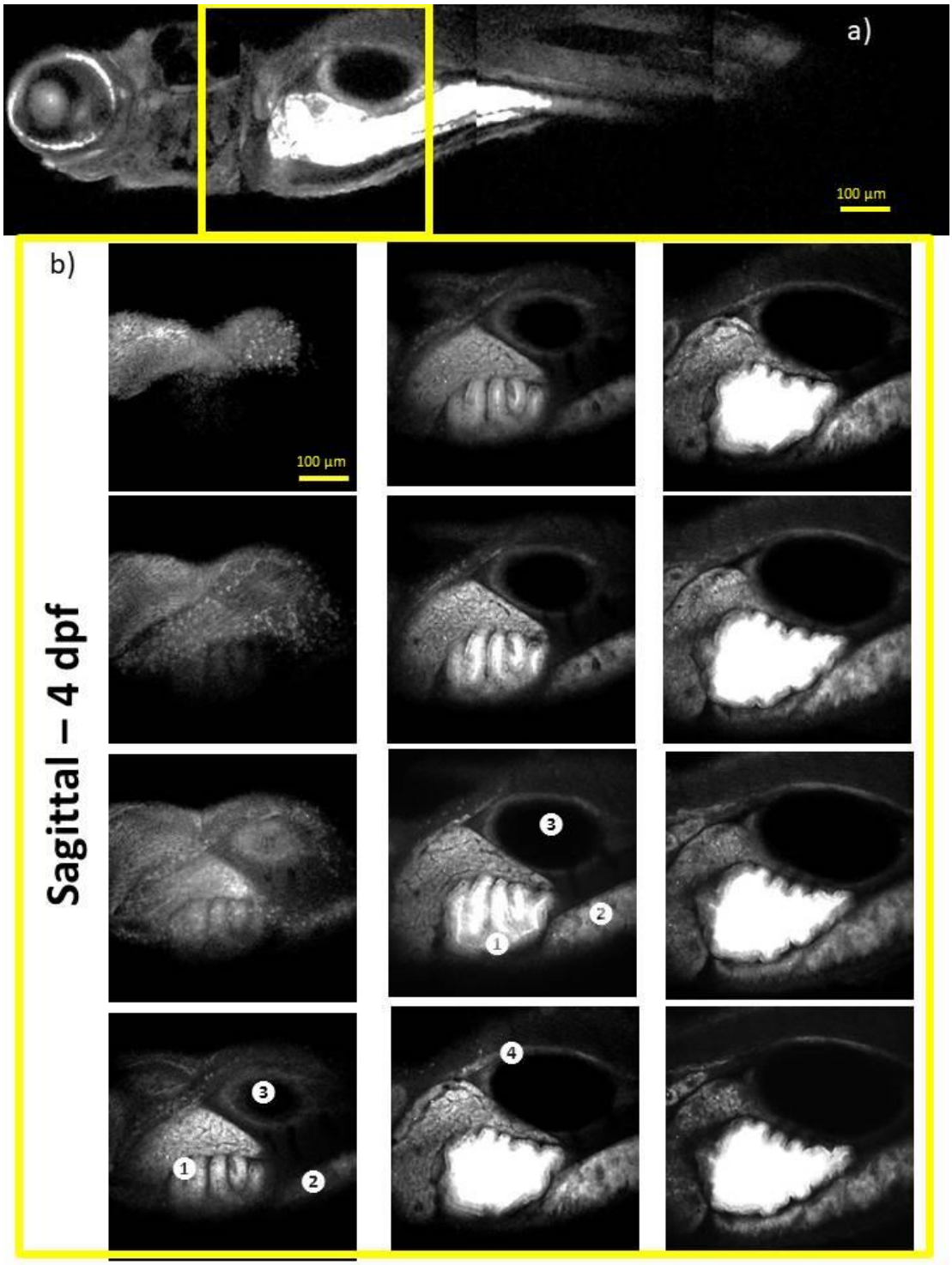


**Figure 40 acquisitions of zebrafish larva at 5 dpf - a) stitiching of 4 images to create the image of the whole larva; b) representative images of a sagittal z-stack of the thorax larva, with z-step of 5 µm; ①the intestine, ②the yolk, ③the swim bladder and ④the caudal vein; $\lambda_{exc}$ of 740nm and $\lambda_{collected\ to\ NADH}$= 460/30 nm**

In Figure 41 the caudal zone is shown, the stack is acquired in sagittal section. Starting from the acquisition of outer layer in these images we can see: ①the somatic muscle and myotomes, ②the end of the yolk, ③the segmental vessels, ④the caudal cardinal vein, ⑤the intestine, ⑥the notochord and ⑦the spinal cord.

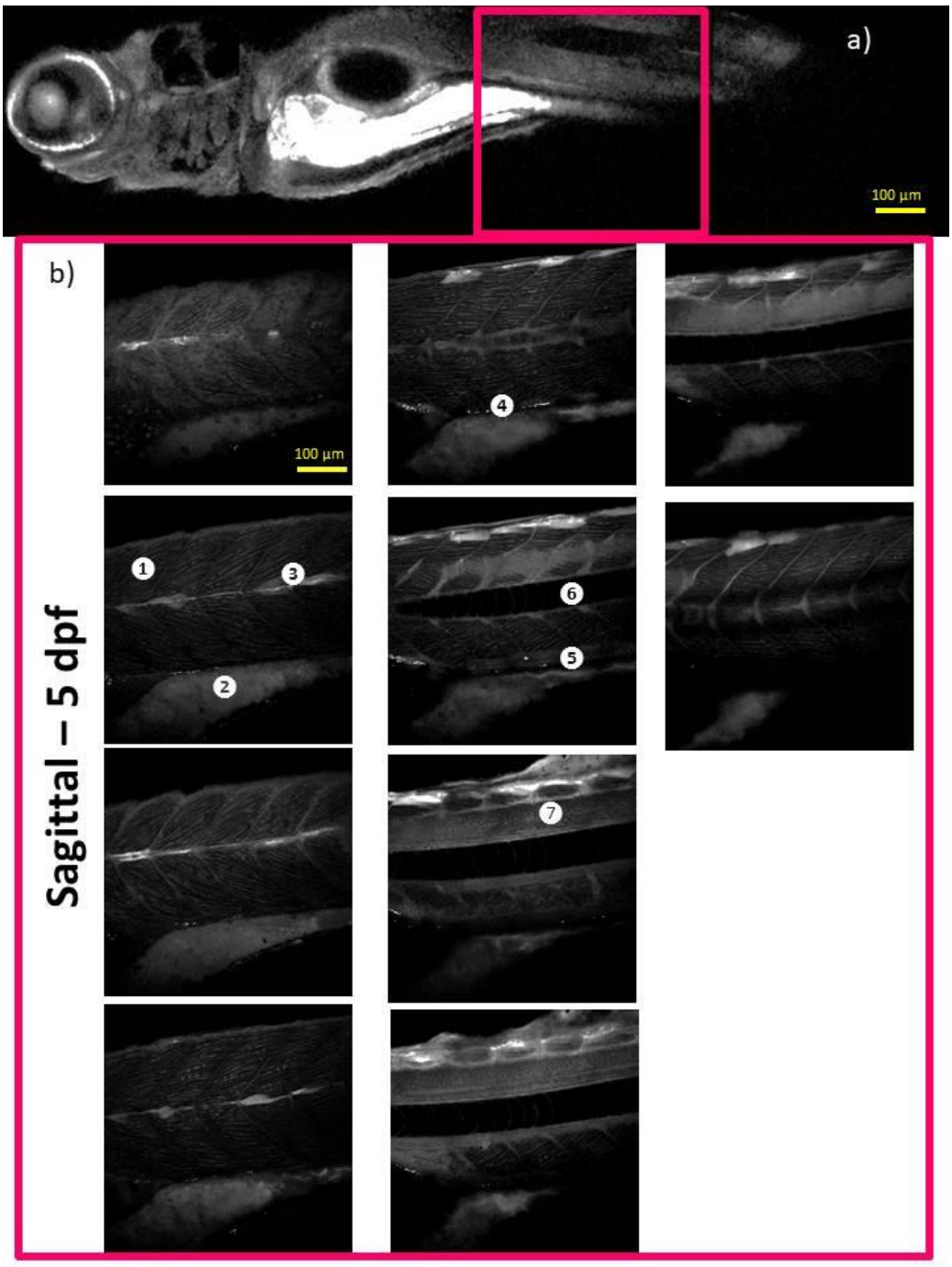


**Figure 41 acquisitions of zebrafish larva at 5 dpf - a) stitching of 4 images to create the image of the whole larva; b) representative images of a sagittal z-stack of the proximal tail region, with z-step of 10 µm; ①the somatic muscle and myotomes, ②the end of the yolk, ③the segmental vessels, ④the caudal cardinal vein, ⑤the intestine, ⑥the notochord and ⑦the spinal cord; $\lambda_{exc}$ of 740nm and $\lambda_{collected\ to\ NADH}$= 460/30 nm**

Figure 42 shows a detail acquired with a FOV of 200 µm in four different areas: in panel b) the epithelium, in c) the muscle, in d) the liver and intestine, in e) the spinal cord.

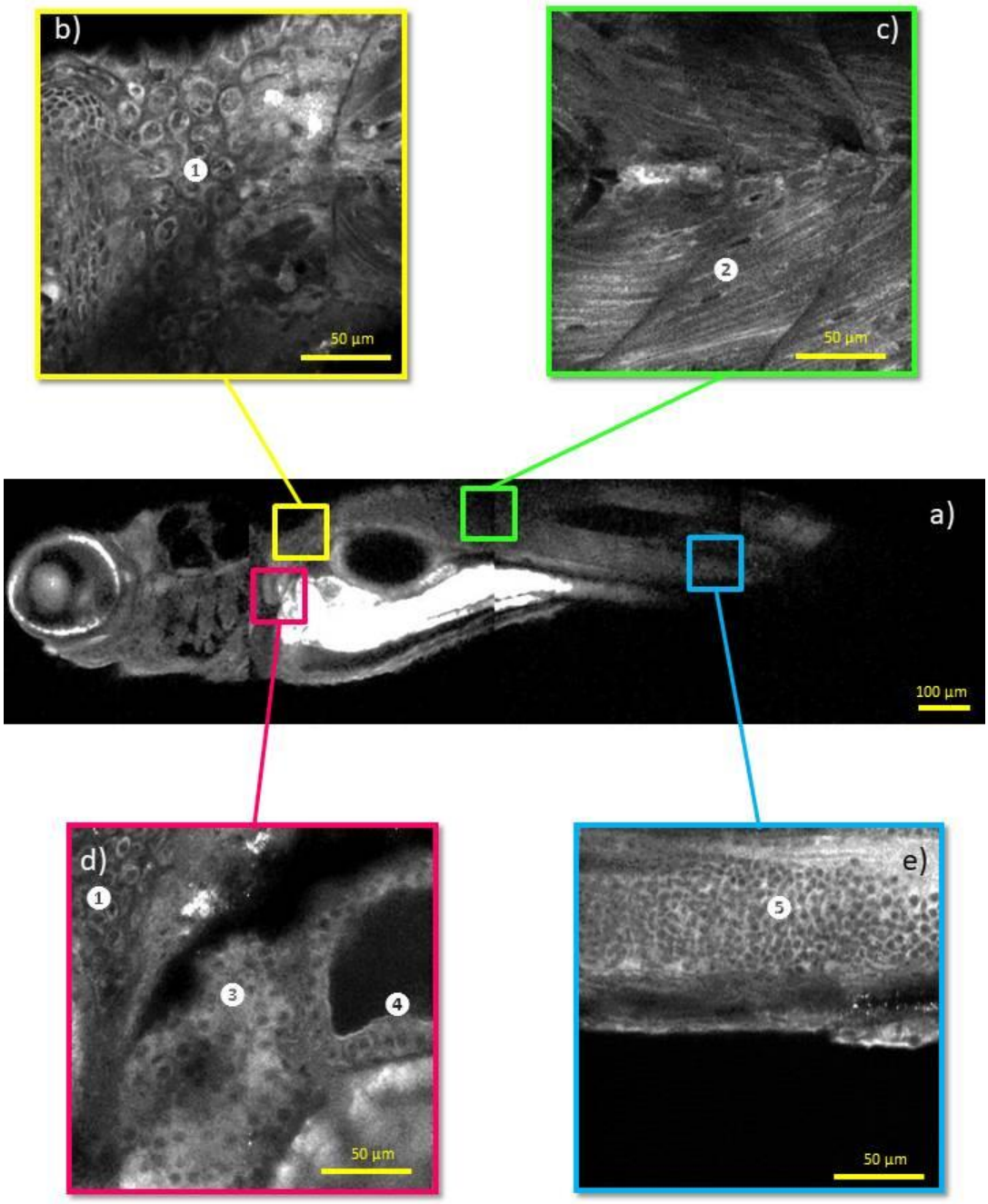


**Figure 42 acquisitions of zebrafish larva at 5 dpf - a) stitching of 4 images to create the image of the whole larva; the images [b) epithelium, c) muscle, d) liver and intestine, e) spinal cord area] are acquired with a 200 µm FOV with $\lambda_{exc}$ of 740nm and $\lambda_{collected\ to\ NADH}$= 460/30 nm; ①epithelium, ②muscle, ③liver, ④intestine, ⑤the spinal cord**

In Figure 43 it is possible to observe the comparison between a histological image, labeled with hematoxylin and eosin, obtained from a physical slice of zebrafish larva at 4 dpf cut and an optical slice acquired *in vivo* from a larva at 4dpf by means of NADH autofluorescence. In the NADH intensity image we can clearly distinguish all the tissues that we see in the histological image. The comparison between histological and TPEF images of intensity of NADH of zebrafish was possible as the Zebrafish Atlas that contains 2- and 3-dimensional, anatomical reference images of zebrafish hematoxylin/eosin histological slides, at various stages of development [78].

In panel b) of Figure 43 it is possible to discriminate the muscle in the region marked with ①. Here the myotomes, that are the portion of a somite from which skeletal musculature is produced, are well distinguishable also in TPEF image.

In region ② there is the swim bladder. In the TPEF image the swim bladder appears totally black because being a hollow. The swim bladder is a double-chambered organ located in the coelom that contributes to the ability to control buoyancy. The swim bladder also functions as a resonating chamber, to produce or receive sound [78].

In the portion of intestine, at point ③, the cylindrical epithelium cells are well visible. The intestine of zebrafish is composed by a thin layer of connective tissue that divides the epithelium at the base of the folds from the inner circular layer of smooth muscle. The intestinal epithelium is arranged in broad, irregular folds while in mammalians is arranged in villi, furthermore it lacks crypts of Lieberkuhn [79].

The yolk, shown in region ④, exhibits strong fluorescence, possibly due to retinoids and oxidized lipids [80].

The pancreas, at point ⑤, is a lobulated gland organ in the digestive and endocrine systems. It is both exocrine, secreting pancreatic juice containing digestive enzymes into the intestine, and endocrine, producing several important hormones [81].

At point the ⑥ there is the caudal cardinal vein that runs with a second one, along each side of the spinal column, towards the common cardinal vein [13].

The pronephric tubule, at point ⑦, connects the pronephric glomeruli to the pronephric ducts.

These comparisons show an excellent agreement with the histopatological images.

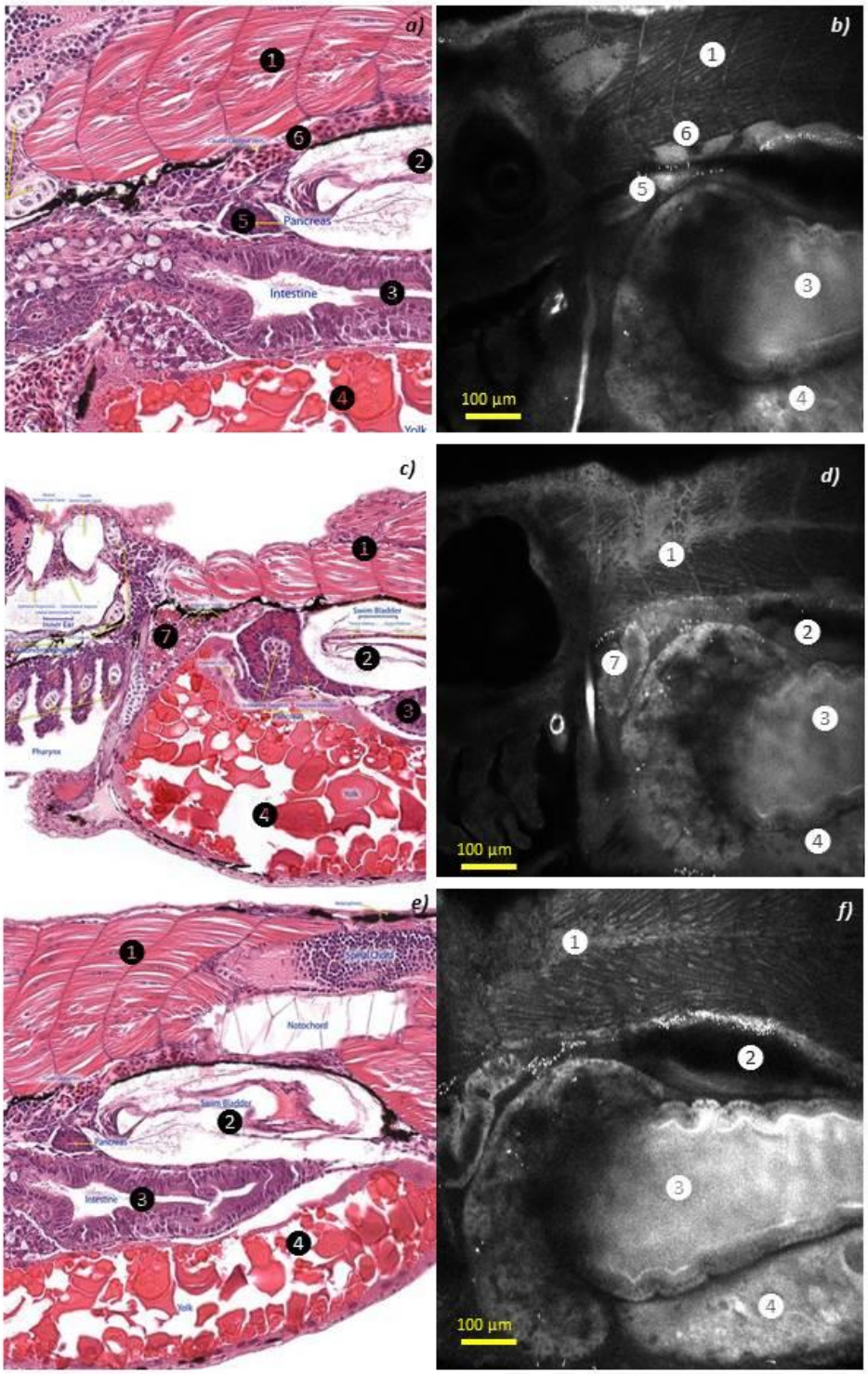


**Figure 43 Comparison of histological and TPEF images of NADH intensity of Zebrafish larva. On the left, there are the histological images, obtained from the zebrafish Atlasat 4 dpf; on the right, there are the sagittal images of NADH intensity acquired *in vivo* from a Zebrafish larva at 4dpf. ①Muscle; ②Swim Bladder; ③ Intestine; ④Yolks; ⑤Pancreas; ⑦pronephric tubule.**

The image of NADH intensity acquired by TPEF, in Figure 44b, gives the morphology of tubular structure of mitochondria in the muscle; the same portion was imaged through Second Harmonic Generation (SHG). The SHG signal in Figure 44a reveals the compact structure of these muscle cells and indicates the location of the periodic myosin thick filaments. The TPEF-SHG merge (Figure 44c) points out that there is a strong SHG signals from myofilaments, while located between the muscle fibers we can observe the bright tubular mitochondria; spinal cord, on the bottom right, does not produce any SHG signal. In fact SHG microscopy is widely used for the imaging of anisotropic molecules, which have great hyperpolarizability within tissues [82, 83] and to measure their organization. A strong SHG signal is obtained, for example, from protein structures such as collagen, microtubules and muscle myosin. This demonstrated that, with TPEF and SHG, it is possible to study the morphology using the endogenous fluorophores and from to the anisotropic molecules.

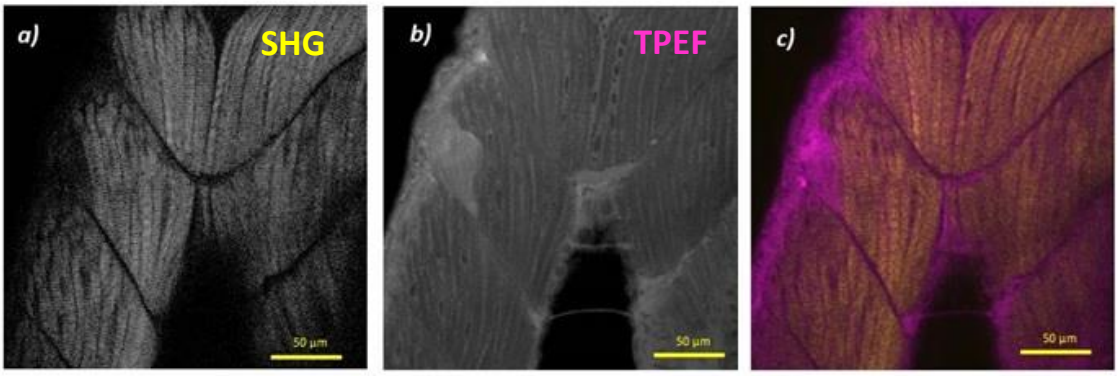


**Figure 44 TPEF and SHG images of skeletal muscle in zebrafish larva; a) image of muscle acquired by Second Harmonic Generation (SHG); b) image of muscle NADH intensity acquired by TPEF; c) merge of panels a and b; in yellow the contribution of SHG, while in magenta there is the contribution of TPEF.**

These preliminary acquisitions show that through TPEF it is possible to obtain the full anatomical mapping of the zebrafish larva *in-vivo*. TPEF microscopy can provide morphological information of the examined tissues and organs, similarly to standard histological methods but *in-vivo* and in a label-free way. The capability to discriminate various organs within TPEF images of NADH intensity allows studying the differences in metabolism among different tissues and organs.

## 3.2 Metabolic two-photon imaging of untreated zebrafish larvae

TPEF and fluorescence lifetime imaging microscopy (FLIM) are two complementary techniques that can gives a very wide framework of metabolic changings. In fact TPEF is the tool that allows obtaining information of the intensity ratio of NADH/FAD in a very rapid way. FLIM is advantageous because it is sensitive to the fluorophore microenvironment, like local pH, temperature, viscosity and oxygen concentration [1]. Through these microscopy techniques we can obtain information not only about the intensity ratios of NADH/FAD but also from the lifetime imaging of NADH and to distinguish protein-bound from free NADH [76]. As previously described, reduced NADH is an essential cofactor for oxidation–reduction (redox) reactions, such as oxidative phosphorylation and glycolysis, and FAD is an important oxidant factor in the Krebs cycle and it is involved in the electron transport chain. The biochemical estimation of NADH and FAD concentrations has been used to monitor cellular energy metabolism *in vivo* [57] and FLIM has become a valuable technique to image live cells and to analyze metabolic states of cells [84].

This method therefore permits fast intensity measurements of redox ratios to be performed without motion artifacts in developing embryos and without altering the larvae metabolism. In these measurements there could be possible artefacts that could affect the determination of the intensity based redox ratio. Analyzing some areas in thick tissues, the detected intensity redox ratio should be the same of the intensity of NADH/FAD ratio emitted, but to have this, the scattering and the absorption should be the same for both the wavelengths. Using albino zebrafish it was shown that the scattering is significantly reduced compared to biological tissue. Besides, the absorption is similar for the two wavelengths, and then the detected intensity NADH/FAD ratio it is not different from the other one emitted. To be certain that these artifacts did not affect the determination of the intensity based on redox ratio in thick tissues, we tested whether the intensity ratio changes when varying the depth acquiring images in the zebrafish tissues at different depths and it was ascertained that the intensity ratio does not change when varying the depth. So these measurements show that if the artefacts could affect the determination of the intensity based on redox ratio in thick tissues these changes are negligible.

Figure 45 shows the comparison of histological (a), TPEF images of NADH intensity (b) and an image of NADH/FAD intensity (c). The TPEF image was obtained *in vivo* from a larva at 4 dpf. The acquisition shows that TPEF microscopy can provide morphological information of the tissues and organs, similarly to standard histological methods. The oxidation-reduction ratio of the mitochondrial matrix space can be evaluated by means of the optical "redox ratio", defined here as the fluorescence intensity of NADH, divided by the fluorescence intensity of FAD. The image of the ratio intensity is displayed through a false-color lookup table (LUT) and it shows the different intensity ratios in the various tissues and organs. From this image, it can be noticed that intestine, pancreas and yolk have a higher intensity compared to muscle and the other tissues and this corresponds to higher metabolism.

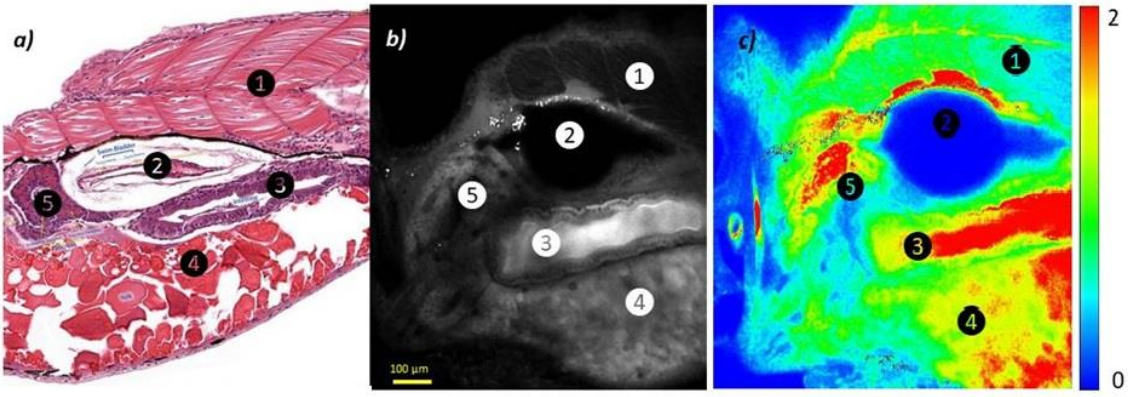


**Figure 45 a) & b) Histological image compared to TPEF image of zebrafish larva at 4dpf; ① Muscle; ②Swim Bladder; ③ Intestine; ④Yolks; ⑤Pancreas; c) NADH/FAD ratio image. The bar at the bottom shows the LUT used.**

To verify whether it is possible to differentiate the metabolism in the various organs and tissues, several images were acquired from larvae at 4, 5 and 6 dpf, in different areas of the larva. For each larva it was acquired an image from five different tissues: epithelium, intestine, muscle, liver and, spinal cord. These acquisitions show that the intensity ratios of NADH/FAD intestine (Figure 46, b) of muscle (Figure 46, c) and epithelium (Figure 47, d) have a similar trend with a slow decrease during development and this is in accord to the fact that when there is a rapid differentiation the metabolism is glycolytic and it shifts to oxidative phosphorylation during the development. In liver (Figure 46, a) and spinal cord (Figure 47, c) the intensity ratios of NADH/FAD shows a different trend, with an increase at 5 dpf that points out that the metabolism is shifted to glycolytic state while the decrease at 6 dpf suggest that the

metabolism is shifted to oxidative phosphorylation state. These trends suggest that it is possible to observe the changes in metabolism during the development of larvae, and that every tissue has its own metabolism.

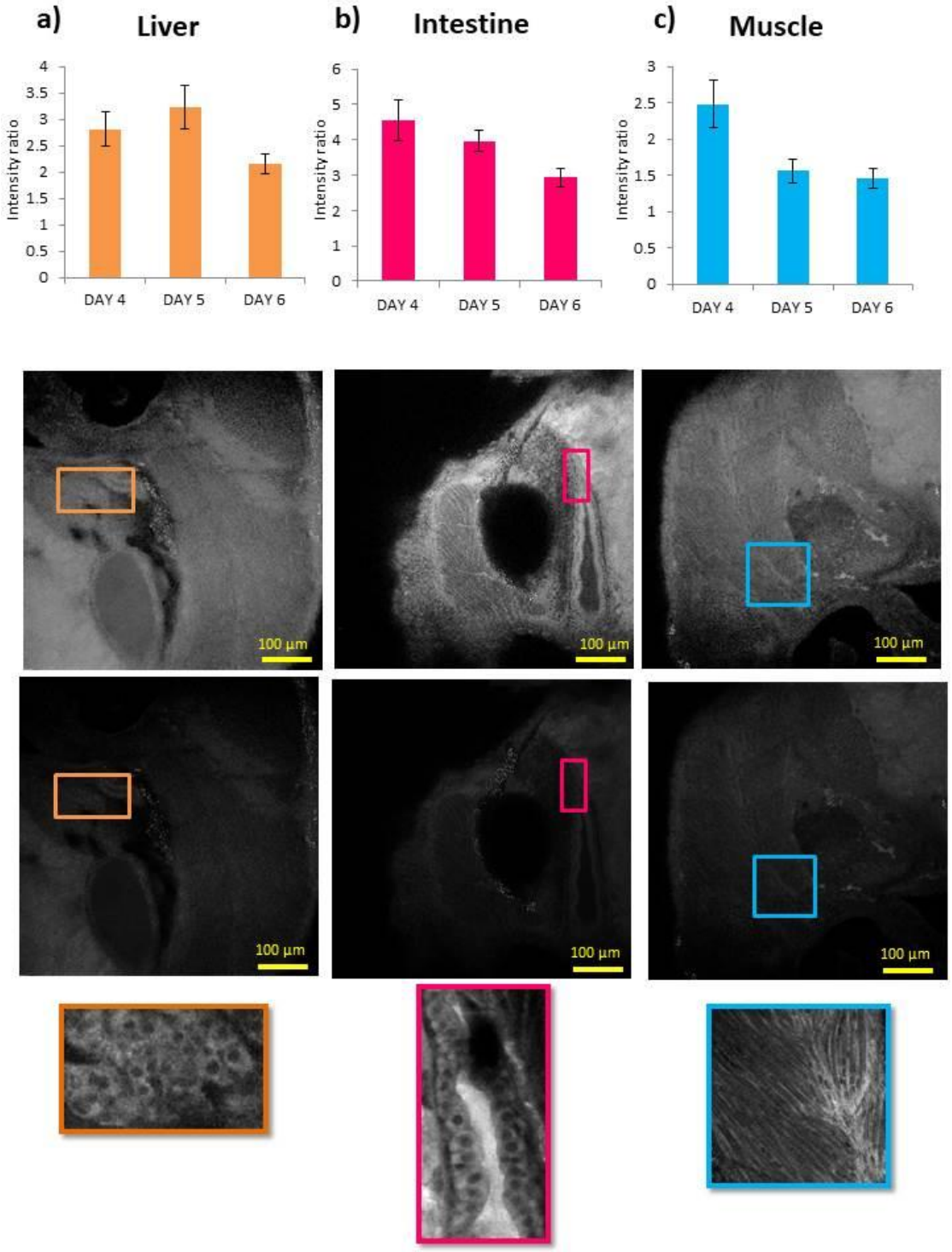


**Figure 46 Mean values of NADH/FAD intensity ratios and standard deviation (std) of larvae at 4, 5 and 6 dpf acquired from five different tissues: a) graph of intensity ratio in liver; b) graph of intensity ratio in intestine; c) graph of intensity ratio in muscle (the ratios are based on the measurement of 10 zebrafish larvae for each dpf); at the bottom of each graph there is a representative image of the acquired area (FOV 500x500µm) of the body and its ROI.**

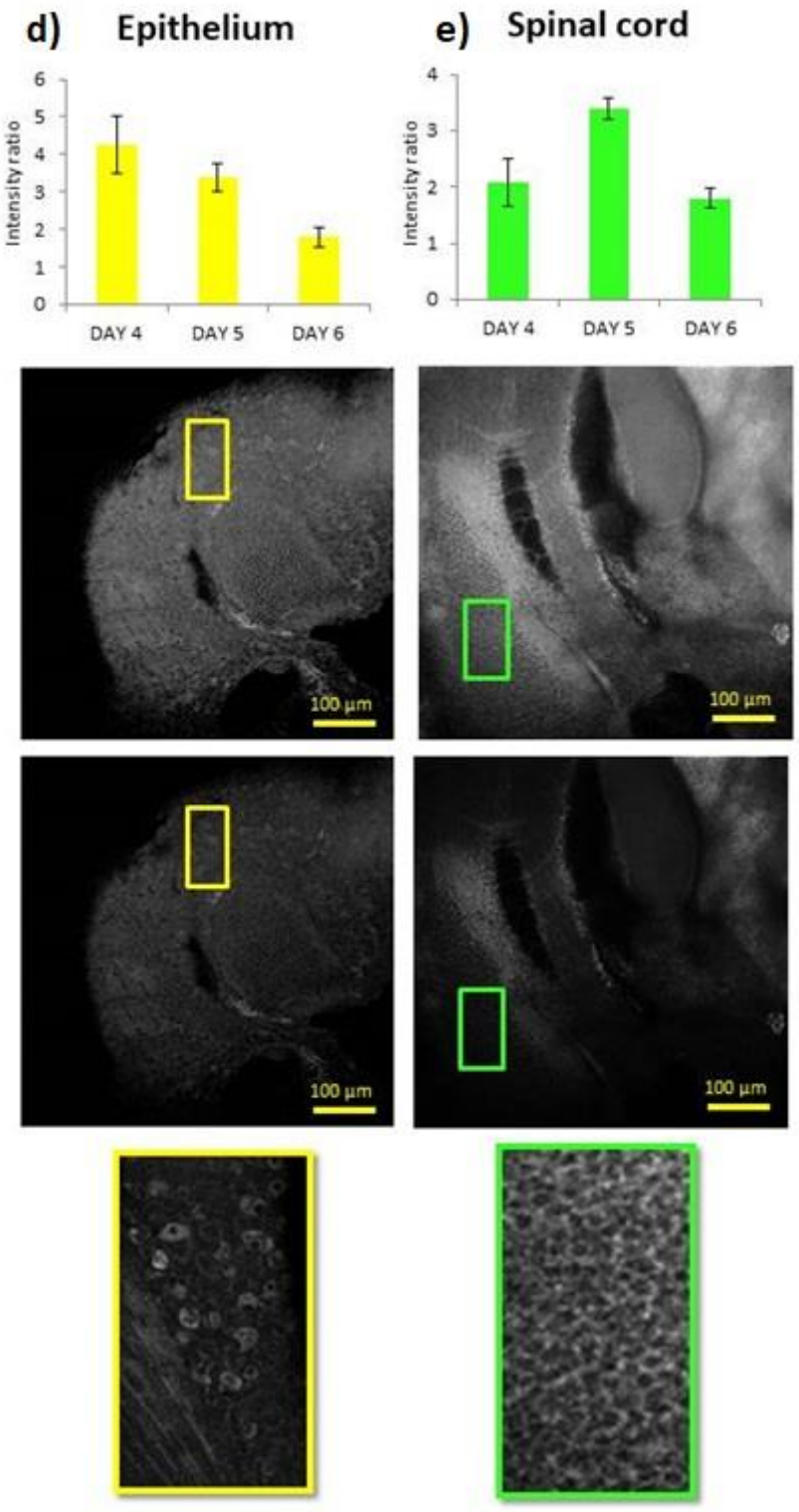


**Figure 47 Mean values of NADH/FAD intensity ratios and standard deviation (std) of larvae at 4, 5 and 6 dpf acquired from five different tissues: d) graph of intensity ratio in epithelium; e) graph of intensity ratio in spinal cord; (the ratios are based on the measurement of 10 zebrafish larvae for each dpf); at the bottom of each graph there is a representative image of the acquired area (FOV 500x500µm) of the body and its ROI.**

In Figure 48, there is a comparison of all examined organs. In the graph we can observe a decrease in epithelium, intestine, muscle from 4dpf to 5dpf and 6dpf. These results show that at 4dpf the metabolism of zebrafish larvae is shifted on glycolytic state compared to the later stages of development in the above-mentioned organs. On the other hand, the spinal cord shows a higher NADH/FAD ratio at 5 dpf. A possible explanation is that the spinal cord at 5dpf is in rapid differentiation, respect to the other two days. During the differentiation there is a change in the concentration of NADH and a large increase in glycolytic metabolism.

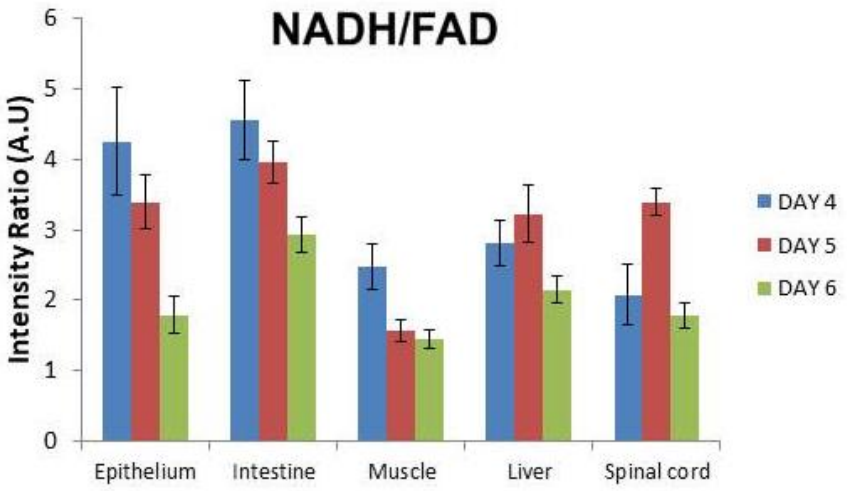


**Figure 48 Mean values of NADH/FAD intensity ratios and standard deviation (std) of larvae at 4, 5 and 6 dpf acquired from five different tissues (the ratios are based on the measurement of 10 zebrafish larvae for each day).**

These measurements show that our methods yield to follow the changes in metabolism during the development of zebrafish larvae. Moreover it is possible to observe the different metabolism that there are in each organ examined.

After these measurements of NADH/FAD ratios to analyze the metabolism in the various organs and tissues, we focused our attention on 3 tissues:

- Intestine
- Muscles
- Spinal cord

The choice of these tissues is due not only to the fact that these are easier to be identified from 2 dpf to 6 dpf, but also for their metabolic features.

The cells of the inner intestinal wall contain mitochondria that control the renewal of this organ's surface; these mitochondria, if altered, may cause the development of gut diseases, such as mitochondrial neurogastrointestinal encephalomyopathy (MNGIE)[85]. Furhermore, the stemness and homeostasis is maintained owing to the intestine mitochondrial function[86].

Muscle tissue is characterized by a very large number of mitochondria, since ATP is essential for muscle contraction.

We focused our attention also on spinal cord, as being well established that damage to spinal cord injury (SCI) and neurodegenerative diseases (Alzheimer's disease, Parkinson's disease, Huntington's disease and amyotrophic lateral sclerosis), and the central nervous system (CNS) by traumatic brain injury, are associated with mitochondrial dysfunction [87].

Moreover we selected only these tissues as the other ones may contain autofluorescent fluorophores different from NADH and FAD that can give contributions (i.e. in yolk [80], lumen and eyes where there is a large contribution by different endogenous fluorophores). The endogenous fluorophores are also contained in intestine, muscle and spinal cord but their contributions do not interfere with our studies because they are excited by different wavelength and/or the concentration of their is negligible (tryptophan).

To understand if TPEF microscopy is a promising tool that allows observing the changes in intensity ratio of NADH/FAD, we treated the larvae with 3 different methods that were known to induce observable changes of the metabolic state, as described in the following paragraphs.

## 3.3 Metabolic two-imaging imaging of zebrafish larvae treated with rotenone

Rotenone, as mentioned in paragraph 1.4.3, inhibits the complex I of electron transport chain (ETC) causing an increase of NADH concentration and an inhibition of oxidative phosphorylation (OXPHOS). At first to induce a change in metabolism in Zebrafish larvae, we tested the molecule of Rotenone. We treated 5 and 6 dpf Zebrafish larvae with 0.2 µM Rotenone. The measurement started 30 minutes after the beginning of the exposure. For each larva we acquired 3 different areas: intestine, muscle and spinal cord and we examined the same body areas in every larva.

In Figure 49 NADH, FAD, and NADH/FAD ratiometric images of larvae at 5dpf treated with rotenone are compared with control larvae: it is possible to see that the NADH intensity of intestine, muscle and spinal cord in the images of rotenone-treated is higher than in the control. The images of the intensity of ratios NADH/FAD show a shift towards higher intensity ratios in the tissues of larvae treated with rotenone, with respect to the control. These images are representative for the graph a shown Figure 51.

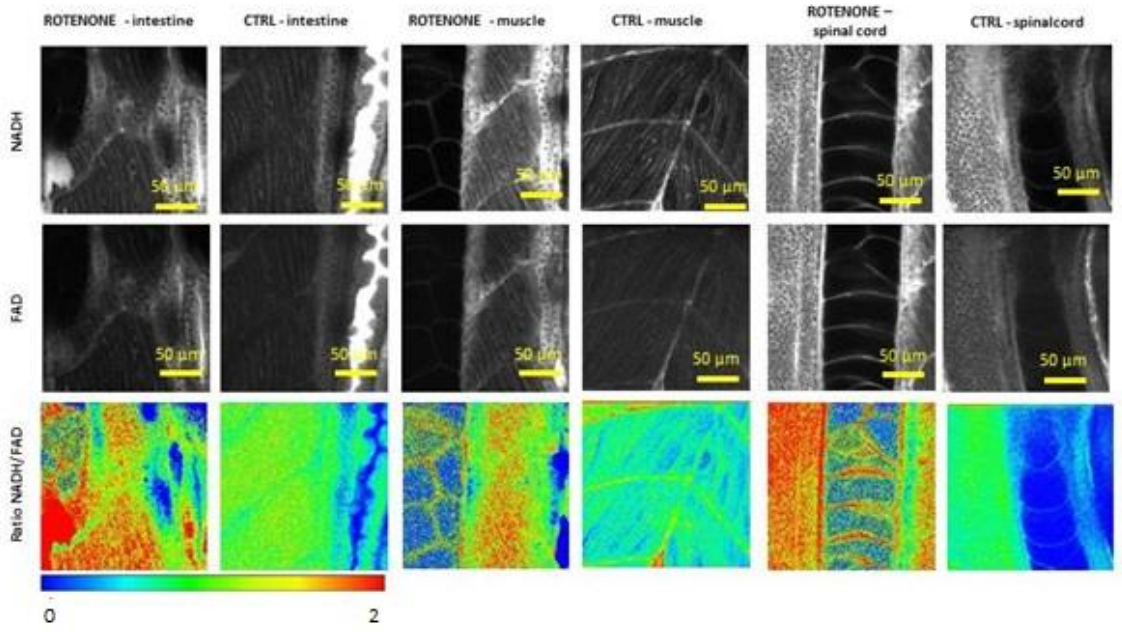


**Figure 49 images of NADH and FAD intensity, of 5 dpf larvae treated with rotenone, compared to the intensities of control larvae for each tissue. The images of intensity ratios of NADH/FAD in a false-color scale are shown with the bar displayed with the color bar. Image size 200x200 µm$^2$.**

In Figure 50 there are NADH, FAD and NADH/FAD images obtained from the intestine, muscle and spinal cord. Treated larvae show in intestine a shift in the NADH/FAD ratio towards higher values compared to control ratios. There is the same trend also in the muscle but there it is much more evident, as demonstrated by Figure 50. Like in the ratios intensity of larvae at 5 dpf, the metabolism of larvae treated with rotenone appears more shifted on glycolytic state compared to the control, as expected from the effect of Rotenone. The Figure 50 shows that the trend occurring among the 3 tissues is less evident compared to the ratios at 5dpf.

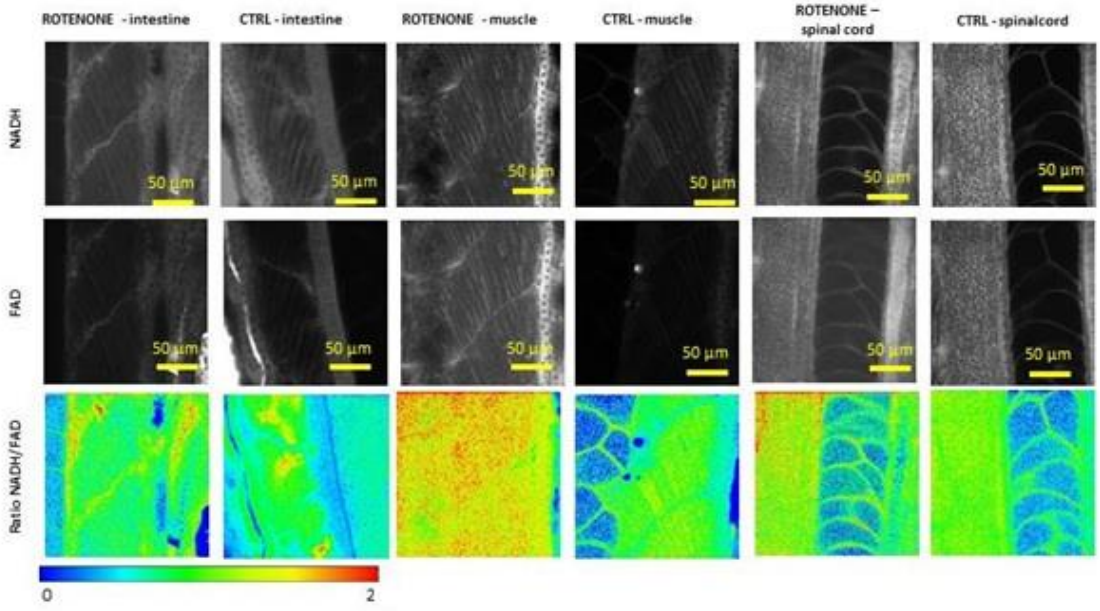


**Figure 50 images of NADH and FAD intensity, of 6 dpf larvae treated with rotenone, compared to the intensities of control larvae for each tissue. The images of intensity ratios of NADH/FAD in a false-color scale are shown with the bar displayed with the color bar. Image size 200x200 µm$^2$.**

In the graph a) in Figure 51 it is possible to observe that there is a trend both for the ratios of NADH/FAD of larvae treated with rotenone and for the control: the ratios in control conditions are lower in the intestine and they increment in the muscle and in spinal cord, where the ratios are higher. On the other hand, all NADH/FAD ratios obtained from tissues treated with rotenone, on both days, are higher than the NADH/FAD ratio of control larvae, indicating that the metabolism of larvae treated with rotenone is more glycolytic than the metabolism of control.

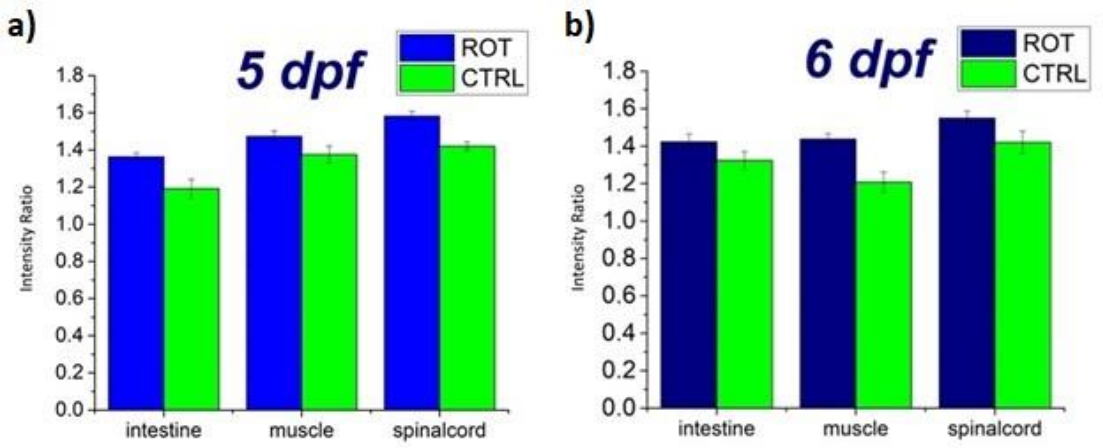


**Figure 51 Mean values of NADH/FAD intensity ratios and standard errors (SEs)of intestine, muscle and spinal cord of 5dpf (panel a) and 6dpf (panel b) larvae treated with rotenone, compared to larva control (the values are average obtained over 40 zebrafish larvae). Graph a) T-test$_{intestine}$: 3.01, ρ value $_{intestine}$>0.0025; T-test $_{muscle}$: 1.78, ρ value $_{muscle}$>0.05; T-test $_{spinalcord}$: 2.35, ρ value $_{spinalcord}$>0.025; Graph b) T-test$_{intestine}$: 1.5, ρ value $_{intestine}$>0.01; T-test $_{muscle}$: 3.7, ρ value $_{muscle}$>0.001; T-test $_{spinalcord}$: 1.7, ρ value $_{spinalcord}$>0.1**

At 6 dpf is observed the same trend seen at 5 dpf for the ratios of NADH/FAD of larvae treated, while in the control the ratios are lower in the muscle and they increment in intestine and spinal cord (Figure 51 graph b). Also in this case the metabolism of larvae treated with rotenone is more glycolytic than control larvae, as expected. These results suggest that under the treating of rotenone, the larvae failed to activate mitochondrial respiration and relied extensively on glycolysis for energy supply.

TPEF microscopy is a powerful tool, but to obtain further information about the sample we improved using Fluorescent Lifetime Imaging Microscopy (FLIM). FLIM permits to get information on free and bound NADH, and it is advantageous over fluorescence intensity because it is independent of fluorophore concentration. Through this technique it is possible to obtain sensitive measurements of the free and protein-bound NADH ratio that, as is known in literature [1], have unique properties that permit to get information about the metabolic states distinguishing whether it is shifted on glycolytic or oxidative phosphorylation state.

For each acquisition we set a field of view of 200 × 200 $\mu m^2$, and a spatial resolution of 128 × 128 pixels. Each acquisition was done setting the excitation wavelength to 740 nm. From each image acquired through FLIM, the parameter $a_1/a_2$, which refers to component ratio to get information about free-to-bound NADH, was mapped in a color-coded scale in the 0-5 range in selected ROIs and analyzed.

In the Figure 52 there are the distributions of the component ratio $a_1/a_2$. The distributions show the $a_1/a_2$ ratio of the intestine (magenta), spinal cord (blue), and muscle (green) in zebrafish larvae at 5dpf. The intestine distribution, compared to the spinal cord and muscle, is shifted to higher $a_1/a_2$ ratio, and then its metabolism is shifted more on glycolytic state than the other two tissues. This shift could be due not only to higher concentration of free NADH but could also depend on the fluorophore microenvironment, and factors such as local pH, temperature and, viscosity [1]. Compared to muscle and spinal cord, the intestine owns a microenviroment with pH different respect to the other tissues. This could be the explanation for the observed shift of intestine to higher values. On the contrary, the distributions $a_1/a_2$ ratio in spinal cord and muscle are very similar. These distributions $a_1/a_2$ demonstrate that FLIM gives more information about the microenviroment respect to TPEF intensity ratio, in fact in the graph (a) is possible to observe that the intestine is more glycolytic respect to muscle and spinal cord, and then this result can be explained with the microenvironment.

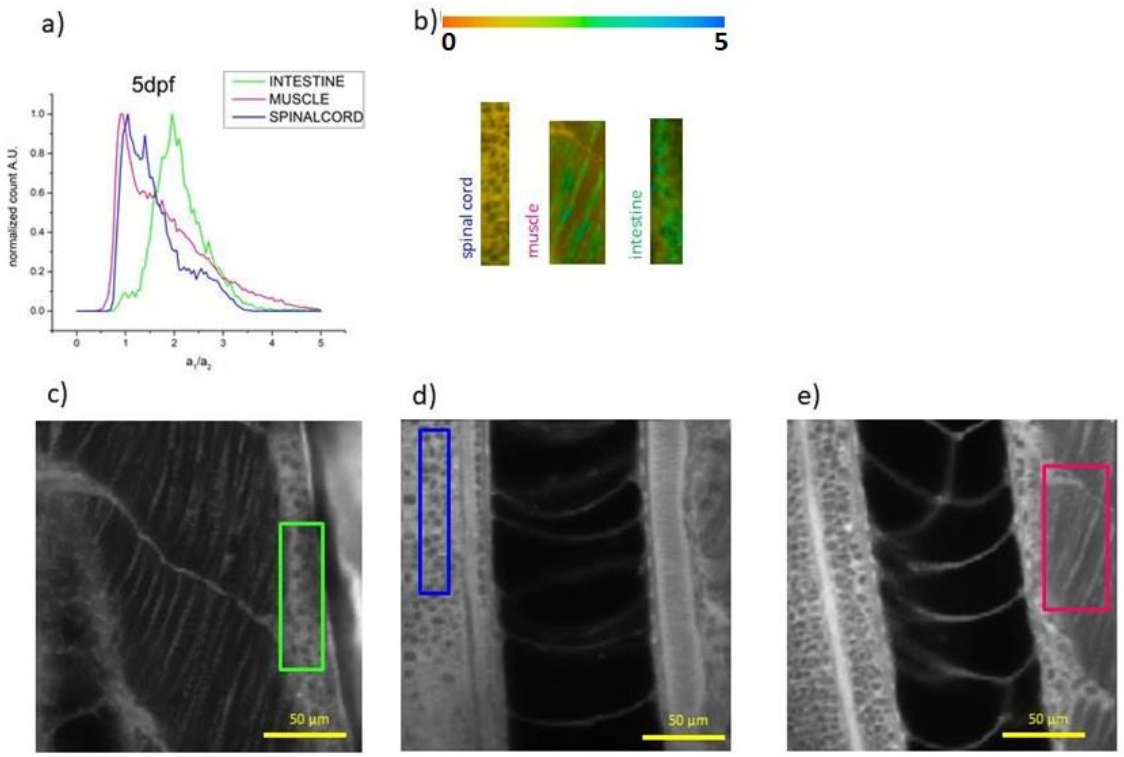


**Figure 52 a) $a_1$ / $a_2$ distribution in the intestine (magenta curve), spinal cord (blue curve) and muscle (green curve); b) ROIs; c), d) and e) NADH images show where the ROIs, displayed in the panel b), have been taken from. The measurements were performed on 25 larvae at 5dpf. Color coded: 0 <$a_1$ / $a_2$ <5.**

The graph in Figure 53 shows the $a_1/a_2$ distribution of the intestine (magenta), spinal cord (blue), and muscle (green). These distributions have been obtained from larvae at 6 dpf. The obtained trend for the three tissue is aligned to what obtained at 5dpf, but with the intestine distribution shifted to lower values, as compared to the corresponding distribution at 5dpf, indicating that the metabolism of intestine undergoes a decrease at this stage. Probably at 6 dpf the differentiation of tissues is lower than at 5 dpf.

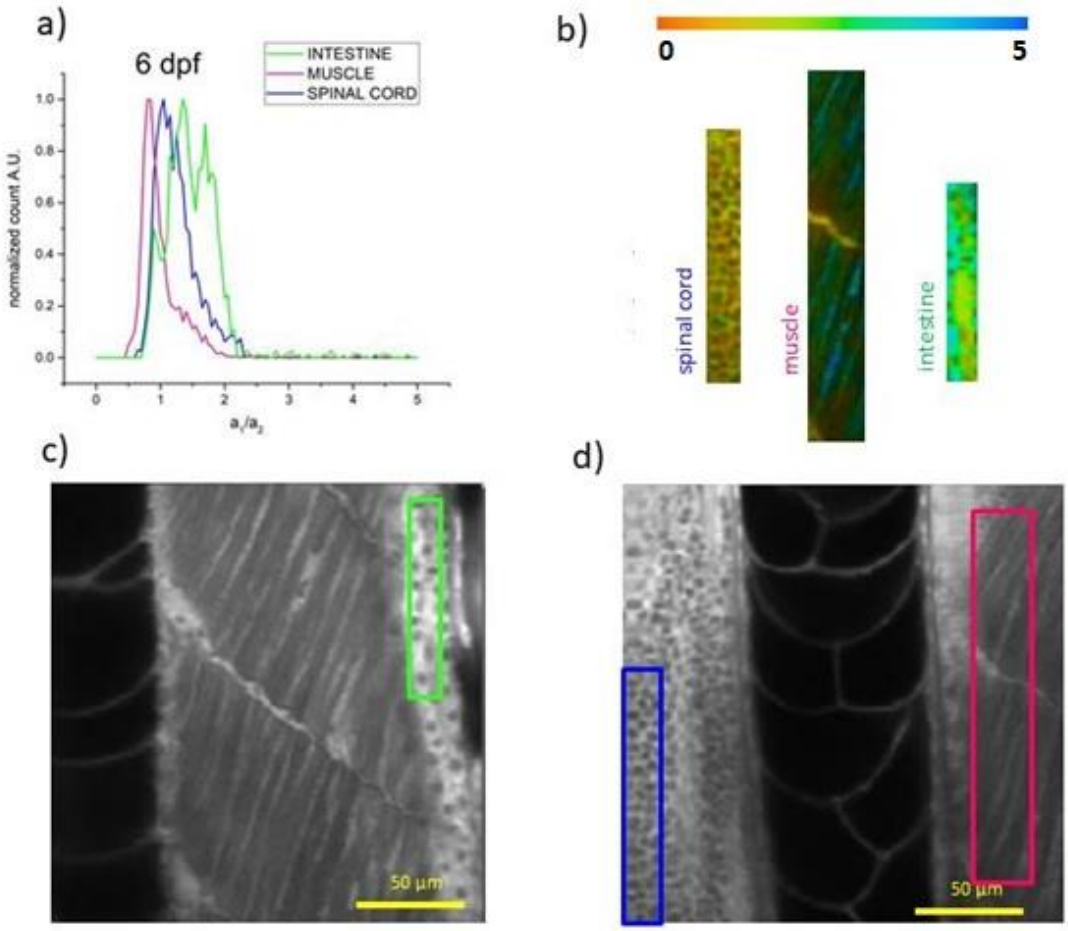


**Figure 53 a) $a_1$ / $a_2$ distribution in the intestine (magenta curve), spinal cord (blue curve) and muscle (green curve); b) ROIs; c) and d) NADH images show where the ROIs, displayed in the panel b), have been taken from. The measurements were performed on 25 larvae at 6 dpf. Color coded: 0 <$a_1$ / $a_2$ <5.**

Correlating these distributions with NADH/FAD intensities in graph 47 it is possible to observe that there is the same trend for the three tissues at 5 and 6 dpf. In fact the

intestine shows that its metabolism is more glycolytic than the other tissues while the muscle is the less glycolytic respect the other ones.

Rotenone-treated larvae were studied through FLIM to acquire the information from intestine, muscle and spinal cord. The distributions obtained are compared with the control distributions. At 5 dpf the intestine $a_1/a_2$ distribution in rotenone-treated larvae exhibits a shift to higher values respect to the control distribution. As we expected, under rotenone treatment the metabolic state of larvae shifts to glycolytic state, in fact the distribution has a peak of the values $a_1/a_2$ that shows an increasing in free-NADH.

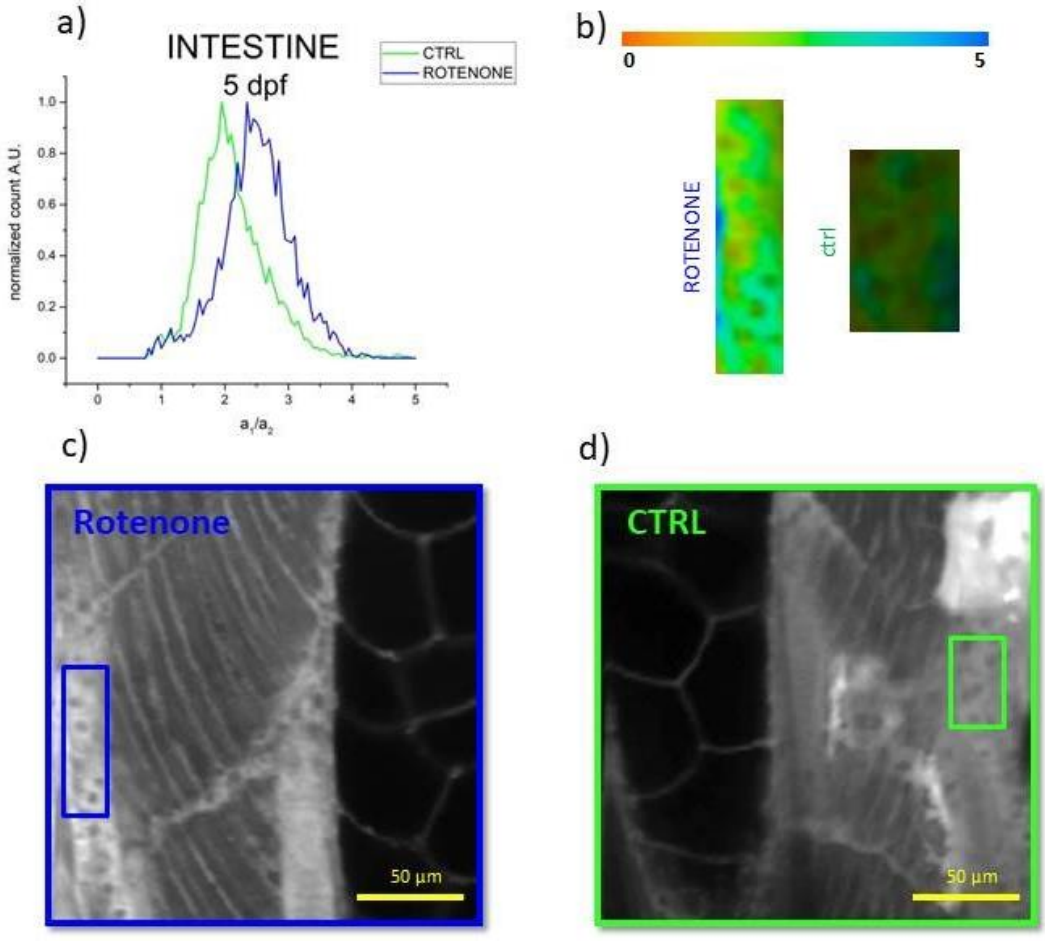


**Figure 54 a) $a_1$ / $a_2$ distribution of the intestine ROIs. The blue distribution curve is the distribution of rotenone-treated larvae, while in green the distribution curve of control larvae; b) ROIs; c) and d) NADH images show where the ROIs, displayed in the panel b) have been taken from. The measurements were performed on 25 larvae at 5 dpf. Color coded: 0 <$a_1$ / $a_2$ <5.**

The results obtained show that the flim measurements are in agreement with the intensity of NADH/FAD ratio. In fact the TPEF measurements in intestine show that the metabolism is more glycolytic in rotenone-treated larvae.

At 6 dpf the distribution of rotenone-treated larvae presents 2 peaks, the first one is at 0.8, where is also the first peak of control distribution, while the second one is shifted to higher values, so is evident the contribution of rotenone treatment in the metabolic state, in fact the inhibition of complex I favors the glycolysis over oxidative phosphorylation, increasing the free-NADH. The presence of the first peak in the distribution might be due to a contribution of bound-NADH. The bound NADH could indicate some changes in the distribution of NADH enzyme binding sites associated with preferred metabolic pathways that may be responsible for the change in protein-bound NADH lifetime with hypoxia [1].

The first peak at lower values has not influences in the fact that the metabolism is more glycolytic in rotenone-treated larvae confirming once more the results obtained from TPEF measurements where the NADH/FAD intensity ratios display a higher intensity in this kind of treatment than control intensities.

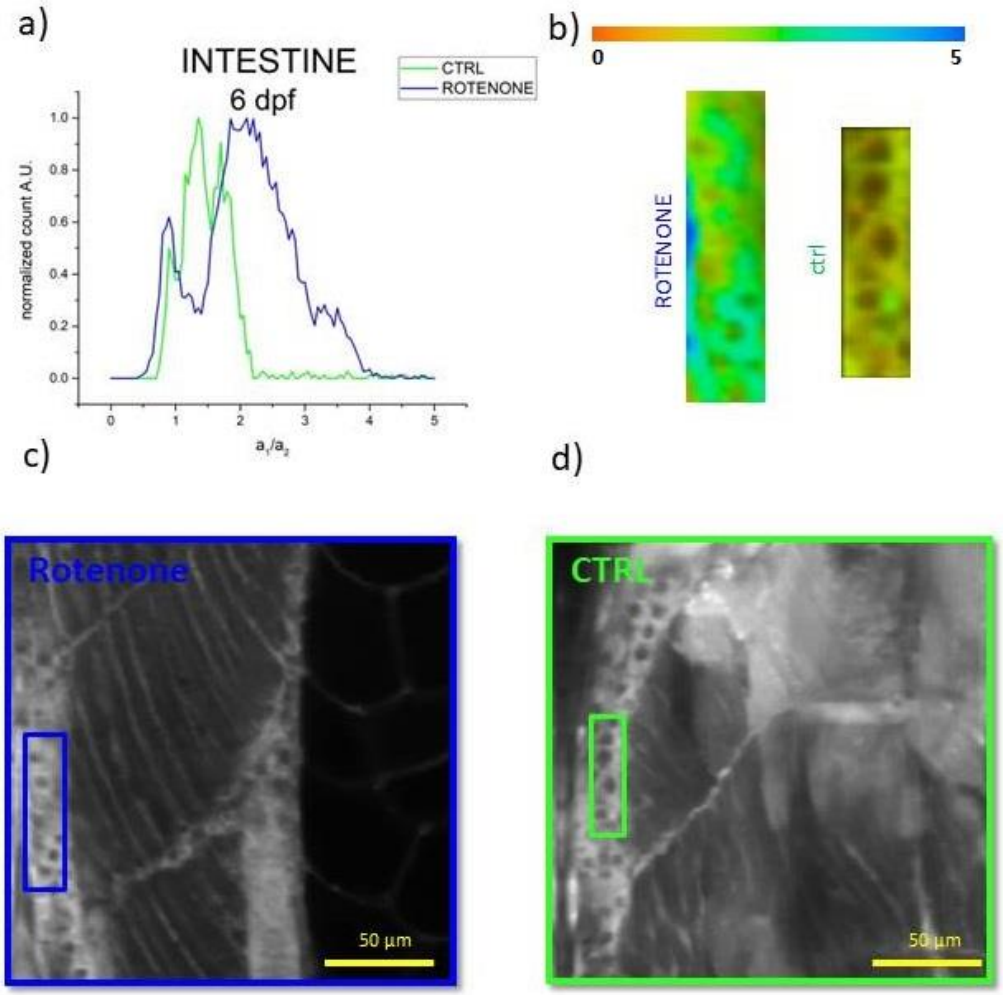


**Figure 55 $a_1$ / $a_2$ distribution of in the intestine ROIs. The blue distribution curve is the distribution of rotenone-treated larvae of $a_1$ / $a_2$ of the intestine, while in green the distribution curve of control larvae; b) ROIs; c) and d) NADH images show where the ROIs, displayed in the panel b), have been taken from. The measurements were performed on 25 larvae at 6 dpf. Color coded: 0 <$a_1$ / $a_2$ <5.**

At 5 dpf, the muscle shows a distribution centered on higher values for rotenone compared to the control distribution, demonstrating that the metabolism is more shifted on glycolysis in treated larvae. Also these results are in agreement with the NADH/FAD intensity ratio.

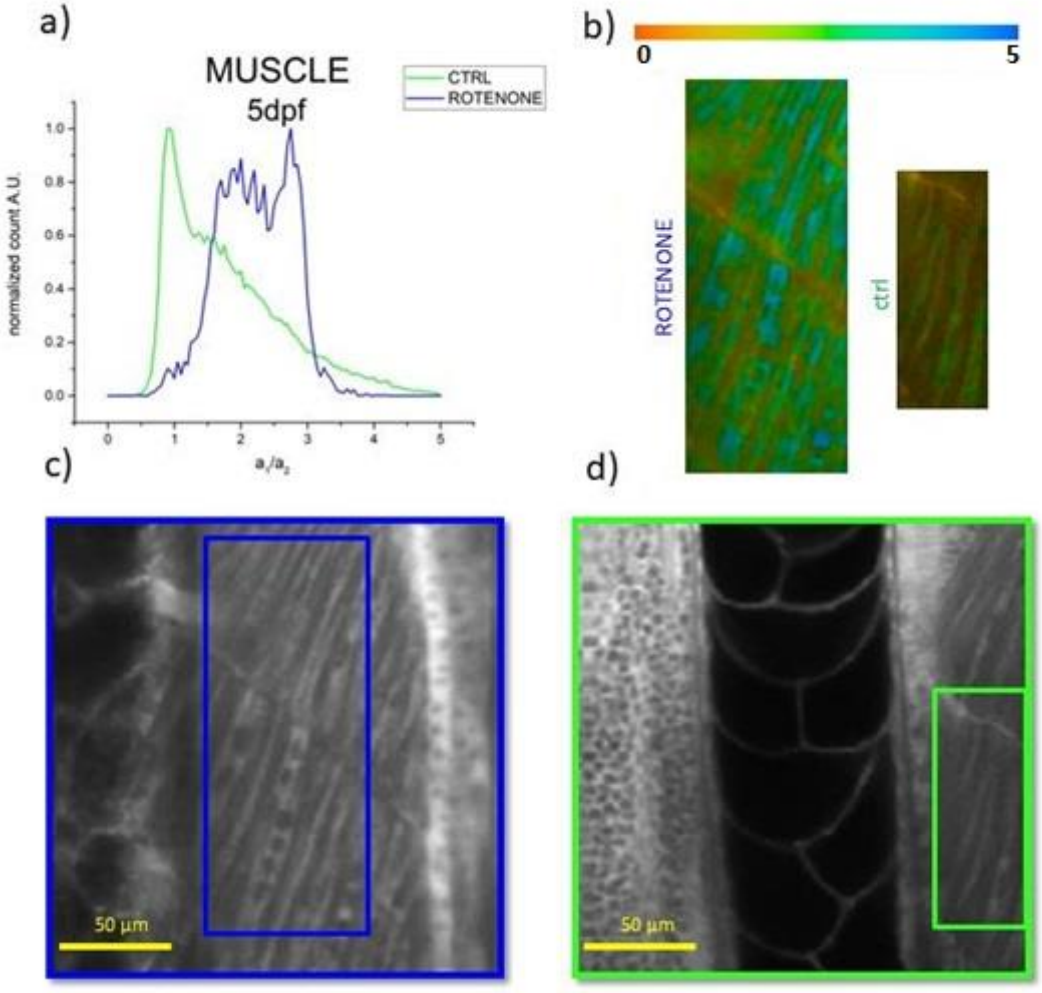


**Figure 56 $a_1$ / $a_2$ distribution of in the muscle ROIs. The blue distribution curve is the distribution of rotenone-treated larvae of $a_1$ / $a_2$ of the intestine, while in green the distribution curve of control larvae; b) ROIs; c) and d) NADH images show where the ROIs, displayed in the panel b), have been taken from. The measurements were performed on 25 larvae at 5 dpf. Color coded: 0 <$a_1$ / $a_2$ <5.**

A similar trend is also observed at 6dpf. So it is possible to confirm that in the muscle the rotenone treatment changes the metabolism toward a glycolytic state inhibiting the complex I of ETC, both at 5dpf and 6 dpf confirming the TPEF results.

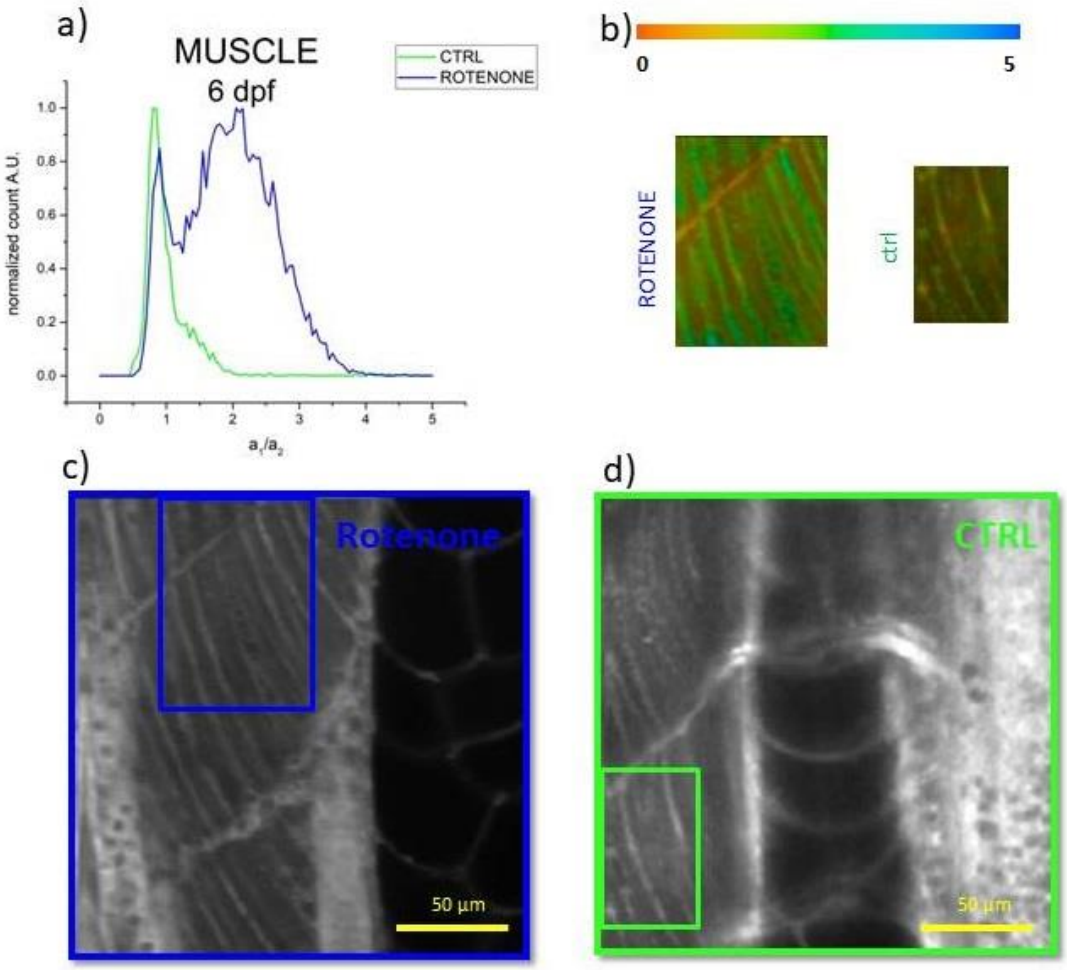


**Figure 57 $a_1$ / $a_2$ distribution of in the muscle ROIs. The blue distribution curve is the distribution of rotenone-treated larvae of $a_1$ / $a_2$ of the muscle, while in green the distribution curve of control larvae; b) ROIs; c) and d) NADH images show where the ROIs, displayed in the panel b), have been taken from. The measurements were performed on 25 larvae at 6 dpf. Color coded: 0 <$a_1$ / $a_2$ <5.**

At 5 dpf, in the spinal cord the distribution of rotenone-treated larvae is centered on similar values respect to the control. A similar behavior has been observed at 6dpf, as demonstrated in Figure 58. Probably this trend to be due the fact that in the spinal cords of zebrafish larva the rotenone has not effect like to in the other tissue, because in this tissue the metabolism is already shifted on glycolytic state respect to intestine and muscle how it is possible to observe in the Figure 51 in graph a and b.

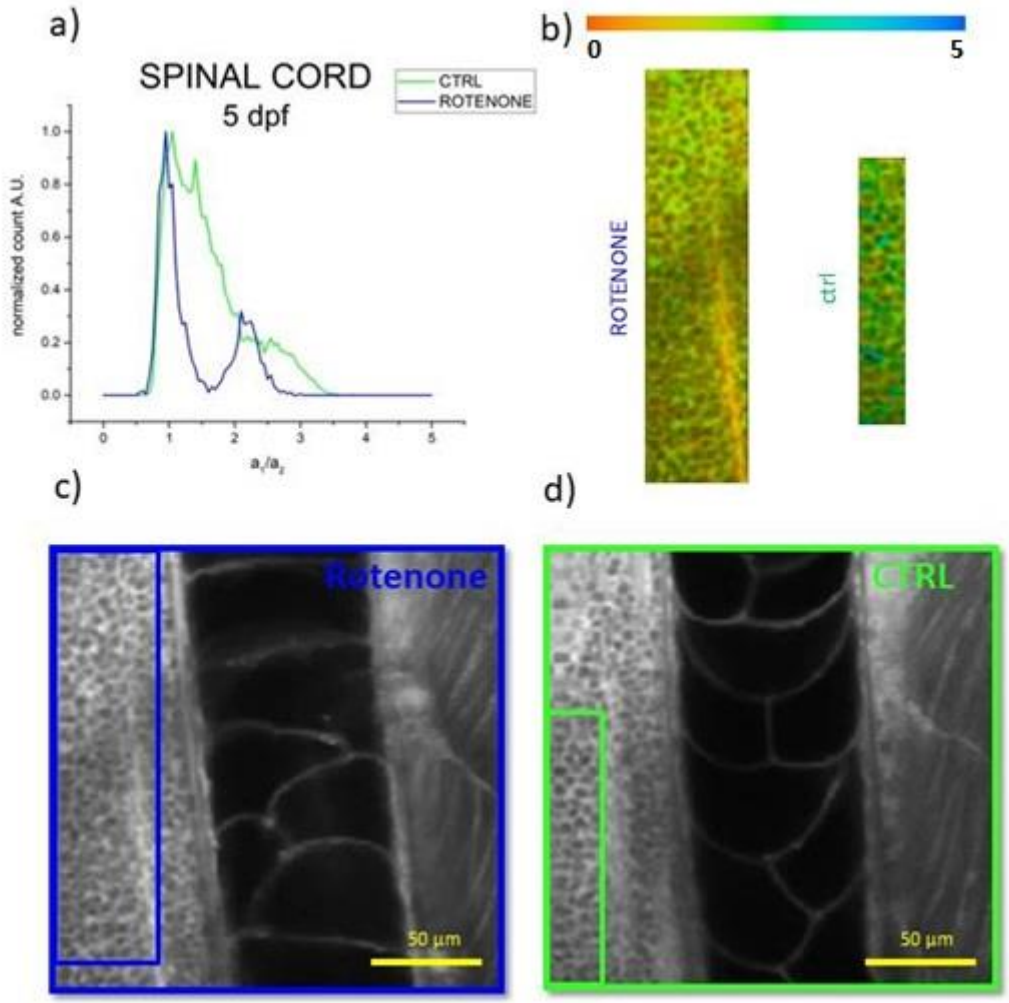


**Figure 58 $a_1$ / $a_2$ distribution of in the spinal cord ROIs. The blue distribution curve is the distribution of rotenone-treated larvae of $a_1$ / $a_2$ of the spinal cord, while in green the distribution curve of control larvae; b) ROIs; c) and d) NADH images show where the ROIs, displayed in the panel b), have been taken from. The measurements were performed on 25 larvae at 5 dpf. Color coded: 0 <$a_1$ / $a_2$ <5.**

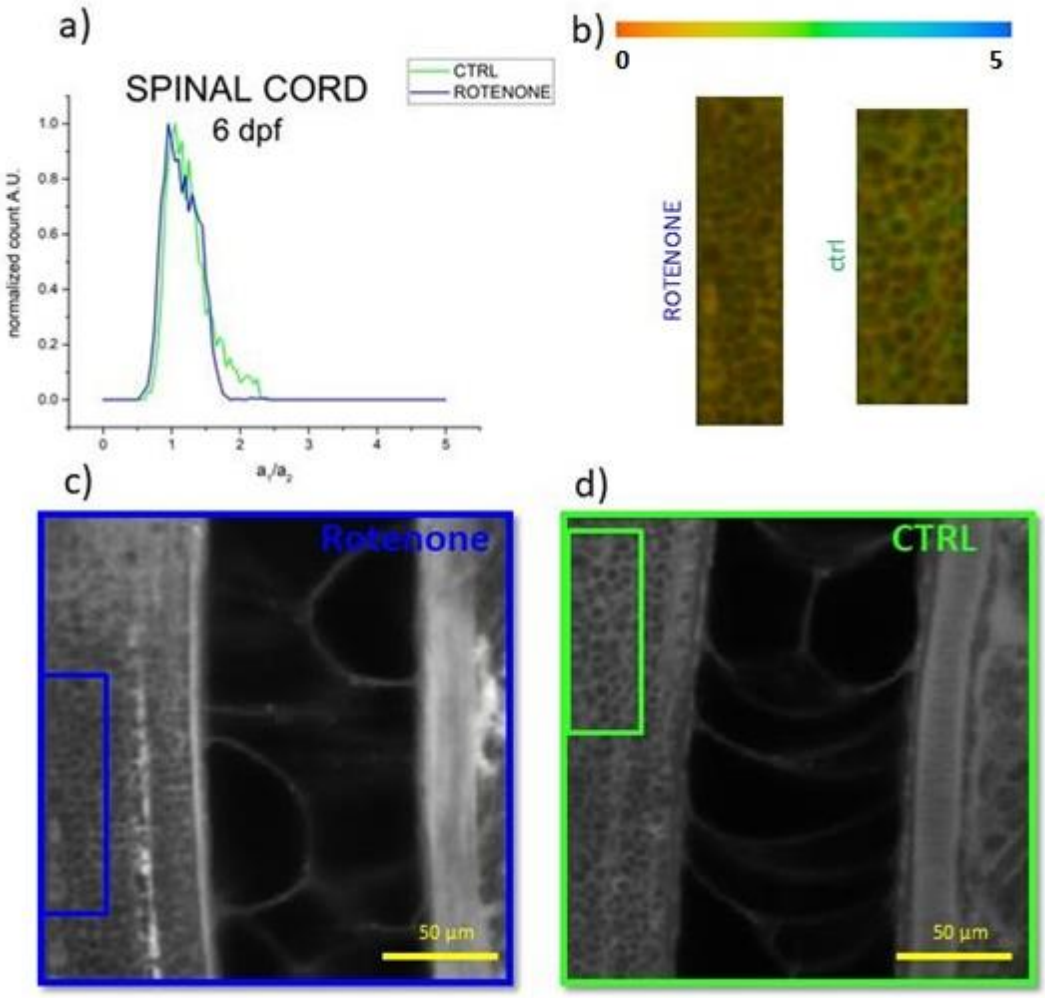


**Figure 59 $a_1$ / $a_2$ distribution of in the spinal cord ROIs. The blue distribution curve is the distribution of rotenone-treated larvae of $a_1$ / $a_2$ of the spinal cord, while in green the distribution curve of control larvae; b) ROIs; c) and d) NADH images show where the ROIs, displayed in the panel b), have been taken from. The measurements were performed on 25 larvae at 6 dpf. Color coded: 0 <$a_1$ / $a_2$ <5.**

These results revealed that the approach to simultaneous measurement of NADH and FAD through TPEF allow observing the changes in oxidative phosphorylation and glycolysis metabolic rates *in vivo* in different tissues and organs of zebrafish larvae. The measured data demonstrate that in larvae treated with rotenone a change on glycolytic metabolism compared to the control larvae at the same age can be monitored by TPEF. In fact, Rotenone, inhibiting the ETC at complex I, causes the increment of glycolytic metabolism and this inhibition induces also an increment of NADH/FAD ratio, as observed.

The FLIM measurement demonstrated that this approach is able to give information about the changings in metabolism because of its capability to investigate free or bound NADH. By correlating the results of TPEF and FLIM measurements we can get more information about the metabolism state and about the microenvironment in the analyzed tissues. As expected the two methods confirm that the rotenone treatments change the metabolism shifting it on glycolytic conditions as known from literature [41].

## 3.4 Metabolic effects of DMOG on zebrafish larvae

As explained in paragraph 1.4.1, DMOG induces HIF signaling, which, in turn, induces increased glycolysis. Therefore, the use of DMOG causes a shift to glycolytic metabolism and then an increase in NADH and a decrease in FAD. When in cellular respiration occurs a fast suppression, there is a production of NADH mitochondria were down-regulated by the de-esterified DMOG derivative, N-oxalylglycine. In the treatment with DMOG occurs a suppression of OXPHOS and the activation of glycolytic ATP flux.

In these measurements, we treated 5 and 6 dpf larvae with 100µM DMOG and we started the acquisition by TPEF 1 h and 30’ after the treatment and we acquired from the same areas studied for rotenone: intestine, muscle and spinal cord.

All the images in the bottom row of Figure 60, showing the NADH/FAD ratio, exhibit a shift to higher intensity values in treated larvae, as compared to control. The difference between treated and untreated larvae has a growing trend from intestine to spinal cord according to the graph in Figure 62.

Also comparing the images of NADH intensity of DMOG-treated larvae (Figure 60) with control, acquired at 6dpf, it can be noticed that the DMOG intensity images are more intense.

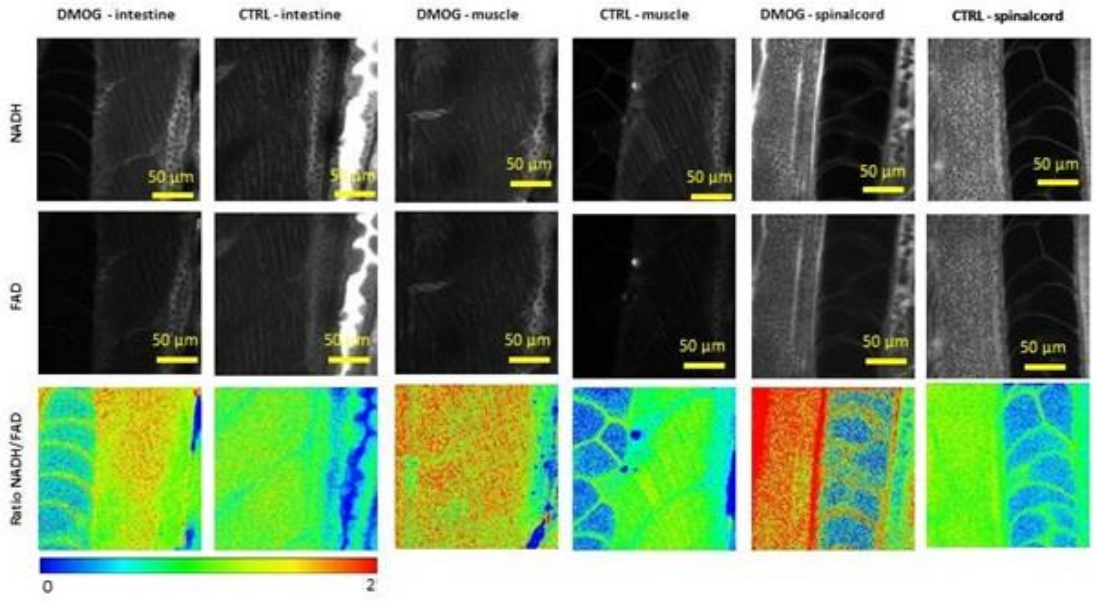


**Figure 60 images of NADH and FAD intensity, of 5 dpf in larvae treated with DMOG compared to those of control larvae for each tissue. The NADH/FAD ratios are represented in a false-color scale as shown with the bar displayed with the color bar. Image size 200x200 µm$^2$.**

In the Figure 51 it is possible to observe that there is a trend both for the ratios of NADH/FAD of DMOG-treated larvae and for the control: the ratios are lower in the intestine and increment in the muscle and in spinal cord, where the ratios are higher. On the other hand, all NADH/FAD ratios obtained from DMOG-treated tissues, on both days, are higher than the NADH/FAD ratio of control larvae, indicating that the metabolism of larvae treated with DMOG are more glycolytic than the metabolism of control. Through this analysis, we observed that the effect of DMOG is stronger than the effect of rotenone.

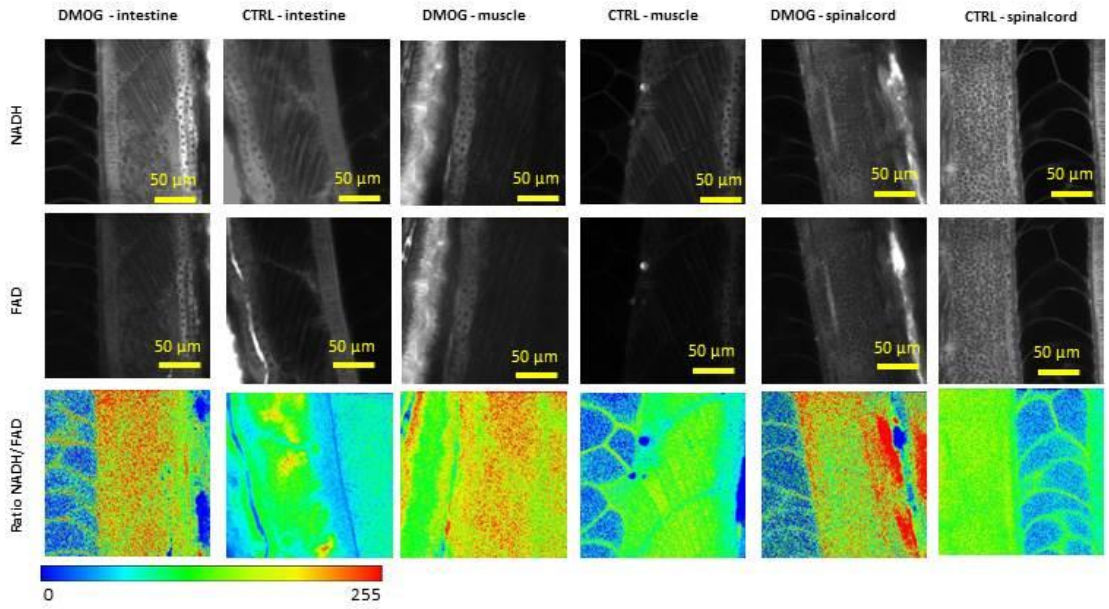


**Figure 61 images of NADH and FAD intensity of 6 dpf in larvae treated with DMOG compared to those of control larvae for each tissue. The NADH/FAD ratios are represented in a false-color scale as shown with the bar displayed with the color bar. Image size 200x200 µm$^2$.**

The intensity of NADH/FAD images (Figure 61) of the DMOG-treated larvae at 6 dpf shows higher values compared to the untreated ones. The Figure 61 shows the ratio of NADH/FAD in larvae at 6 dpf, comparing the DMOG treated to control larvae. The intensity ratio exhibits a trend similar to that observed in Figure 60, where the ratios of larvae treated are higher in spinal cord and decreasing in muscle and intestine, demonstrating that the metabolic framework of these three tissues does not display significant changes between the 5$^{th}$ and 6$^{th}$ day of development, while the effect of DMOG is in both cases can be probed by TPEF microscopy.

The graph in Figure 62 shows that the DMOG-treated larvae have an increase in metabolism; in fact their intensity ratios are higher than in the control-larvae. It can be observed that DMOG induces in each tissue a variation in metabolism, which is consistent with what expected about the effects of DMOG.

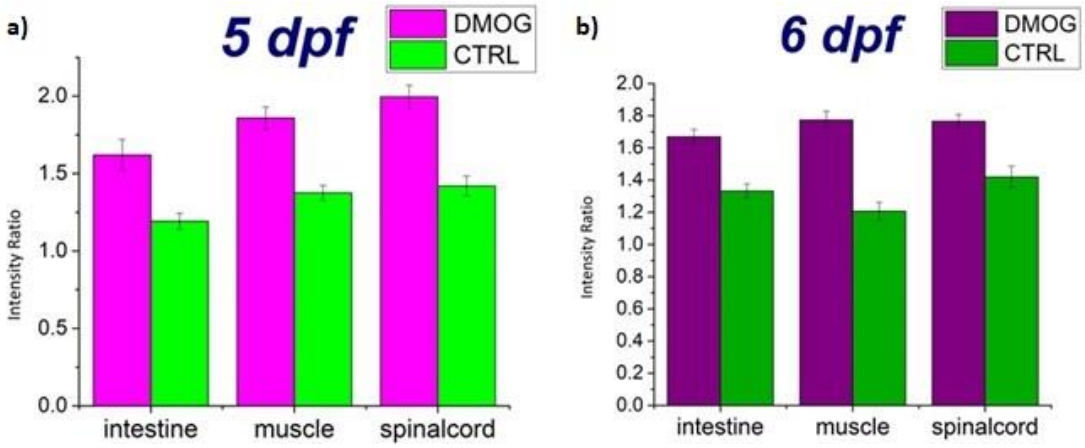


**Figure 62 Mean values of intensity ratios and standard errors (SEs); comparison between the NADH/FAD ratios of intestine, muscle and spinal cord of 5 dpf (graph a) 6 dpf (graph b) larvae treated with DMOG, compared to larva control (average over 40 zebrafish larvae)**

**Graph a) T-test$_{intestine}$: 3.7, ρ value $_{intestine}$>0.01; T-test $_{muscle}$: 5.75, ρ value $_{muscle}$>0.0005; T-test $_{spinalcord}$: 5.86, ρ value $_{spinalcord}$>0.0005; Graph b) T-test$_{intestine}$: 5.29, ρ value $_{intestine}$>0.0005; T-test $_{muscle}$: 7.37, ρ value $_{muscle}$>0.0005; T-test $_{spinalcord}$: 4.37, ρ value $_{spinalcord}$>0.0005**

Through TPEF imaging it was possible to observe the effect on metabolism of DMOG treatment. Through these analyses it has been possible to study the effect of DMOG in metabolism of the different tissues. These data have shown that the larvae treated with DMOG show a shift on glycolytic metabolism compared to the control larvae at the same stage of development. DMOG inducing the activation of HIF signaling causes an increment of NADH/FAD ratio, as DMOG increments the glycolytic metabolism and then the results obtained follow the trend that was expected from this kind of treatment, demonstrating that TPEF microscopy can give information about changes due to DMOG treatment using its capability to reflect mitochondrial function.

## 3.5 Metabolic effect of interference of MOpolG on mitochondria replication

To understand if TPEF and FLIM microscopy allowed to get information about the metabolic effect of interference of MOpolG on mithocondria replication, we microinjected the one/two-cell stage larvae fertilized eggs with MOpolG that, as described in paragraph 1.4.3.3, is a synthetic molecule that permits a transient knock-down of polymerase gamma, thus causing the inhibition of mtDNA replication. This, in turn, causes a decrease of the density of mitochondria in the tissues, leading to a lack of ATP and consequently metabolic imbalance.

For these analyses we had to start the measurements at 2 dpf because from the molecular point of view, morpholino is more efficient within 2-3 dpf, because the cell proliferation changes the concentration of morpholino by dilution effect and also occurs the degradation of the morpholino itself, in fact at 3dpf the effect of morpholino is vanishing. Figure 63 shows images of NADH and FAD intensity measured in larvae microinjected with MOpolG and control larvae. The images of NADH/FAD

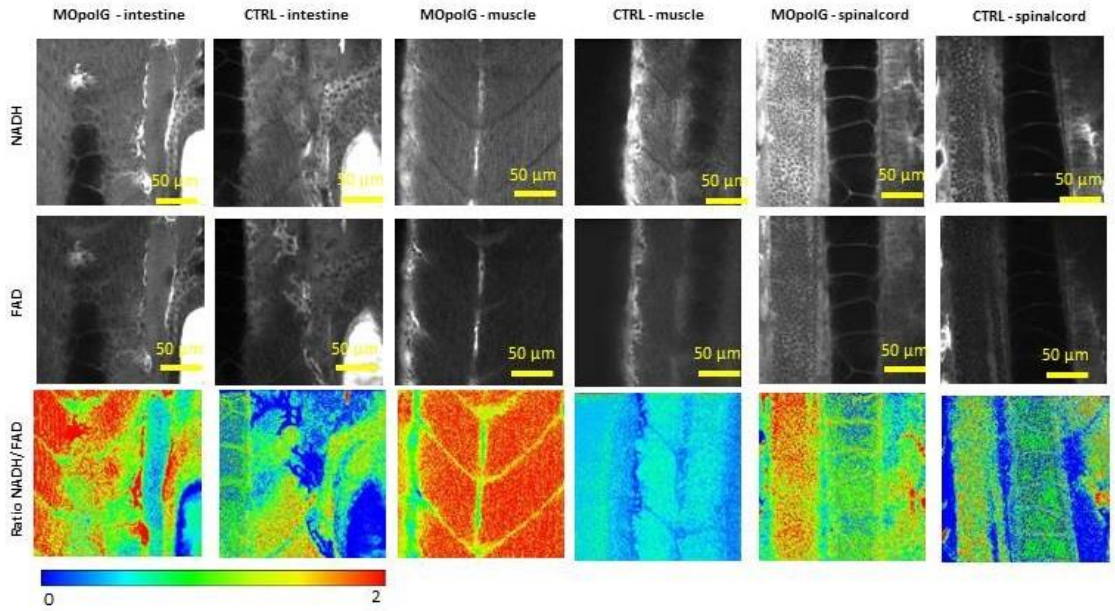


**Figure 63 images of NADH and FAD intensity, of 5dpf in larvae microinjected with MOpolG compared to those of control larvae for each tissue. The NADH/FAD ratios are represented in a false-color scale as shown with the bar displayed with the color bar. Image size 200x200 µm$^2$**

ratio show the shift to higher value of intensity in all the tissues of treated larvae, while the intensity ratios are mainly at a lower value in the control.

In the Figure 63 the images of intensity of NADH and FAD, are very similar in control and in the microinjected larvae, as it could be expected, basing on the fact that at 3dpf the effect to morpholino tends to vanish. The ratio images of microinjected larvae show intensity levels lower with respect to the intensity ratios of microinjected larvae. The decrease in the difference between microinjected and control ratios is probably due to the vanishing effect of morpholino at 3dpf. Those results confirm that the metabolism of larvae microinjected with MOpolG is more shifted on glycolytic state compared to the control and that the effect of the treatment tends to vanish at 3dpf.

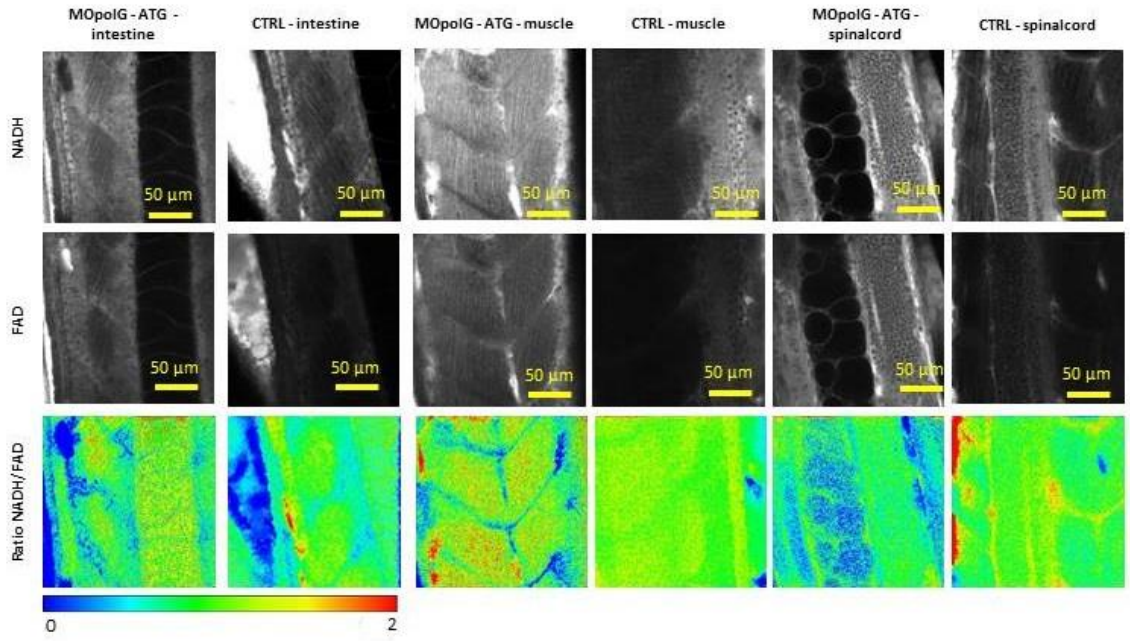


**Figure 64 images of NADH and FAD intensity, of 3dpf in larvae microinjected with MOpolG compared to those of control larvae for each tissue. The NADH/FAD ratios are represented in a false-color scale as shown with the bar displayed with the color bar. Image size 200x200 µm$^2$**

The graphs in Figure 65 show an increase of the NADH/FAD ratio (ρ value >0.005) in microinjected larvae compared to control larvae, both at 2 and 3 dpf. At 2 dpf the results show that the ratio has a higher value in muscle compared to intestine and spinal cord. This trend, repeated in graph of 3 dpf measurements (Figure 65, b), is probably due to the fact that muscle has more mitochondria with respect to the other

tissues and then it undergoes to the effects of the inhibition of mtDNA replication. The ratios at 3 dpf maintain the general trend like of the 2dpf ratios, but with a less significant difference between treated and control samples in all the tissues analyzed. This is probably due to the fact that cell proliferation decreases the concentration of morpholino microinjected and then the effect of MOpolG decreases.

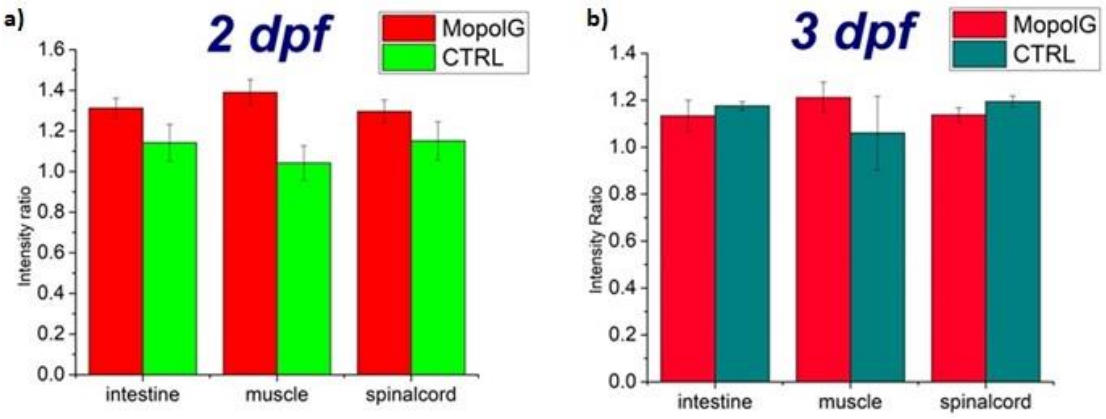


**Figure 65 Mean values of intensity ratios and standard errors (SEs); comparison between the NADH/FAD ratios of intestine, muscle and spinal cord of 2 dpf larvae microinjected with MOpolG, compared to larva control (the ratios are based on the measurement of 15 zebrafish larva for each one)**
**Graph a: T-test$_{intestine}$: 4.29, ρ value $_{intestine}$>0.0005; T-test $_{muscle}$: 6.4, ρ value $_{muscle}$>0.0005; T-test $_{spinalcord}$: 2.93, ρ value $_{spinalcord}$>0.005;**
**Graph b: T-test$_{intestine}$: 0.9, ρ value $_{intestine}$>0.25; T-test $_{muscle}$: 1.82, ρ value $_{muscle}$>0.05; T-test $_{intestine}$: 2.85, ρ value $_{spinalcord}$>0.01**

FLIM measurements have been acquired also for the larvae microinjected with MOpolG in the same conditions as previous acquisitions.

In the Figure 66, in the intestine the $a_1/a_2$ distribution of MOpolG-microinjected larvae shows that, respect to distribution control, the curve is shifted at higher value, as it was expected. We can observe the same trend at 3 dpf in the intestine (Figure 67), where the $a_1/a_2$ distribution of MOpolG-microinjected larvae centered on higher values as compared to the control.

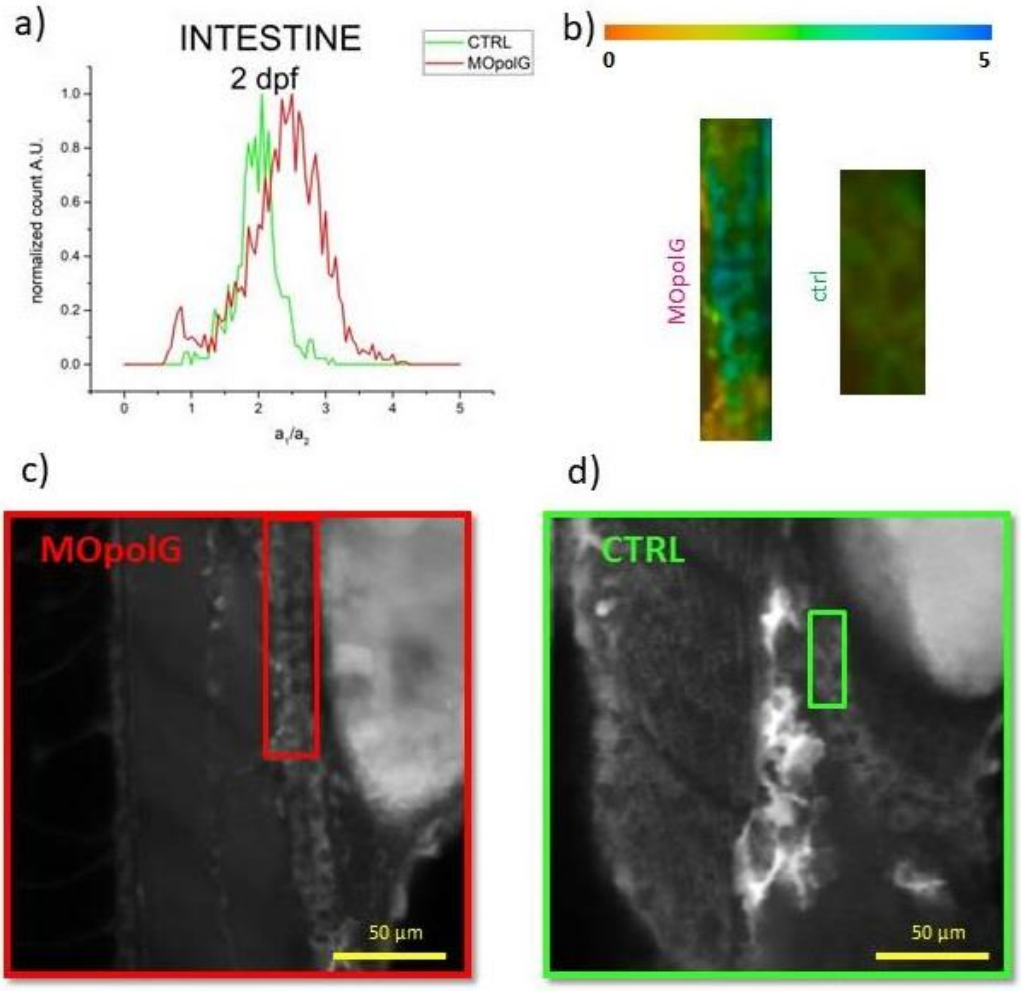


**Figure 66 shows the $a_1$ / $a_2$ distribution of in the intestine ROIs. The red distribution curve is the distribution of MOpolG-microinjected larvae of $a_1$ / $a_2$ of the intestine, while in green the distribution curve of control larvae; b) ROIs; c) and d) NADH images show where the ROIs, displayed in the panel b), have been taken from. The measurements were performed on 15 larvae at 2 dpf. Color coded: 0 <$a_1$ / $a_2$ <5;**

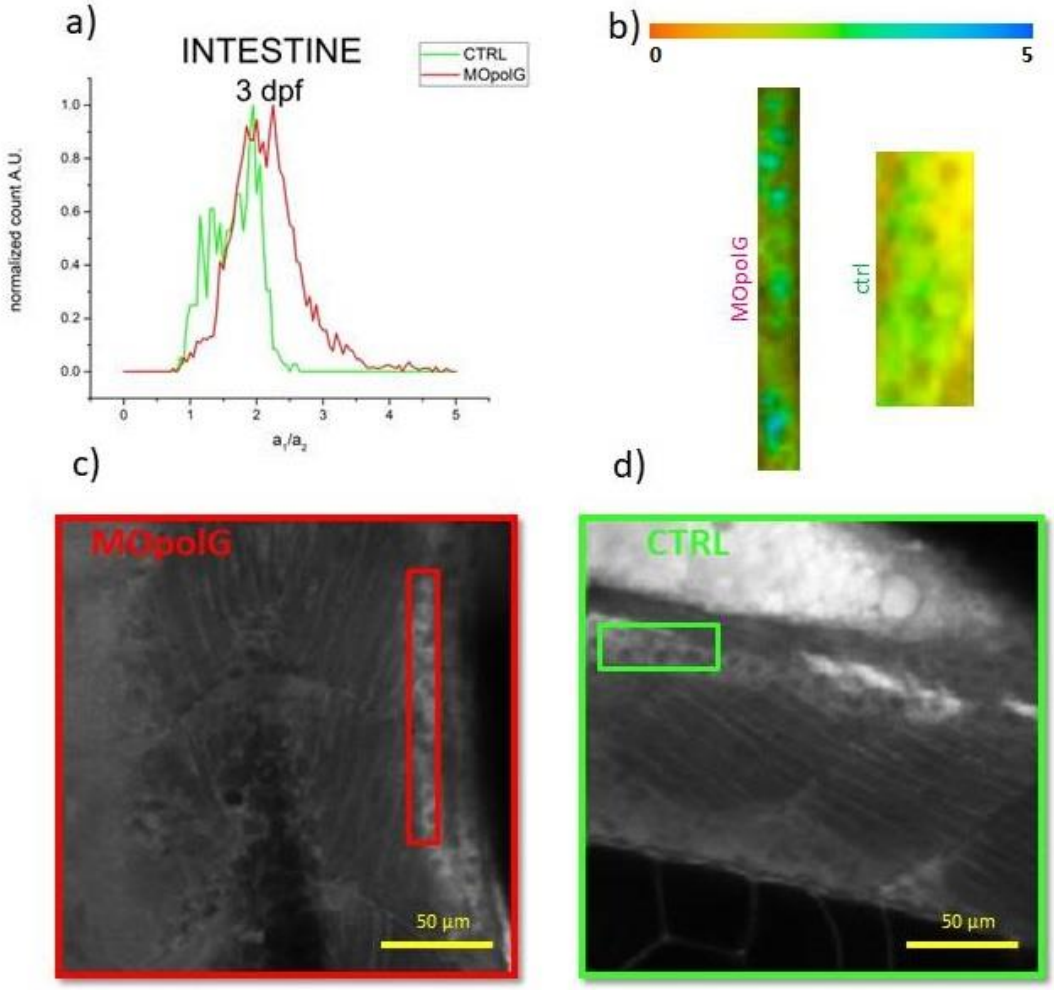


**Figure 67 shows the $a_1$ / $a_2$ distribution of in the intestine ROIs. The red distribution curve is the distribution of MOpolG-microinjected larvae of $a_1$ / $a_2$ of the intestine, while in green the distribution curve of control larvae; b) ROIs; c) and d) NADH images show where the ROIs, displayed in the panel b), have been taken from. The measurements were performed on 15 larvae at 3 dpf. Color coded: 0 <$a_1$ / $a_2$ <5;**

The graphs (Figure 68 and Figure 69) of spinal cord at 2 and 3 dpf follow the same trends of intestine distributions. These trends are in good agreement with the effect of morpholino, as the inhibition of mtDNA replication caused by MOpolG, in turn, leads to a decrease of the density of mitochondria in the tissues, and then a decrease of ATP and an increase of glycolytic state. The higher values of $a_1/a_2$ means that the metabolism is shifted to a glycolytic state and then demonstrated that FLIM acquisition can provide a good tool that allows observing the changes in metabolism.

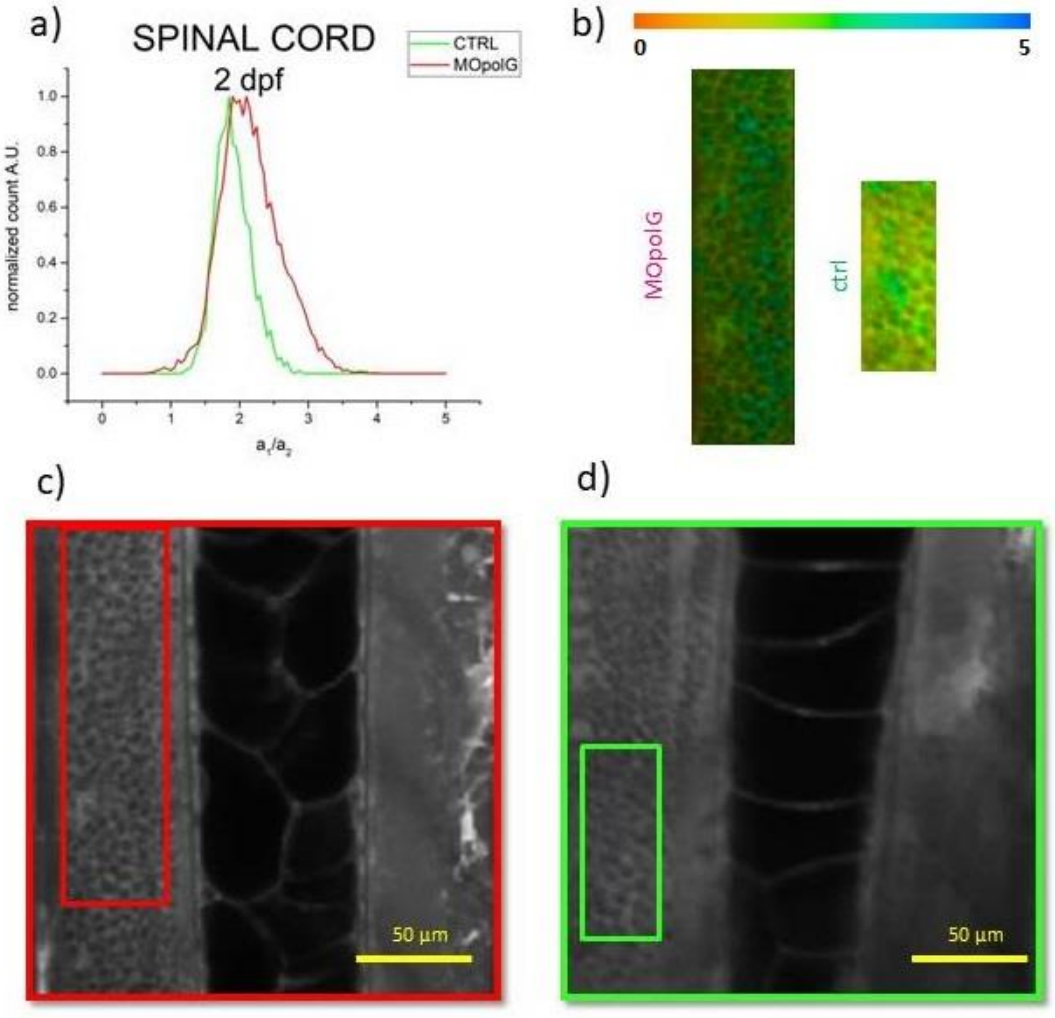


**Figure 68 $a_1$ / $a_2$ distribution of in the spinal cord ROIs. The red distribution curve is the distribution of MOpolG-microinjected larvae of $a_1$ / $a_2$ of the spinal cord, while in green the distribution curve of control larvae; b) ROIs; c) and d) NADH images show where the ROIs, displayed in the panel b), have been taken from. The measurements were performed on 15 larvae at 2 dpf. Color coded: 0 <$a_1$ / $a_2$ <5.**

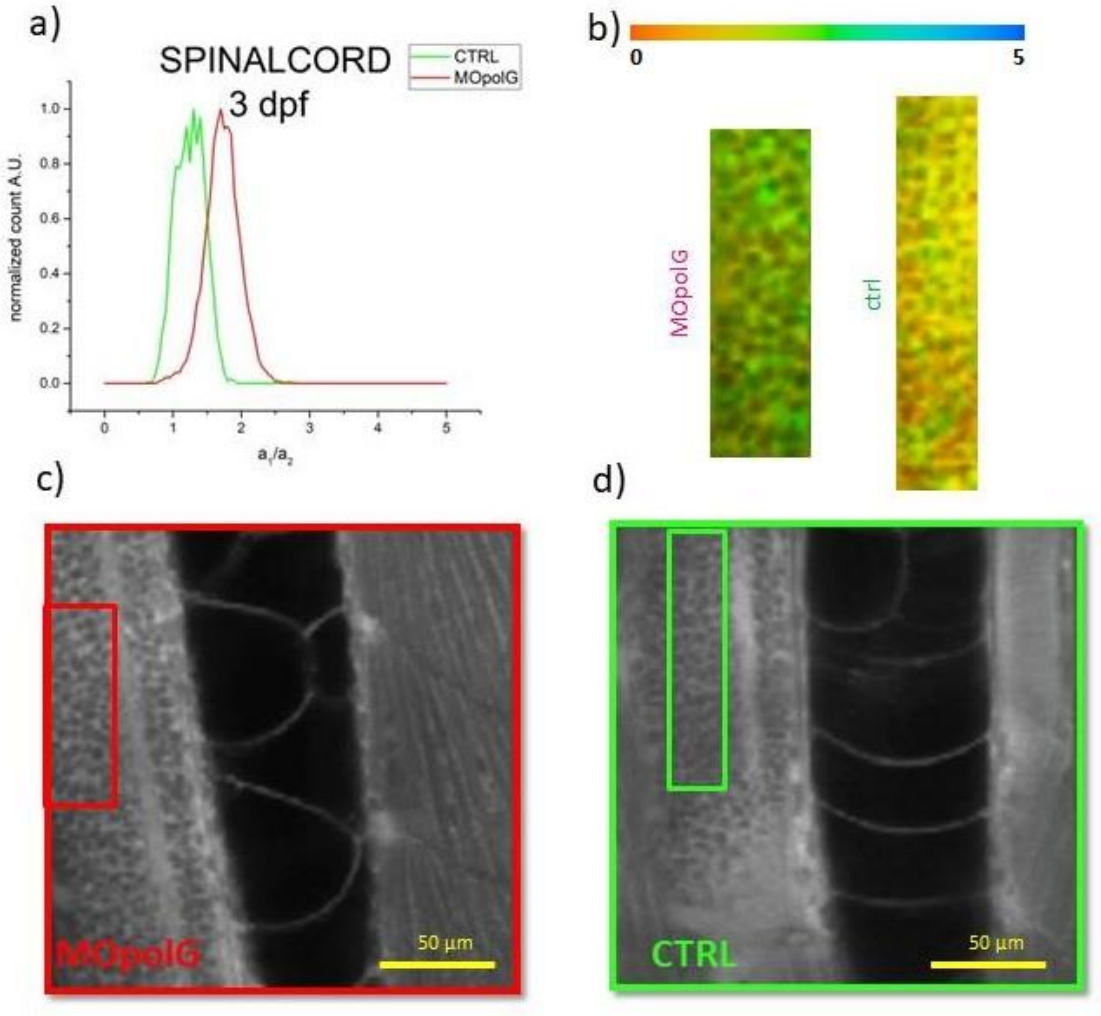


**Figure 69 $a_1$ / $a_2$ distribution of in the spinal cord ROIs. The red distribution curve is the distribution of MOpolG-microinjected larvae of $a_1$ / $a_2$ of the spinal cord, while in green the distribution curve of control larvae; b) ROIs; c) and d) NADH images show where the ROIs, displayed in the panel b), have been taken from. The measurements were performed on 15 larvae at 3 dpf. Color coded: 0 <$a_1$ / $a_2$ <5.**

## 3.6 Metabolic effect of interference of MOpolG ATG on mitochondria replication

In these measurements, we used the Morpholino ATG that, differently from Morpholino splicing, binds maternal transcripts that are mature transcripts. Furthermore to have an additional control we microinjected also a part of the eggs (those not microinjected with MOpolG) with Morpholino Mismatch which differs in five positions of base. The Morpholino Mismatch was used to check whether the phenotype found in the microinjected larvae was effectively due to the effect of morpholino or if it was caused by the microinjection or caused by other interactions with different targets. Also, for these analyses the measurements started at 2 dpf and the acquisitions were performed up to 3 dpf, because at 3dpf the effects of morpholino decrease.

In Figure 70 the NADH and FAD intensity images of the larvae microinjected with MOpolG ATG were compared to those of control larvae. The images of NADH/FAD ratio of larvae microinjected display slightly higher values than the control.

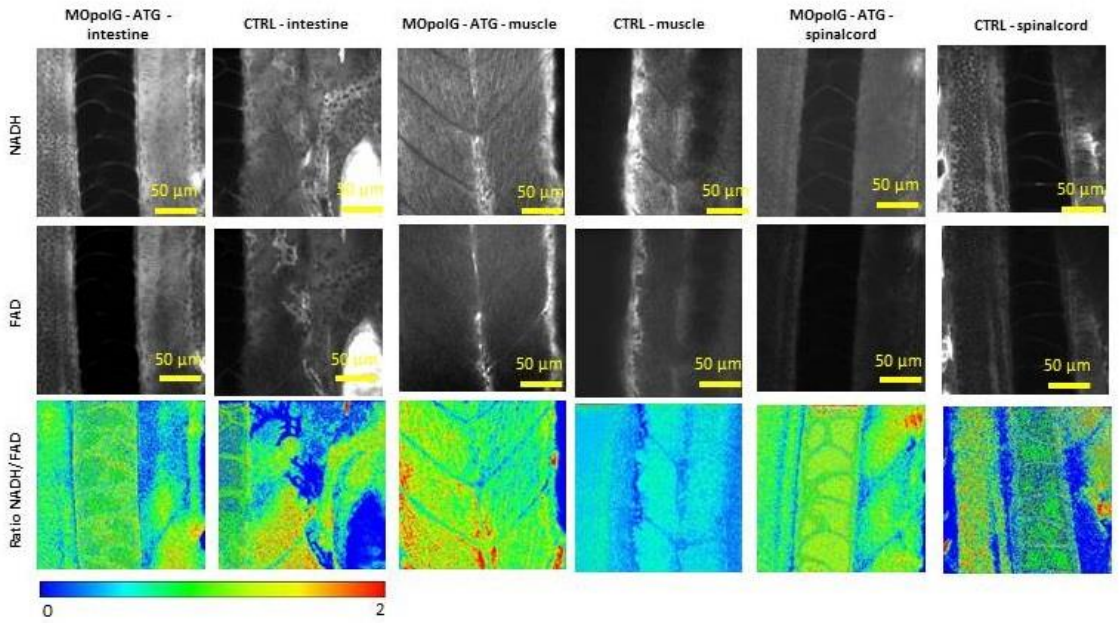


**Figure 70 images of NADH and FAD intensity, of 5dpf in larvae microinjected with MOpolG ATG compared to those of control larvae for each tissue. The NADH/FAD ratios are represented in a false-color scale as shown with the bar displayed with the color bar. Image size 200x200 µm$^2$**

In Figure 71 is possible to observe that the effect of morpholino is fading at 3 dpf, as the intensity ratios are the same for all the intensity images.

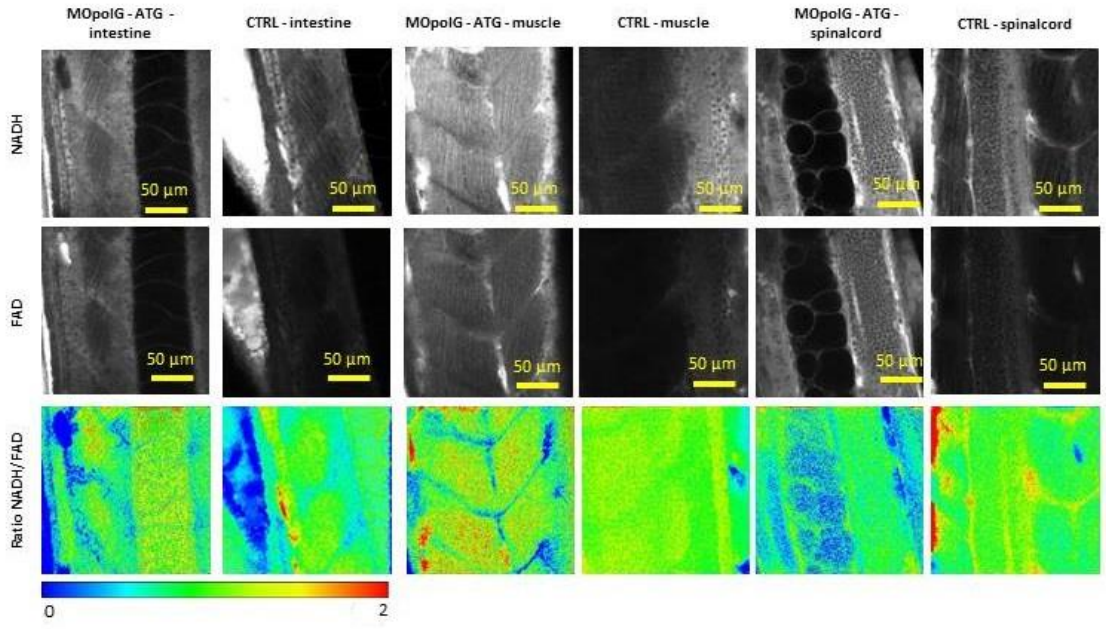


**Figure 71 images of NADH and FAD intensity, of 5dpf in larvae microinjected with MOpolG ATG compared to those of control larvae for each tissue. The NADH/FAD ratios are represented in a false-color scale as shown with the bar displayed with the color bar. Image size 200x200 µm$^2$**

The graph a) in Figure 72 shows an increased NADH/FAD ratio in muscle and spinal cord of microinjected larvae compared to control and MOmismatch microinjected larvae. The ratio of the muscle has higher values compared to the intestine and spinal cord. We found this trend not only in the graph (in Figure 72, b) of 3 dpf measurements, but also in the intensity ratios of MOpolG at 2 and 3 dpf (Figure 65). These trends are due to the fact that muscle has more mitochondria respect to the other tissues and then it undergoes to the effects of the inhibition of mtDNA replication.

In the graph b) of Figure 72 we can observe that there are less significant differences among treated, MOmismatch and control samples in all the tissues analyzed respect the intensity ratios of NADH/FAD at 2dpf. This behavior could due to the vanishing effect of MopolG ATG at 3 dpf.

These results display that through the intensity ratios is possible to observe the shift on glycolytic state of metabolism of microinjected larvae with MOpolG ATG, compared to the metabolism of control and MOmismatch larvae.

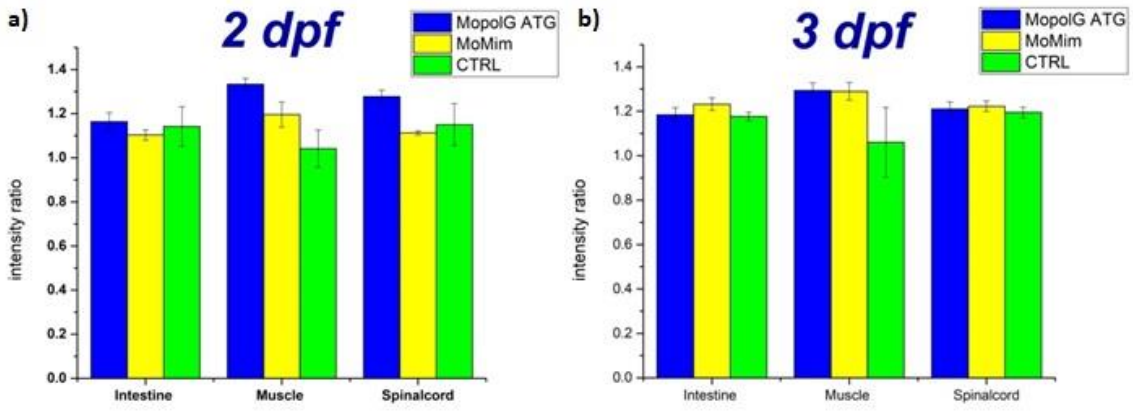


**Figure 72 Mean values of intensity ratios and errors standard (SEs); comparison between the NADH/FAD ratios of intestine, muscle and spinal cord of 3 dpf larvae microinjected with MOpolG ATG, compared to larva control (the ratios are based on the measurement of 15 zebrafish larva for each one)**
**Graph a) T-test$_{intestine}$: 1.84, ρ value $_{intestine}$>0.05; T-test $_{muscle}$: 2.19, ρ value $_{muscle}$>0.025; T-test $_{intestine}$: 0.24, ρ value $_{spinalcord}$<0.4; Graph b) T-test$_{intestine}$: 0.21, ρ value $_{intestine}$<0.4; T-test $_{muscle}$: 1.45, ρ value $_{muscle}$<0.1; T-test $_{intestine}$: 0.92, ρ value $_{spinalcord}$<0.25**

Through TPEF imaging it has been possible to study the effects of MOpolG and MOpolG ATG in metabolism of the different tissues. The TPEF data demonstrated that the larvae microinjected with MOpolG and MOpolG ATG show a shift on glycolytic metabolism compared to the control larvae at the same stage of development. The transient knock-down of polymerase gamma induce the inhibition of the replication of mtDNA and consequently it inhibits the production of more mitochondrial, causing the decrease of the density of mitochondria in the tissues, and it leads to a lack of ATP and consequent metabolic imbalance.

# 4 CONCLUSIONS

I used a custom-made Two Photon Excited Fluorescence microscope combining Fluorescence Lifetime Imaging Microscopy to characterize the metabolic state of different tissues in the zebrafish larva. The sensitivity of the method was tested using different methods that reduce the activity of oxidative phosphorylation in the cell: blocking the respiratory chain (with rotenone) or activating the HIF signaling pathway (with DMOG), that mimics the lack of oxygen, and interfering with a morpholino (MOpolG) with mitochondria replication and thus inducing a depletion of these organelles in the tissues.

Two-photon imaging allowed full anatomical mapping of the zebrafish larva and confirmed that TPEF microscopy can provide morphological information of the examined tissues and organs, similarly to standard histological methods but *in vivo* and in label-free way. Further, the capability to discriminate various organs within TPEF images of NADH and FAD intensities allowed the study of the differences in metabolism among various tissues and organs and in different experimental conditions as described above.

TPEF and FLIM demonstrated to be a promising tool for the study of mitochondrial disease using zebrafish larvae as a model. TPEF allows discrimination between glycolytic and oxidative phosphorylation state of metabolism by means to the NADH/FAD intensity ratio, while FLIM permitted to obtain information on free and bound NADH using the ratio of fast over slow lifetime components ($a_1/a_2$).

In summary, we have demonstrated that TPEF and FLIM microscopy are able to reveal the metabolic state of different tissues during the development of zebrafish larvae due to the NADH/FAD intensity ratio and to the $a_1/a_2$ distribution,. Through these tools it has also been possible to observe the changes after treatments using different methods that reduce the activity of oxidative phosphorylation and mimic the lack of oxygen.

The methods illustrated here, therefore, applied to the zebrafish model represent a powerful tool for the study of metabolism in vivo at cellular resolution with applications in the study of development and metabolic disorders.

# APPENDIX

The spectral emission of NADH and FAD in figure 37 shows that there is a crosstalk of NADH spectra on FAD, where NADH emission curve bleeds in FAD curve.

The measurements were corrected considering the NADH bleeding in FAD channel.

At the same photons incident, the detectors (PMT1, PMT2) measure the same light intensity. So calibrating and standardizing the gains the intensity is proportional to the number of fluorescence photons emitted from NADH, while in FAD channel the PMT reveals FAD and NADH fluorescence photons, as there is a percentage of NADH fluorescence photons that bleeds in this channel. Then for both the detectors (PMT1, PMT2) there is the same parameter ϒ.

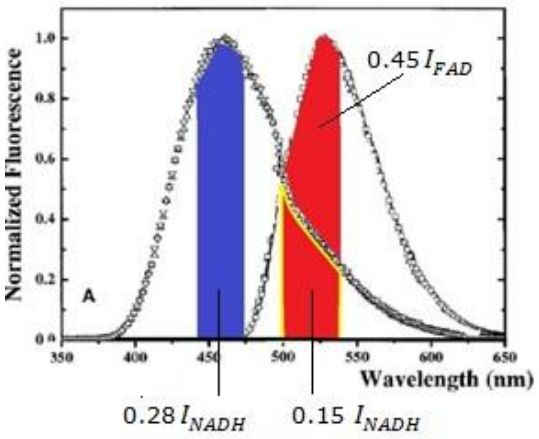


**Figure 73 spectral absorptions and emissions of NADH and FAD**

Considering that the bandpass filter 460/30 used to get information from NADH, has transmission band T>90% and reflection of 98%; while the FAD bandpass filter 520/42 has transmission band T>90% and the reflection 98%, we have for both the detector the same parameter α (α = 0.98*0.9 = 0.88).

Then:

$$\text{PMT1} = \Upsilon I_1 = \Upsilon * 0.28 * 0.88 * I_{NADH} \quad (1)$$

$$\text{PMT2} = \Upsilon I_2 = \Upsilon * 0.88 * (0.45 I_{FAD} + 0.15 \frac{n\ photons}{\alpha\ 0.28}) = \Upsilon * 0.4 * I_{FAD} + \Upsilon * 0.13 * I_{NADH} \quad (2)$$

As $I_{NADH} = \frac{PMT1}{0.25\Upsilon}$ substituting in the equation (2) $I_{NADH}$, we have that the detector PMT2 is equal to:

$$\text{PMT2} = \Upsilon * 0.4 * I_{FAD} + \Upsilon * 0.52 * \text{PMT1} \quad (3)$$

As the NADH/FAD intensity ratio is given by:

$$\frac{I_{NADH}}{I_{FAD}} = \frac{\frac{PMT1}{0.25\Upsilon}}{\frac{PMT2-0.52\,PMT1}{0.4\Upsilon}} \quad (4)$$

Then to calculate the intensity ratio from the images acquired it was used this equation

$$\frac{I_{NADH}}{I_{FAD}} = 1.6\frac{PMT1}{PMT2-0.52\,PMT1} \quad (5)$$

As the graphs show these corrections do not change the trend of intensity of DMOG, Rotenone compared to control intensity remaining unchanged while the values of intensity ratio change.

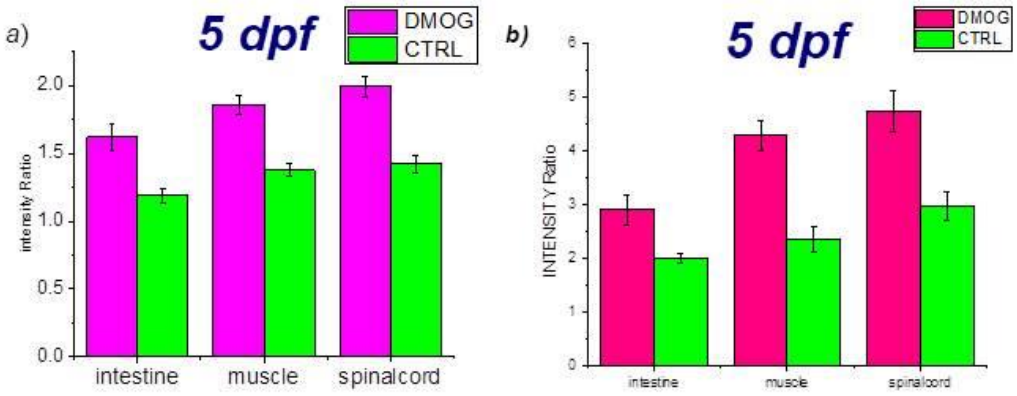


**Figure 74 Mean values of NADH/FAD intensity ratios and standard errors (SEs)of intestine, muscle and spinal cord of 5dpf (panel a) and 5dpf with correcting factor for NADH bleeding in FAD channel (panel b) for DMOG measurement**

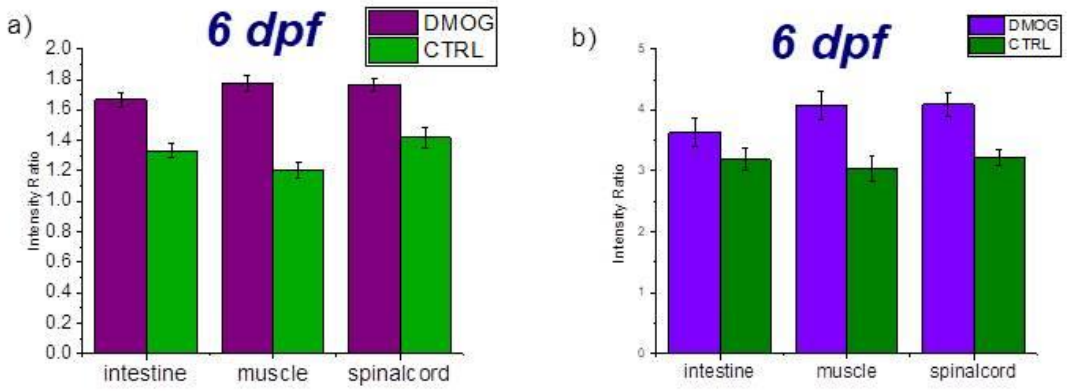


**Figure 75 Mean values of NADH/FAD intensity ratios and standard errors (SEs)of intestine, muscle and spinal cord of 6 dpf (panel a) and 6dpf with correcting factor for NADH bleeding in FAD channel (panel b) for DMOG measurement**

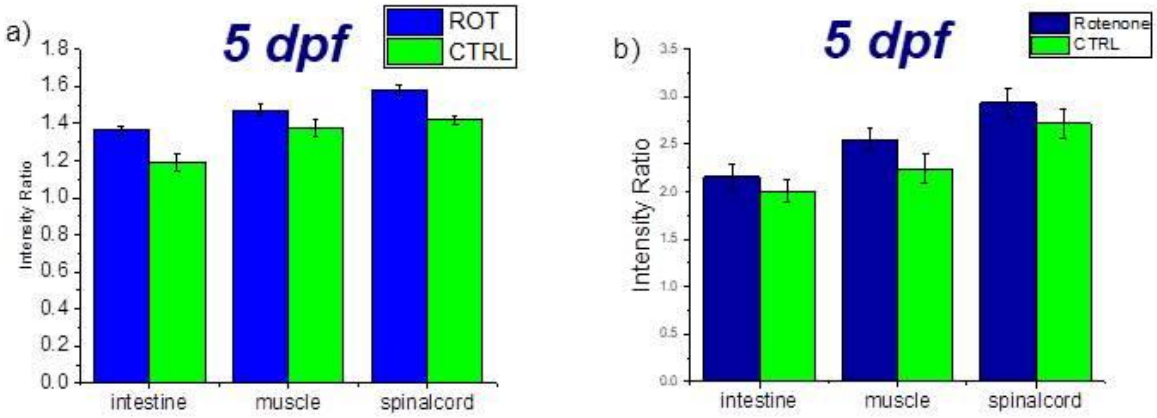


**Figure 76 Mean values of NADH/FAD intensity ratios and standard errors (SEs)of intestine, muscle and spinal cord of 5 dpf (panel a) and 5 dpf with correcting factor for NADH bleeding in FAD channel (panel b) for Rotenone measurement**

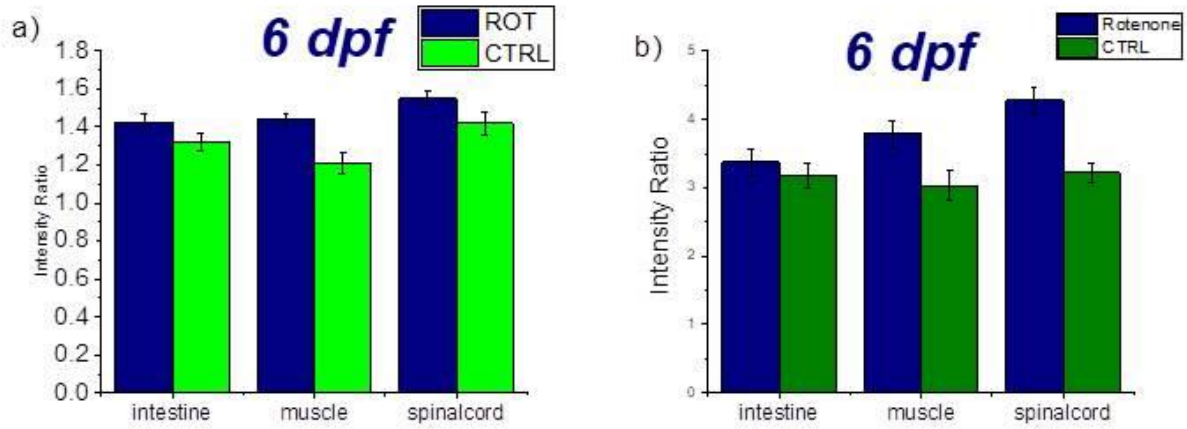


**Figure 77 Mean values of NADH/FAD intensity ratios and standard errors (SEs)of intestine, muscle and spinal cord of 6 dpf (panel a) and 6 dpf with correcting factor for NADH bleeding in FAD channel (panel b) for Rotenone measurement**

## REFERENCES


1. Skala, M.C., et al., *In vivo multiphoton fluorescence lifetime imaging of protein-bound and free nicotinamide adenine dinucleotide in normal and precancerous epithelia.* Journal of biomedical optics, 2007. **12**(2): p. 024014-024014-10.
2. Duchen, M.R., *Roles of mitochondria in health and disease.* Diabetes, 2004. **53**(suppl 1): p. S96-S102.
3. Chance, B., et al., *Oxidation-reduction ratio studies of mitochondria in freeze-trapped samples. NADH and flavoprotein fluorescence signals.* Journal of Biological Chemistry, 1979. **254**(11): p. 4764-4771.
4. W. Denk, H.J.S., and W. W. Webb, , *Two-photon laser scanning fluorescence microscopy.* Science, 1990. **73**: p. 248.
5. Zeviani, M. and S. Di Donato, *Mitochondrial disorders.* Brain, 2004. **127**(10): p. 2153-2172.
6. Sengupta, A. and P. Narad. *Glucose concentration varies logarithmically under both glycemic conditions in a computationally reconstructed human energy pool network (HEPNet)*. in *Bioinformatics and Systems Biology (BSB), International Conference on*. 2016. IEEE.
7. DiMauro, S. and E.A. Schon, *Mitochondrial disorders in the nervous system.* Annu. Rev. Neurosci., 2008. **31**: p. 91-123.
8. DiMauro, S. and E.A. Schon, *Mitochondrial respiratory-chain diseases.* New England Journal of Medicine, 2003. **348**(26): p. 2656-2668.
9. McKenzie, M., D. Liolitsa, and M.G. Hanna, *Mitochondrial disease: mutations and mechanisms.* Neurochemical research, 2004. **29**(3): p. 589-600.
10. Laale, H.W., *The biology and use of zebrafish, Brachydanio rerio in fisheries research.* Journal of Fish Biology, 1977. **10**(2): p. 121-173.
11. Dooley, K. and L.I. Zon, *Zebrafish: a model system for the study of human disease.* Current opinion in genetics & development, 2000. **10**(3): p. 252-256.
12. Briggs, J.P., *The zebrafish: a new model organism for integrative physiology.* American Journal of Physiology-Regulatory, Integrative and Comparative Physiology, 2002. **282**(1): p. R3-R9.
13. Kimmel, C.B., et al., *Stages of embryonic development of the zebrafish.* Developmental dynamics, 1995. **203**(3): p. 253-310.
14. Scholz, S., et al., *The zebrafish embryo model in environmental risk assessment—applications beyond acute toxicity testing.* Environmental Science and Pollution Research, 2008. **15**(5): p. 394-404.
15. Howe, K., et al., *The zebrafish reference genome sequence and its relationship to the human genome.* Nature, 2013. **496**(7446): p. 498.
16. Andersson, S.G., et al., *The genome sequence of Rickettsia prowazekii and the origin of mitochondria.* Nature, 1998. **396**(6707): p. 133.
17. Schultz, B.E. and S.I. Chan, *Structures and proton-pumping strategies of mitochondrial respiratory enzymes.* Annual review of biophysics and biomolecular structure, 2001. **30**(1): p. 23-65.
18. Broughton, R.E., J.E. Milam, and B.A. Roe, *The complete sequence of the zebrafish (Danio rerio) mitochondrial genome and evolutionary patterns in vertebrate mitochondrial DNA.* Genome research, 2001. **11**(11): p. 1958-1967.
19. Artuso, L., et al., *Mitochondrial DNA metabolism in early development of zebrafish (Danio rerio).* Biochimica et Biophysica Acta (BBA)-Bioenergetics, 2012. **1817**(7): p. 1002-1011.
20. Harris, A., *Hypoxia—a key regulator in angiogenesis.* Nat Rev Cancer, 2002. **2**: p. 38-47.

21. Gonzales, T.T., M. Katoh, and A. Ishimatsu, *Air breathing of aquatic burrow-dwelling eel goby, Odontamblyopus lacepedii (Gobiidae: Amblyopinae).* Journal of Experimental Biology, 2006. **209**(6): p. 1085-1092.
22. Bhattacharyya, A., et al., *Oxidative stress: an essential factor in the pathogenesis of gastrointestinal mucosal diseases.* Physiological reviews, 2014. **94**(2): p. 329-354.
23. Mansfield, K.D., et al., *Mitochondrial dysfunction resulting from loss of cytochrome c impairs cellular oxygen sensing and hypoxic HIF-α activation.* Cell metabolism, 2005. **1**(6): p. 393-399.
24. Schönenberger, M.J. and W.J. Kovacs, *Hypoxia signaling pathways: modulators of oxygen-related organelles.* Frontiers in cell and developmental biology, 2015. **3**.
25. Puissegur, M., et al., *miR-210 is overexpressed in late stages of lung cancer and mediates mitochondrial alterations associated with modulation of HIF-1 activity.* Cell death and differentiation, 2011. **18**(3): p. 465.
26. Brauner, C.J., et al., *Air breathing in the armoured catfish (Hoplosternum littorale) as an adaptation to hypoxic, acidic, and hydrogen sulphide rich waters.* Canadian Journal of Zoology, 1995. **73**(4): p. 739-744.
27. Richards, J.G., *Metabolic and molecular responses of fish to hypoxia.* Fish physiology, 2009. **27**: p. 443-485.
28. Semenza, G.L., *HIF-1 mediates the Warburg effect in clear cell renal carcinoma.* Journal of bioenergetics and biomembranes, 2007. **39**(3): p. 231-234.
29. Déry, M.-A.C., M.D. Michaud, and D.E. Richard, *Hypoxia-inducible factor 1: regulation by hypoxic and non-hypoxic activators.* The international journal of biochemistry & cell biology, 2005. **37**(3): p. 535-540.
30. Jaakkola, P., et al., *Targeting of HIF-α to the von Hippel-Lindau ubiquitylation complex by O2-regulated prolyl hydroxylation.* Science, 2001. **292**(5516): p. 468-472.
31. Ivan, M., et al., *HIFα targeted for VHL-mediated destruction by proline hydroxylation: implications for O2 sensing.* Science, 2001. **292**(5516): p. 464-468.
32. Masson, N., et al., *Independent function of two destruction domains in hypoxia-inducible factor-α chains activated by prolyl hydroxylation.* The EMBO journal, 2001. **20**(18): p. 5197-5206.
33. Epstein, A.C., et al., *C. elegans EGL-9 and mammalian homologs define a family of dioxygenases that regulate HIF by prolyl hydroxylation.* Cell, 2001. **107**(1): p. 43-54.
34. Bruick, R.K. and S.L. McKnight, *A conserved family of prolyl-4-hydroxylases that modify HIF.* Science, 2001. **294**(5545): p. 1337-1340.
35. Huang, L.E., et al., *Activation of hypoxia-inducible transcription factor depends primarily upon redox-sensitive stabilization of its α subunit.* Journal of Biological Chemistry, 1996. **271**(50): p. 32253-32259.
36. Semenza, G.L., *Targeting HIF-1 for cancer therapy.* Nature reviews. Cancer, 2003. **3**(10): p. 721.
37. Morikawa, T. and K. Takubo, *Hypoxia regulates the hematopoietic stem cell niche.* Pflügers Archiv-European Journal of Physiology, 2016. **468**(1): p. 13-22.
38. Meacham, C.E. and S.J. Morrison, *Tumour heterogeneity and cancer cell plasticity.* Nature, 2013. **501**(7467): p. 328-337.
39. Reya, T., et al., *Stem cells, cancer, and cancer stem cells.* nature, 2001. **414**(6859): p. 105-111.
40. P. Stoller, K.M.R., P. M. Celliers and A. M. Rubenchik, *Polarization-modulated second harmonic generation in collagen.* Biophys. J., 2002. **3330**: p. 82.
41. sigmaaldrich.com.
42. Sherer, T.B., et al., *An in vitro model of Parkinson's disease: linking mitochondrial impairment to altered α-synuclein metabolism and oxidative damage.* Journal of Neuroscience, 2002. **22**(16): p. 7006-7015.

43. Li, N., et al., *Mitochondrial complex I inhibitor rotenone induces apoptosis through enhancing mitochondrial reactive oxygen species production.* Journal of Biological Chemistry, 2003. **278**(10): p. 8516-8525.
44. Kroemer, G., B. Dallaporta, and M. Resche-Rigon, *The mitochondrial death/life regulator in apoptosis and necrosis.* Annual review of physiology, 1998. **60**(1): p. 619-642.
45. Fink, B.D., et al., *Impaired utilization of membrane potential by complex II-energized mitochondria of obese, diabetic mice assessed using ADP recycling methodology.* American Journal of Physiology-Regulatory, Integrative and Comparative Physiology, 2016. **311**(4): p. R756-R763.
46. Fato, R., et al., *Differential effects of mitochondrial Complex I inhibitors on production of reactive oxygen species.* Biochimica et Biophysica Acta (BBA)-Bioenergetics, 2009. **1787**(5): p. 384-392.
47. Cohen, B.H., P.F. Chinnery, and W.C. Copeland, *POLG-related disorders.* 2014.
48. Naviaux, R.K. and K.V. Nguyen, *POLG mutations associated with Alpers' syndrome and mitochondrial DNA depletion.* Annals of neurology, 2004. **55**(5): p. 706-712.
49. Rahn, J.J., et al., *Zebrafish lacking functional DNA polymerase gamma survive to juvenile stage, despite rapid and sustained mitochondrial DNA depletion, altered energetics and growth.* Nucleic acids research, 2015. **43**(21): p. 10338-10352.
50. Baden, K.N., et al., *Early developmental pathology due to cytochrome c oxidase deficiency is revealed by a new zebrafish model.* Journal of Biological Chemistry, 2007. **282**(48): p. 34839-34849.
51. Scholz, R., Thurman, R. G., Williams.Jr, Chance, B., and Bucher,, *Journal of Biological Chemistry.* Journal of Biological Chemistry 1969: p. 244, 2317.
52. Drezek, R., et al., *Autofluorescence Microscopy of Fresh Cervical-Tissue Sections Reveals Alterations in Tissue Biochemistry with Dysplasia¶.* Photochemistry and photobiology, 2001. **73**(6): p. 636-641.
53. Gulledge, C. and M. Dewhirst, *Tumor oxygenation: a matter of supply and demand.* Anticancer research, 1996. **16**(2): p. 741-749.
54. Ramanujam, N., et al., *Low temperature fluorescence imaging of freeze-trapped human cervical tissues.* Optics Express, 2001. **8**(6): p. 335-343.
55. Skala, M. and N. Ramanujam, *Multiphoton redox ratio imaging for metabolic monitoring in vivo.* Advanced Protocols in Oxidative Stress II, 2010: p. 155-162.
56. Chance, B., *Metabolic heterogeneities in rapidly metabolizing tissues.* Journal of applied cardiology, 1989. **4**(4): p. 207-221.
57. Heikal, A.A., *Intracellular coenzymes as natural biomarkers for metabolic activities and mitochondrial anomalies.* Biomarkers in medicine, 2010. **4**(2): p. 241-263.
58. Boyd, R., *Nonlinear Optics 2nd edn (Amsterdam: Academic).* 2003.
59. Göppert-Mayer, M., *Über elementarakte mit zwei quantensprüngen.* Annalen der Physik, 1931. **401**(3): p. 273-294.
60. Denk, W., J.H. Strickler, and W.W. Webb, *Two-photon laser scanning fluorescence microscopy.* Science, 1990. **248**(4951): p. 73-76.
61. Perry, S.W., R.M. Burke, and E.B. Brown, *Two-photon and second harmonic microscopy in clinical and translational cancer research.* Annals of biomedical engineering, 2012. **40**(2): p. 277-291.
62. Website, *https://www.microscopyu.com/techniques/multi-photon/multiphoton-microscopy*.
63. So, P.T., et al., *Two-photon excitation fluorescence microscopy.* Annual review of biomedical engineering, 2000. **2**(1): p. 399-429.
64. Wang, R.K. and V.V. Tuchin, *Advanced biophotonics: tissue optical sectioning*. 2013: CRC Press.

65. Stender, A.S., et al., *Single cell optical imaging and spectroscopy.* Chemical reviews, 2013. **113**(4): p. 2469.
66. Tuchin, V.V., *Handbook of photonics for biomedical science*. 2010: CRC Press.
67. Denk, W., *Two-photon scanning photochemical microscopy: mapping ligand-gated ion channel distributions.* Proceedings of the National Academy of Sciences, 1994. **91**(14): p. 6629-6633.
68. Lakowicz, J.R. and K.W. Berndt, *Lifetime-selective fluorescence imaging using an rf phase-sensitive camera.* Review of Scientific Instruments, 1991. **62**(7): p. 1727-1734.
69. Gadella, T.W., T.M. Jovin, and R.M. Clegg, *Fluorescence lifetime imaging microscopy (FLIM): spatial resolution of microstructures on the nanosecond time scale.* Biophysical chemistry, 1993. **48**(2): p. 221-239.
70. Sanders, R., et al., *Quantitative pH imaging in cells using confocal fluorescence lifetime imaging microscopy.* Analytical biochemistry, 1995. **227**(2): p. 302-308.
71. French, T., et al., *Two-photon fluorescence lifetime imaging microscopy of macrophage-mediated antigen processing.* Journal of microscopy, 1997. **185**(3): p. 339-353.
72. Website, *https://www.picoquant.com/applications/category/life-science/fluorescence-lifetime-imaging-flim.*
73. Westerfield, M., *The zebrafish book: a guide for the laboratory use of zebrafish (Brachydanio rerio)*. 1995: University of Oregon Press.
74. Seth, A., D.L. Stemple, and I. Barroso, *The emerging use of zebrafish to model metabolic disease.* Disease models & mechanisms, 2013. **6**(5): p. 1080-1088.
75. Libby, P., P.M. Ridker, and A. Maseri, *Inflammation and atherosclerosis.* Circulation, 2002. **105**(9): p. 1135-1143.
76. Lakowicz, J.R., et al., *Fluorescence lifetime imaging of free and protein-bound NADH.* Proceedings of the National Academy of Sciences, 1992. **89**(4): p. 1271-1275.
77. Iweibo, I., *Protein fluorescence and electronic energy transfer in the determination of molecular dimensions and rotational relaxation times of native and coenzyme-bound horse liver alcohol dehydrogenase.* Biochimica et Biophysica Acta (BBA)-Protein Structure, 1976. **446**(1): p. 192-205.
78. webisite, *bio-atlas.psu.edu.*
79. Wallace, K.N., et al., *Intestinal growth and differentiation in zebrafish.* Mechanisms of development, 2005. **122**(2): p. 157-173.
80. Stringari, C., et al., *Multicolor two-photon imaging of endogenous fluorophores in living tissues by wavelength mixing.* Scientific Reports, 2017. **7**.
81. Biemar, F., et al., *Pancreas development in zebrafish: early dispersed appearance of endocrine hormone expressing cells and their convergence to form the definitive islet.* Developmental biology, 2001. **230**(2): p. 189-203.
82. Fine, S. and W. Hansen, *Optical second harmonic generation in biological systems.* Applied optics, 1971. **10**(10): p. 2350-2353.
83. Francesco S. Pavone, P.J.C., *Second Harmonic Generation Imaging.* 2013. **1**: p. 105-106.
84. Ishikawa-Ankerhold, H.C., R. Ankerhold, and G.P. Drummen, *Advanced fluorescence microscopy techniques—Frap, Flip, Flap, Fret and flim.* Molecules, 2012. **17**(4): p. 4047-4132.
85. Giordano, C., et al., *Gastrointestinal dysmotility in mitochondrial neurogastrointestinal encephalomyopathy is caused by mitochondrial DNA depletion.* The American journal of pathology, 2008. **173**(4): p. 1120-1128.
86. Berger, E., et al., *Mitochondrial function controls intestinal epithelial stemness and proliferation.* Nature communications, 2016. **7**: p. 13171.
87. O'Brien, L.C. and A.S. Gorgey, *Skeletal muscle mitochondrial health and spinal cord injury.* World journal of orthopedics, 2016. **7**(10): p. 628.